

ABSTRACT

MAHBOOBA, ZAYNAB MUNTHER. Additive Manufacturing of Bulk Metallic Glass. (Under the Direction of Dr. Ola Harrysson and Dr. Victoria Miller).

A metallic glass is a solid metallic material with a disordered, amorphous, atomic structure. Iron-based metallic glass alloys have roused significant technological interest driven by their desirable combination of mechanical, magnetic and chemical properties which often outperform those of crystalline metals. Despite exhibiting exceptional materials properties, metallic glass alloys have a limited industrial relevance due to the inadequate dimensions and geometries achievable using current manufacturing techniques. An advanced manufacturing technique, additive manufacturing, holds the potential to enable the production of large-scale bulk metallic glass components with complex and intricate geometries, unmatched by the current processing techniques. This work examines the use of laser and electron powder bed fusion additive manufacturing to produce Fe-based bulk metallic glass. One additively manufactured specimen exceeded its critical casting thickness by a factor of 15 or more in all dimensions, and maintained full amorphicity; however, the alloy exhibited a significant propensity to crack during additive manufacturing regardless of process development efforts. Seeking out more crack resistant Fe-based alloys, a novel alloy design methodology and eight unique chemistries with predicted high additive processability and glass forming ability were produced within this work. Although the first round of alloy design did not yield amorphous material, the work highlighted the importance of intrinsic materials properties relating to the additive manufacturability of Fe-based metallic glass and the usefulness of integrated computational materials engineering as a time and cost saving method for novel alloy design for additive manufacturing.

© Copyright 2019 by Zaynab Mahbooba

All Rights Reserved

Additive Manufacturing of Bulk Metallic Glass

by
Zaynab Munther Mahbooba

A dissertation submitted to the Graduate Faculty of
North Carolina State University
in partial fulfillment of the
requirements for the degree of
Doctor of Philosophy

Materials Science and Engineering

Raleigh, North Carolina

2019

APPROVED BY:

Ola Harrysson
Co-chair of Advisory Committee

Victoria Miller
Co-chair of Advisory Committee

Carl Koch

Yuntian Zhu

Harvey West

BIOGRAPHY

Zaynab Mahbooba was born and raised in Raleigh, North Carolina, and she received her B.S. and M.S. from the department of Materials Science and Engineering at North Carolina State University in 2013 and 2015, respectively. During her graduate career, she worked in the Center for Additive Manufacturing and Logistics housed in the Industrial Systems and Engineering department at N.C. State. Outside of the lab, she found joy in the company of her roommates (listed alphabetically: Alex, Emily, John, Kara, and Matt), playing Spikeball, thinking about Harry Potter, working at the high ropes challenge course, taking P.E. classes, and playing racquetball with her dad.

ACKNOWLEDGMENTS

Thank you to Dr. Ola Harrysson for his encouragement, advisement, and patience throughout my graduate career. Thank you to Dr. Harvey West for sharing his infinite knowledge of materials and experimentation. Thank you to Dr. Mattias Unosson, Ms. Lena Thorsson, and the entire team at Sindre Metals and Exmet AB for funding this project, and providing endless support and expertise. Thank you to Dr. Björgvin Hjörvarsson, Jithin Marattukalam, and the entire group in the Ångström Laboratory at Uppsala University for hosting me as a visiting researcher, and Victor Pacheco for producing splat quenched samples. Thank you to Dr. Ida Berglund and Mr. Abhinav Saboo at QuesTek Innovations, and Dr. Martin Walhbrul and Dr. Jiayi Yan at QuesTek Europe AB for hosting me in Evanston, IL, advising me on materials design, and allowing me to use their modeling tools. Thank you to the staff at The Center for Additive Manufacturing and Logistics for providing materials, machinery, and expertise. Finally, thank you to all of my lab mates, Austin, Caroline, Carter, Chris K., Chris L. Harshad, Hengfeng, Katie, Lokesh, Maria, Pedro, Spencer, and Thomas, for their technical support, and for bringing splendid company, conversation, and laughter to the basement of Daniels Hall.

TABLE OF CONTENTS

LIST OF TABLES	vii
LIST OF FIGURES	viii
CHAPTER 1: INTRODUCTION TO METALLIC GLASS AND ADDITIVE MANUFACTURING	1
Introduction to Metallic Glass	1
Glass-forming Compositions	2
Properties	3
Applicability	5
Manufacturing	7
Introduction to Additive Manufacturing	10
Powder Bed Fusion	11
Directed Energy Deposition	11
Sheet Lamination	12
Material Jetting	12
Material Extrusion	13
Chapter 2: Literature review of Additive Manufacturing of Metallic Glass	14
Laser Powder Bed Fusion	14
Electron Beam Melting	22
Directed Energy Deposition	26
Sheet Lamination	30
Material Jetting	34
Material Extrusion	37
Challenges during Additive Manufacturing of Metallic Glass	38
Optimization of Powder Size and Morphology	38
Contamination of Feedstock and during Manufacturing	41
Chemical Segregation in the Melt Pool	43
Devitrification in the Heat Affected Zone	44
Chapter Summary	46
Chapter 3: Additive Manufacturing of an Iron-based Bulk Metallic Glass Larger than the Critical Casting Thickness	48

Chapter 4: Exploring the use of chemistry modifications and electron beam melting to reduce micro-cracking during additive manufacturing of metallic glass.....55

Introduction	55
Materials and Methods	56
Powder characterization	56
Laser Powder Bed Fusion.....	57
Electron Beam Melting.....	58
Results	61
Powder Characterization	61
Laser Powder Bed Fusion.....	65
Electron Beam Melting.....	67
Discussion	69
Powder.....	69
Laser Powder Bed Fusion.....	69
Electron Beam Melting.....	70
Chapter Summary.....	74

Chapter 5: Identification and application of computational tools to propose a novel iron-based metallic glass chemistry with acceptable additive manufacturing processability76

Introduction	76
Analysis of Alloy Design Modeling Tools	81
Liquidus Temperature	81
Glass Transition Temperature	83
Machine Learning Model	86
Phase Prediction	87
Shear Modulus.....	87
Hardness	88
Bulk Modulus	89
Poisson's Ratio	90
Determining Mechanical Requirements.....	91
Alloy Design Steps.....	94
Step 1: Element Selection.....	94
Step 2: Glass Forming Ability Plot Production.....	95
Step 3: Glass Forming Ability Plot Filtering.....	95
Step 4: Shear Modulus Calculation.....	98

Step 5: Phase Analysis.....	99
Step 6: Glass-former Addition.....	101
Step 7: Composition Selection	104
Materials and methods for design analysis	104
Results	106
Discussion	108
Chapter Summary.....	110
Chapter 6: Summary	111
References.....	114

LIST OF TABLES

Table 1. Production methods for metallic glass. Recreated from (Greer, 1995).	8
Table 2. Particle size distribution and morphology of four powder batches processed using LPBF and EBM.	62
Table 3. Parameters that correlate with GFA (Yanglin Li et al., 2017).	79
Table 4. Fe-based glass-forming compositions that were processed using AM and their respective T_g , T_i , cracking and structure (Am=amorphous, Cr=crystalline, Am/Cr=amorphous matrix with grains). Some T_g and T_i values were collected from other references utilizing the same composition. Calculated shear modulus from the QuesTek Europe AB model are reported.	92
Table 5. Fe-based glass-forming compositions that were described as “tough” and their respective T_g , T_i , plastic strain (compression), fracture strength and calculated shear modulus from the QuesTek Europe AB model.	93
Table 6. Effective shear modulus of selected elements from the QuesTek Europe AB shear modulus model.	99
Table 7. Compositions selected by QuesTek Innovations LLC and QuesTek Europe AB for alloy design validation and their calculated G , T_g , T_i and ν values (2019 US Patent Application No. 62/851,261).	104
Table 8. Product description of elemental material purchased from Thermo Fischer Scientific.	106
Table 9. Target and actual chemistry of splat quenched specimens in weight percent.	107

LIST OF FIGURES

Figure 1. Time-temperature-transformation diagram of a bulk metallic glass showing a difference in critical cooling (R_c) and heating (R_h) rate. Recreated from (Lu et al., 2017).	46
Figure 2. Photos depicting LPBF-fabricated AMZ4.....	58
Figure 3. Photo depicting the redesigned EBM build tank for processing small powder batches.	59
Figure 4. Particle size distribution by number (left) and volume (right) of AMZ4 LPBF powder.	63
Figure 5. Particle size distribution by number (left) and volume (right) of FeCrMoCB EBM powder.	63
Figure 6. Particle size distribution by number (left) and volume (right) of FeMoCB LPBF powder.	63
Figure 7. Particle size distribution by number (left) and volume (right) of FeMoCB EBM powder.	63
Figure 8. SEM micrographs of the EBM FeCrMoCB (top-left), LPBF AMZ4 (top-right), LPBF FeMoCB (bottom-left) and EBM FeMoCB (bottom-right) gas atomized powders.	64
Figure 9. LPBF-fabricated FeCrMoCB (left) and FeMoCB (right) cross-sections along the build axis.	66
Figure 10. Cross section along the build plane of LPBF-fabricated AMZ4 revealing spherical porosity between 10 and 30 μm in diameter.	66

Figure 11. Micrographs of LPBF-fabricated AMZ4 along the build axis depicting stress-induced cracks.	66
Figure 12. X-ray diffraction spectrum of LPBF-fabricated AMZ4.	67
Figure 13. Selected EBM builds of FeCrMoCB.	68
Figure 14. X-ray diffraction spectrum of the “best case scenario” EBM-fabricated FeCrMoCB sample.	68
Figure 15. FeCrMoCB EBM samples depicting delamination from the build plate and cracking along the XY plane.	73
Figure 16. Experimental and calculated liquidus temperature (T_l). The liquidus temperature was calculated using Thermo-Calc databases TCFE9 and TCHEA3, and QuesTek’s metallic glass database, QT-BMG.	82
Figure 17. Experimental versus calculated glass transition temperature with (left) and without (right) low-glass-forming compositions.	84
Figure 18. Experimental versus calculated shear modulus (left) and hardness (right) plotted with the + and – error lines.	88
Figure 19. Experimental versus calculated bulk modulus plotted with the + and – error lines (left) and Poisson’s ratio (right).	90
Figure 20. Elements allowed into the machine learning model.	94
Figure 21. Selected ternary diagrams with high GFA (Ren et al., 2018).	97
Figure 22. Shear modulus plots of the high glass-forming Fe-Ni-Zr and Fe-Co-Zr ternary systems.	98
Figure 23. Ternary phase diagrams of Fe-Ni-Ta (top left), Fe-Zr-Co (top right) and Fe-Ni-Zr (bottom middle).	100

Figure 24. Ternary GFA diagrams of Fe-Zr-Co and Fe-Ni-Zr. Compositional space with Fe > 50 at. % and no TCP phases is outlined in red.....	101
Figure 25. Liquidus projection of Fe-Ni-Zr-xP (x = 5, 10 and 15). The area between the green lines is the compositional space where TCP phases were not predicted on the Fe-Ni-Zr phase diagram. The temperature on each plot is the minimum liquidus within this region.	103
Figure 26. Splat quenched specimens.	107
Figure 27. Copper contamination visible on the QTBMG17 specimen.	107
Figure 28. XRD spectra of splat quenched specimens.	108

CHAPTER 1: INTRODUCTION TO METALLIC GLASS AND ADDITIVE MANUFACTURING

This chapter provides a brief introduction to metallic glass compositions, properties, applicability and manufacturing. In addition, this chapter introduces additive manufacturing (AM) and describes five different AM processes.

Introduction to Metallic Glass

Metallic glass first came to prominence in 1959 when Duwez and coworkers demonstrated that amorphous $\text{Au}_{75}\text{Si}_{25}$ (at. %) could be obtained through rapid solidification from the liquid state (Jun et al., 1960). During rapid solidification, atoms do not have sufficient time or energy to arrange for crystal nucleation. Amorphous metallic material was recognized before 1959 (Buckel, 1954). Buckel produced thin films of condensed glassy metallic material in 1954. The significance of Duwez's work was the development of the melt spinning technique that allowed for the production of comparatively large quantities of metallic glass (Jun et al., 1960). Turnbull and coworkers also made a crucial contribution to the discipline; they observed a distinct glass transition temperature (T_g) in rapidly quenched metallic liquid, similar to non-metallic glasses like silicates, polymers and ceramic glass (Chen and Turnbull, 1968). At temperatures below T_g the material is frozen into a solid, and if the material has an amorphous, non-crystalline atomic structure, it can be correctly termed a metallic glass. Metallic glass is less brittle than conventional oxide glass, and has the same opaque, gray and shiny appearance of traditional metals (Telford, 2004).

The technological significance and fundamental interest regarding the formation, structure and properties of metallic glass motivated the surge of academic and industrial research on metallic glass in the late 1970s and 1980s. Some commercial applications have

been established since then and constant discoveries offer novel opportunities for commercial application (Greer, 1995).

Glass-forming Compositions

During cooling of a metal, crystallization becomes thermodynamically possible only when the temperature falls below the liquidus temperature (T_l), and vitrification becomes kinetically possible once the temperature of the uncrystallized melt drops below T_g . Naturally, glass formation is favored if the temperature difference between T_l and T_g is minimized. The reduced glass transition temperature, $T_{rg} = T_g/T_l$, is therefore a useful measure of the glass forming ability (GFA) of metallic alloys (Turnbull, 1969). Since T_g is not strongly compositional dependent, alloy compositions with a high T_{rg} , that favor glass formation, are due to a depression in T_l (typically deep eutectic compositions) (Greer, 1995). Turnbull suggested that compositions with $T_{rg} \geq 2/3$ form stable liquids and have high GFA (Turnbull, 1969); this “rule of thumb” contributed to the development of bulk sized metallic glass (Johnson, 2002).

Alloy compositions with exceptional GFA are castable into dimensions larger than 1 mm; these alloys are termed bulk metallic glasses (BMGs). The first BMG was prepared by Chen in 1974 (Chen, 1974). A PdCuSi alloy was produced into a 1 mm thick section by suction casting. Later, Turnbull prepared a centimeter sized PdNiP alloy using an oxide fluxing method to purify the melt and prevent heterogeneous nucleation during solidification (Drehman et al., 1998; Kui et al., 1998). Bulk sized metallic glass was successfully produced using Pd, however, commercialization of these BMGs was improbable owing to the high cost of Pd. In the 1980s, Inoue designed several low critical cooling rate, multicomponent BMGs using common, lower cost, metallic elements (Inoue, 2000; Inoue et al., 1989). Inoue

summarized the compositional requirements for bulk glass formation and outlined the following rules for alloy design (Inoue, 2000): (1) the alloy system should be multicomponent, comprising of more than three elements. Increasing the number of constituent elements increases the complexity and size of the unit cell, so crystallization is less energetically favorable. (2) The three main constituent elements should have atomic radius mismatches larger than 12%. The atomic size mismatch increases the atomic packing density in the liquid, so a large volumetric change is a requisite for crystallization (Chen and Turnbull, 1969). (3) Lastly, there should be negative heats of mixing between the three main constituent elements; this increases the energy barrier at the solid/liquid interface and reduces the nucleation rate (Trexler and Thadhani, 2010).

Overall, the GFA of a metallic alloy is improved when the liquid is stabilized compared to the competing crystalline phases (Chen and Turnbull, 1969). Alloy compositions satisfying all three of Inoue's rules and those chosen with $T_{rg} \geq 2/3$ should have sluggish crystallization kinetics, and favor glass formation. These rules have successfully guided the development of new BMG compositions, however, in practice it is still challenging and time-consuming to navigate a multicomponent composition space to uncover the best glass-forming compositions (H. Wang et al., 2007).

Properties

The physical and chemical properties of materials are dependent on atomic interactions. For example, the mechanical response of crystalline metals is understood in terms of crystalline defects, and the magnetic properties are explained in terms of the local symmetry of a magnetic species (Hasegawa, 1983). The long- and short-range order that allow for these explanations is missing from the structure of metallic glass. The atomic

arrangement of metallic glass is somewhat understood, but there is no clear translation from the conventional representation of materials properties to the materials properties of metallic glass (Hasegawa, 1983). The disordered structure and metastable state of metallic glass impart unusual structural properties and unconventional deformation mechanisms (Eckert et al., 2007; Schuh et al., 2007).

The mechanical properties of crystalline metals are dictated by dislocation-mediated crystallographic slip (Greer, 1995; Telford, 2004). In metallic glass, the homogeneous structure and the absence of crystalline defects leads to superior strength (closer to the theoretical limit) and high hardness (Inoue, 2000). The tensile fracture strength of metallic glass is double that of crystalline metals; this mechanical improvement is a reflection of the major differences in the deformation and fracture mechanisms between amorphous and crystalline metals (Wang et al., 2004). Crystalline metals exhibit plastic deformation after yielding and therefore demonstrate high fracture toughness and impact resistance. Metallic glass does not exhibit homogeneous plastic deformation; instead, deformation is highly localized into shear bands. Owing to the absence of a work hardening mechanism (i.e. dislocations), plastic flow via shear band propagation leads to work softening. The work softening behavior results in catastrophic, brittle failure during loading (Greer, 1995). The origin of shear bands is not fully understood; however, it is of general consensus that shear banding is a result of local heating or local structural change (Greer, 2009). Lund and Schuh provide a summary of small-scale events that can occur during macroscopic yield and failure of metallic glass (Lund and Schuh, 2004), and Schuh et al. reviewed the deformation of metallic glass in detail (Schuh et al., 2007).

The structural homogeneity and the absence of grain boundaries leads to excellent corrosion, oxidation, and wear resistance in metallic glass (Anantharaman, 1984; Ashby and Greer, 2006; Greer, 1995; Telford, 2004). In addition, metallic glass alloys containing a ferrous transition metal (Fe, Co, or Ni) as the main constituent are highly valued for their soft magnetic properties (Telford, 2004). The homogeneous microstructure, free of crystalline defects, allows for magnetocrystalline isotropy and results in low hysteresis losses and low coercivity (Ashby and Greer, 2006; Liebermann, c1993.; Telford, 2004).

The novel material properties that originate from the amorphous structure of metallic glass are diminished if devitrification takes place. For certain applications and alloys, partial crystallization can improve select properties. For example, a dispersion of crystals in a ferromagnetic glass can pin domain boundaries and reduce hysteretic losses at high frequency (DeCristofaro et al., 1982). Also, partial crystallization of certain phases can improve plasticity (Fan and Inoue, 2000).

Applicability

The unique properties of metallic glass alloys have inspired their use in a variety of applications. Metallic glass has desirable properties for use in structural applications as high-strength aircraft frames, rotating equipment and automobile parts (Johnson, 2002). In addition, metallic glass parts offer improved performance over crystalline metal when applied in prosthetics, surgical implants, pace maker casings and other medical applications due to their exceptional wear and corrosion resistance, and high strength-to weight ratio (Telford, 2004; Wang et al., 2004).

Metallic glass is very hard, so it is attractive for use in the tooling and cutting industry. Due to the lack of grain structure, metallic glass blades can be sharpened to a much

finer edge than a crystalline metal blade (Ashby and Greer, 2006); this means that high quality tooling and cutting devices, such as scalpels, can be produced without the high cost of diamond cutting blades. Furthermore, the high hardness and homogeneous structure of metallic glass allow the opportunity for atomic scale features to be etched into the surface; this is useful for information storage (Ashby and Greer, 2006). Metallic glass can be polished to a stunning reflective finish; this, along with their sheer novelty, makes metallic glass alloys a popular material for luxury items like rings, watch casings, phone casings and glasses frames (Ashby and Greer, 2006).

Metallic glass is an ideal material for springs due to its ability to efficiently store and transfer elastic energy (Ashby and Greer, 2006; Johnson, 2002). The sporting equipment industry has also taken advantage of the high elastic limit of metallic glass. Sporting equipment where energy transfer largely dictates performance, such as baseball bats, tennis racquet frames and golf clubs, have been produced using metallic glass. In one example, a golf club head coated in a metallic glass was twice as hard as and four times more elastic than a titanium driver. The metallic glass coated club can transfer 99% of the initial impact energy to the golf ball compared with only a 70% transfer using a titanium golf club (Telford, 2004).

The low coercivity and high permeability of Fe-based metallic glass is desirable for magnetic applications such as transformer cores, magnetic read heads, magnetic shielding and other magnetic applications (Ashby and Greer, 2006; Greer, 1995). Metallic glass also holds potential for application in microelectromechanical systems. As an example, metallic glass Al_3Ti hinges rotate mirrors in digital light processing technology (i.e. projectors). The metallic glass hinges have been tested to 10^{12} cycles without fatigue failure (Tregilgas,

2004). The challenge with applying metallic glasses is to develop alloys with a desirable set of properties while maintaining suitable processability and manufacturability, and a low cost (Johnson, 2002).

Manufacturing

Vitrification of glass-forming alloys occurs when the liquid cools below the T_g with a sufficiently high rate of solidification, typically on the order of 10^5 – 10^8 K/s (Anantharaman, 1984; Greer, 1995; Telford, 2004). To achieve the required solidification rates, metallic glass manufacturing techniques typically apply a thin layer of liquid to a large, thermally conductive substrate (Chen, 1980). For example, casting into bulk-sized copper molds is a popular BMG manufacturing technique to produce simple geometries such as rods or plates (Greer, 2009; Inoue and Takeuchi, 2011; Telford, 2004). During melt spinning, a widely used metallic glass processing technique, a molten stream of material is cast onto a cooled, rotating drum to achieve solidification rates of 10^5 - 10^6 K/s and produce ribbon-shaped material (Chen, 1980; Greer, 1995). Pulsed laser quenching can achieve even higher cooling rates of 10^{14} K/s (Greer, 1995). This process involves the rapid laser melting of a surface layer (~100nm) atop a large, cooled substrate.

Atomization provides quench rates similar to those found in melt spinning, however, the material is not cooled through contact with a substrate. During atomization, a jet of molten material is ejected from an orifice and through a coolant to produce metallic glass wire, or the liquid is broken into droplets to form a powder (Greer, 1995). Certain alloys might require quench rates unattainable using liquid quenching (Chen, 1980). These compositions are made amorphous using atomic condensation, such as evaporation or sputtering (Chen, 1980; Greer, 1995). For compositions that require clean conditions to

avoid crystallization, techniques such as containerless solidification in freefall or encapsulation of the liquid alloy in another liquid are used to achieve extreme cleanliness (Greer, 1995). Metallic glass is also manufactured using methods other than rapid solidification such as chemical methods, irradiation, mechanical methods and reactions (Greer, 1995); examples of these techniques are listed in Table 1.

Table 1. Production methods for metallic glass. Recreated from (Greer, 1995).

Method	Reference
<i>Rapid liquid cooling</i>	
Melt-spinning, planar flow casting	54, 55
Atomization	56, 57
Wire formation in water	58
As a surface treatment	
Scanned laser or electron beam	59, 60
Pulsed laser beam	6
<i>Undercooling of clean liquids</i>	
Emulsion technique	61
Fluxing	62
Solidification in free fall	63
<i>Physical vapor deposition</i>	
Evaporation	2
Sputtering	64
<i>Chemical methods</i>	
Electroless deposition	65
Electrodeposition	66
Precipitation	67
Hydrogenation	68
<i>Irradiation</i>	
By light or heavy ions	69, 70
By electrons or neutrons	71, 72
Ion implantation or mixing	73, 74
<i>Mechanical methods</i>	
Grinding	75
Mechanical alloying	76
<i>Reactions</i>	
Solid-state reaction of elements	7
Decomposition of crystalline solid solution	30

Current manufacturing methods impose a significant geometric restraint on metallic glass. The production methods listed in Table 1 only provide the opportunity to produce thin films, foils, ribbons, wires, powder, plates, rods or other simple geometries. However, certain strong glass-forming BMGs are producible into more complex shapes using thermoplastic forming (extrusion or blow molding) (Inoue and Takeuchi, 2011; Schroers, 2010). When heated to temperatures between T_g and the crystallization temperature, T_x , metallic glass exhibits a considerable decrease in viscosity, allowing for thermoplastic forming (Schroers, 2010). Since the time window for thermoplastic forming is small and dependent on the thermal stability of the alloy, only strong glass-forming BMGs can feasibly be thermoplastic formed. The best glass-forming alloys often contain toxic (e.g. Be) or expensive elements (Pt, Pd, Au), limiting the viability of large-scale commercialization (Inoue and Takeuchi, 2011).

Furthermore, the solidification rates required to obtain an amorphous microstructure impose a dimensional constraint on BMGs called the critical casting thickness (t_c) (Johnson, 2002; Wang et al., 2004). Typical t_c values are a couple of millimeters, and only the best glass-forming alloys are able to be cast into thicknesses greater than 1 cm (Ashby and Greer, 2006; Inoue, 2000; Wang et al., 2004). Recently, researchers have investigated the use of additive manufacturing to produce metallic glass. The complex geometries allowable by AM are unmatched by current BMG production techniques. In addition, the layerwise manufacturing process enables the production of BMGs thicker than t_c , if the local cooling rate per layer is higher than the critical cooling rate.

Introduction to Additive Manufacturing

Additive manufacturing is defined by ASTM F2792 as the process of joining materials to make objects from 3D model data, layer upon layer, unlike subtractive manufacturing methodologies. The layer-by-layer process removes many geometric limitations present in traditional manufacturing methods. Complex structural designs allowable by AM inspire the production of lightweight, high-strength structures for the aerospace, medical and automotive industries. In practice, AM is performed using the following steps:

1. A 3D computer aided design (CAD) file is generated of the part to be built.
2. The CAD file is converted into a standard tessellation language (.STL) file, which closely approximates the geometry using triangles.
3. The .STL file is sliced into layers to be read by the 3D printer; orientation and scaling are chosen in the AM software.
4. Layers are consolidated using thermal energy, light, or binder.
5. The completed part can be subject to post processing steps.

Additive manufacturing processes are separated into 7 categories: binder jetting, directed energy deposition, material extrusion, material jetting, powder bed fusion, sheet lamination and vat photopolymerization. Recently, researchers have attempted to produce metallic glass using powder bed fusion, directed energy deposition, sheet lamination, material jetting and material extrusion; these AM processes are briefly described in the following subsections.

Powder Bed Fusion

Powder bed fusion (PBF) is an AM technology in which layers of powder are fused together by a laser or electron energy source at locations specified by a computer model. After melting is complete a new powder layer is applied using a roller or blade mechanism, and the process is repeated until part completion (King et al., 2015). Laser powder bed fusion (LPBF) is typically completed at room temperature under an inert atmosphere (Ar or N). The rapid heating and cooling cycles in LPBF result in large residual stresses, so laser-fabrication is typically followed by a stress relief heat treatment. Contrastingly, during electron beam PBF, or electron beam melting (EBM), a controlled vacuum system provides a pressure of 10^{-5} mbar to maintain a clean, oxygen-free atmosphere. Electron beam melting is performed at high temperatures, typically between 700°C and 900°C. The elevated build temperature reduces the thermal gradient between a newly spread layer and previously melted layers, and thereby minimizes residual stress accumulation. Annealing takes place during fabrication, so a post-build heat treatment is not required.

Directed Energy Deposition

Directed energy deposition (DED) is an AM technology in which powder or wire is supplied to the focus of a laser beam and subsequently melted onto a build surface. Unlike PBF, material is only supplied to the portion of the geometry that is being added at that time. After a layer is completed, the deposition nozzle moves up vertically to begin building the next layer. Inert gas is used to locally shield the melt pool, or is pumped into a hermitically sealed build chamber. Directed energy deposition is used to produce metal AM parts; however, it is singular to other AM processes in that it is also used to coat or repair

previously existing parts. In addition, the use of multiple material feed nozzles allows the opportunity to create functionally graded materials using DED.

Sheet Lamination

Sheet lamination is an AM technology in which sheets of material are bound together, usually using an adhesive or ultrasonic welding. After each layer adhesion, excess material is cut or machined away. Unlike in most AM processes, the subtracted, unused material cannot be easily reused. Despite this disadvantage, sheet lamination provides several advantages over powder-based AM processing. Firstly, sheets of material are less sensitive to oxidation than powder due to a dramatic decrease in the surface area to volume ratio. This reduces safety measures required to handle the material, and is particularly useful during the processing of reactive metals. Additionally, the feedstock material does not contain trapped gas defects that cause micro-pores in powder-based AM parts, so achieving full density is easier. Finally, sheets of material have a higher thermal conductivity than powder, so higher heating and cooling rates are achievable.

Material Jetting

Material jetting is an AM technique that is similar to two-dimensional inkjet printing. Complex, three-dimensional parts are produced by depositing droplets of material from a thermal or piezoelectric actuated print head onto a build substrate. Droplets of material can be supplied on demand or continuously during material jetting. After a layer of material is deposited, it cools and hardens or is cured by an ultraviolet light. Commercial material jetting equipment typically supports the production of only polymer and wax materials; however, recently a metal material jetting machine was commercialized.

Material Extrusion

Material extrusion is an AM technology in which a filament is extruded continuously through a heated nozzle and deposited onto a substrate. This AM technique is the most well-known and prominently used AM process since it is utilized in most low-cost, hobbyist printers. Material extrusion is most commonly used to process ABS plastics and other polymers, however can feasibly process any material that is producible into a wire.

Components fabricated using material extrusion typically have poor strength along the build axis and their resolution is limited by the radius of the extrusion nozzle.

CHAPTER 2: LITERATURE REVIEW OF ADDITIVE MANUFACTURING OF METALLIC GLASS

Additive manufacturing processes are separated into 7 categories: binder jetting, directed energy deposition, material extrusion, material jetting, powder bed fusion, sheet lamination and vat photopolymerization. Thus far, researchers have attempted to produce metallic glass using powder bed fusion (laser and electron beam), directed energy deposition, sheet lamination, material jetting and material extrusion. The application of these processes to metallic glass production is described in this chapter.

Laser Powder Bed Fusion

In 2005, Fischer et al. published the first report referring to the use of AM to process metallic glass (Fischer et al., 2005). In their work, a $\text{Pt}_{57.3}\text{Cu}_{14.7}\text{Ni}_{5.3}\text{P}_{22.7}$ (at. %) powder bed was scanned with average laser power ranging from 200 mW to 1 W. Although the cooling rate was sufficient to attain an amorphous microstructure, samples melted with an average laser power of 1 W were heavily crystallized because the powder bed temperature exceeded the T_x . Reducing the average laser power eliminated crystallization; however, powder particles were only superficially connected, so density was poor. Since Fischer's publication, several others have attempted to fabricate metallic glass using LPBF.

The microstructure and density of LPBF-fabricated metallic glass is largely dictated by the laser power, laser scanning speed, spot size, hatch distance (distance between the center of two adjacent scans), scanning strategy, layer thickness, and build plate temperature. Some of these parameters can be combined to calculate the energy density, or energy input, per unit area during laser melting (Equation 1).

Equation 1. Energy input per unit area where P is power, v is scanning speed, t is layer thickness and h is hatch spacing.

$$I = \frac{P}{vht}$$

The heat input per area is a useful variable during parameter optimization, however, its value is not transferable between alloy compositions since *Equation 1* does not account for material properties such as thermal conductivity and reflectivity, or powder size. Pauly et al. observed that a higher energy input improved the density but opposed vitrification of a Zr-based metallic glass, $Zr_{52.5}Cu_{17.9}Ni_{14.6}Al_{10}Ti_5$ (Pauly et al., 2017). Zrodowski et al. revealed similar results; they reported that samples melted with $I = 50 \text{ J/mm}^3$ and with $I = 59 \text{ J/mm}^3$ were denser, but less amorphous than those melted with $I = 25 \text{ J/mm}^3$ (Zrodowski et al., 2016). Several researchers reported higher energy input leading to crystallization (Jung et al., 2015; Li et al., 2014a, 2016; Lu et al., 2019; Pauly et al., 2017; Zrodowski et al., 2016). At lower energy input, incomplete melting of the powder particles results in an increase in porosity (Fischer et al., 2005; Nong et al., 2019; Pauly et al., 2017). Increasing the energy input improves the solid density, but if the energy input is too large the “balling effect” can produce porosity (Pauly et al., 2017). A goal of parameter development is to find an energy input range that can fully melt the powder, but also does not cause crystallization or balling. Even with an optimized energy input, poor density can result from non-ideal hatch spacing or scanning patterns. In addition, porosity is an inherent defect in gas atomized (GA) powder and since the porosity is not annihilated during LPBF, it is inherited in LPBF components. Lu et al. suggest that porosity is even more prominent in LPBF-fabricated metallic glass due to the high liquid viscosity as compared to crystalline metals (Lu et al., 2019).

Jung et al. optimized laser processing parameters for a $\text{Fe}_{68.3}\text{C}_{6.9}\text{Si}_{2.5}\text{B}_{6.7}\text{P}_{8.7}\text{Cr}_{2.3}\text{Mo}_{2.5}\text{Al}_{2.1}$ (at. %) glass-forming alloy; they produced a 6 mm x 2 mm cylinder that was > 99% dense and fully amorphous by x-ray diffraction (XRD) inspection (Jung et al., 2015). While some researchers were able to achieve a near maximum density, others were unable to optimize density during parameter development. Cracking is also a source of poor density in LPBF-fabricated parts (Hofmann et al., 2018; Mahbooba et al., 2018; Pauly et al., 2013). A photograph of a laser-fabricated scaffold by Pauly et al. reveals a high density of cracks in the as-built structure (Pauly et al., 2013). The high heating and cooling rates during laser melting, and the subsequent thermal expansion and contraction cause cracking, especially in materials with limited toughness like metallic glass. Cracking in any material occurs when the applied stress exceeds the fracture strength of that material. According to finite element method (FEM) simulations by Xing et al., the maximum thermal stress generated during LPBF does not exceed the typical fracture strength of strong, Fe-based metallic glass (Xing et al., 2018). Therefore, the thermal stress alone cannot cause cracking during LPBF; instead, defects like pores cause local stress concentrations that induce cracking and deteriorate mechanical properties (Bordeenithikasem et al., 2018b; Lu et al., 2019; Ouyang et al., 2017; Xing et al., 2018). Li et al. produced single line scans of an Al-based glass-forming alloy (Li et al., 2014b). Cracking occurred in the line scans that were melted with a higher laser power because the temperature gradient between the melt and the previously melted layers was larger, so the temperature gradient, and therefore the thermal stress, was more extreme. At lower laser power, the material was very porous as a result of unmelted powder (Li et al., 2014b). Jung et al. reported similar issues when they developed processing parameters for a Fe-based glass-forming alloy. Laser power and scanning speed

were systematically varied while using a layer thickness of 75 μm , a hatch spacing of 110 μm , and a hatch style scanning pattern with a 90-degree rotation. Slow scanning speed and high power input favored the formation of dense, non-porous samples. Samples fabricated with a scanning speed of 1500 mm/s and power greater than 300 W exhibited densities larger than 99%. Despite the high density, cracks were still prominent in the laser-fabricated samples (Jung et al., 2015).

Cracking and porosity impact the material properties of metallic glass. In one example, Lu et al. observed micro-scale porosity positioned at the molten pool boundaries of a 97% dense $\text{Cu}_{50}\text{Zr}_{43}\text{Al}_7$ component; the presence of porosity reduced the compressive strength of the LPBF material (Lu et al., 2019). Ouyang et al. fabricated a 83% amorphous $\text{Zr}_{55}\text{Cu}_{30}\text{Ni}_5\text{Al}_{10}$ (at. %) cylinder with only 0.12% volume fraction of porosity (Ouyang et al., 2017). The calculated stress concentration around the spherical pores (1.4 GPa) was high enough to trigger micro-cracking, but micro-cracks were infrequently observed. The presence of 0.12% porosity did, however, result in lower Young's modulus and plasticity during compression testing as compared to a cast reference sample. In work by Jung et al., the $\text{Fe}_{68.3}\text{C}_{6.9}\text{Si}_{2.5}\text{B}_{6.7}\text{P}_{8.7}\text{Cr}_{2.3}\text{Mo}_{2.5}\text{Al}_{2.1}$ (at. %) virgin powder and AM component exhibited some differences in the initial part of their M-H magnetic hysteresis loop (Jung et al., 2015). Jung et al. suggest that the cracks and pores observed in the AM microstructure, and not in the virgin powder, delayed the materials magnetic response to the applied magnetic field. In addition, the thermal stresses inherent to LPBF could introduce a magnetic anisotropy in the material (Cullity and Graham, c2009.), influencing the material's extrinsic magnetic properties (Jung et al., 2015).

Even with optimized process parameters, complete density is likely unattainable in LPBF even for crystalline metals. In addition, the low build temperature and rapid heating and solidification rates result in thermal stress that can cause cracking or distortion. Typical post processing of LPBF-fabricated crystalline metals therefore typically involves a stress relief and densifying heat treatment. During heat treatment of metallic glass, the heating and cooling rates must be sufficient to avoid crystallization, and the annealing temperature cannot be larger than T_x . Substantial control over time-at-temperature is needed to avoid devitrification during heat treatment of metallic glass. Therefore, post-build heat treatment of bulk-sized components, like those produced via AM, is impracticable since it would be nearly impossible to uniformly relieve stress and avoid devitrification in the thick and poor thermally conductive material. Instead, researchers attempted to alter processing parameters and introduce novel scanning strategies in an attempt to reduce thermal stress in-situ. Prashanth et al. used a heated substrate (400°C) to successfully avoid cracking during LPBF of an 8 mm tall $\text{Al}_{85}\text{Nd}_8\text{Ni}_5\text{Co}_2$ (at. %) cylinder; however, the component was heavily crystallized (Prashanth et al., 2015). Li et al. attempted an in-situ stress relief using a laser re-scanning method on an Al-based BMG composite material (Li et al., 2014a). Their stress relief treatment used two scanning stages. First, a layer was melted with a high energy input to achieve high density. Then, a low energy scan was used to relieve stress. The low energy re-scan rapidly increased the temperature of the material to the supercooled liquid region, where atomic motion is increased and stress is reduced by viscous flow, and then rapidly cooled the material to $T < T_g$. Stress is also reduced due to the lower temperature gradient resulting from the lower heat input. The metallic glass composites that were treated with re-scanning were crack free and showed no new crystalline phase formation. In control samples

that were fabricated without the stress relief re-scan treatment, large cracks extended from the bottom to the center of the sample. Using the stress relief re-scan treatment, a crack-free gear with a 25 mm diameter and a 10 mm thickness was fabricated from the metallic glass composite.

In addition to layer re-scanning, a variety of novel melting and scanning strategies were used to optimize the microstructure of LPBF-fabricated metallic glass. Zrodowski et al. studied the influence of a pulse-random (P-R) remelt strategy on the microstructure of $\text{Fe}_{71}\text{Si}_{10}\text{B}_{11}\text{C}_6\text{Cr}_2$ (at. %) (Zrodowski et al., 2019, 2016). Each layer was first melted with a checkerboard scanning strategy. After initial melting, each layer was re-melted using the P-R scanning strategy which utilized random pulses, at least 1 mm apart, to melt the surface. Samples that were re-melted using the P-R strategy were four times more amorphous than samples melted only using the checkerboard melt strategy (Zrodowski et al., 2016). The P-R re-melted samples also exhibited an increase in relative density and reduction in magnetic coercivity (Zrodowski et al., 2019). The single melt checkerboard strategy in the control samples produced crystalline melt pools 30-60 μm deep and 80-120 μm wide. The P-R melting step produced amorphous melt pools with a much deeper dimension (100-200 μm deep and 30-60 μm wide). The considerable difference in melt pool aspect ratio between the two melt strategies is a result of the transition from conduction melting to keyhole melting. A difference in crystallinity is due to the variation in laser exposure time. The checkerboard melting had a longer exposure time (500 μs or 1000 μs) than the P-R melt strategy (20 μs). Both pulse durations may have provided cooling rates sufficient for vitrification; however, a thermal model demonstrated that only a short pulse duration during P-R remelting achieved a heating rate larger than the critical heating rate to avoid

devitrification. Overall, the P-R strategy restored the amorphous structure after initial melting and reduced stress accumulation to allow for the LPBF of crack-free material.

In addition to optimizing density and reducing thermal stress, crystallization of the glass-forming alloys was a major challenge during LPBF. Ouyang et al. suggested that crystallization during LPBF occurred during reheating, since their FEM modeling indicated that the cooling rate in the melt pool, heat affected zone (HAZ), and beyond the HAZ were all sufficient for amorphization (Ouyang et al., 2017). Similarly, Lu et al. suggest that thermal annealing during LPBF allows for atomic rearrangement (Lu et al., 2019). Yang et al. used pulsed laser surface melting and LPBF to examine the crystallization behavior of $Zr_{55}Al_{10}Ni_5Cu_{30}$ (at. %) (Yang et al., 2012). Laser surface melting was performed on $Zr_{55}Al_{10}Ni_5Cu_{30}$ amorphous substrates. The surface was melted using 1, 6, 12 and 20 laser pulses at a single point. Cross sectional analysis of the melt pools melted with 1 and 6 pulses were featureless; this is indicative of a fully-amorphous structure. As the pulse number increased to 12 and 20 times, the HAZ, the area surrounding the melt zone, contained spherulite clusters. Similar results were collected during LPBF of $Zr_{55}Al_{10}Ni_5Cu_{30}$. One, 2, 4, and 7 layer deposits were produced, and the deposits with 1 and 2 layers show no difference in microstructure, both are fully amorphous. As the deposit thickness increased to 4 and 7 layers, dendritic features were observed in the HAZ. These results imply that the accumulation of heat and structural relaxation during the melting of subsequent layers influences the final microstructure.

Likewise, the build substrate temperature influences the microstructure of LPBF metallic glass. Li et al. investigated the effect of substrate temperature on the interface bond between the substrate and a laser melted $Al_{86}Ni_6Co_{4.5}La_{1.5}$ (at. %) glass-forming alloy (X. P.

Li et al., 2015). A 100 μm layer was melted onto two aluminum substrates (120 W, 750 mm/s): one at room temperature (25°C) and one heated to 250°C. A thermal model characterizing the heat distribution within the melt pool and build substrate was created to supplement experimental data. At room temperature, a distinct interfacial gap was observable between the metallic glass and the build substrate. Although the powder was fully melted, the surface layer of the aluminum substrate did not melt. When the build plate was heated to 250°C, the powder and build substrate were melted together and strongly bonded. In addition, at 250°C a sub-circular region 50 μm deep exists between the metallic glass and the build substrate. Similarly, the thermal model illustrates that at 250°C a larger volume of material is heated to temperatures greater than the melting temperature of aluminum. The model was also used to predict the cooling rate at the center of the melt pool for the room temperature and 250°C build substrate temperatures at 3.6×10^3 K/s and 3.5×10^3 K/s, respectively. Cooling rate at both substrate temperatures is larger than the critical cooling rate for the $\text{Al}_{86}\text{Ni}_6\text{Co}_{4.5}\text{La}_{1.5}$ (at. %) alloy; however, the model is based off the assumption that heat can be readily transferred into the substrate. Experimental results showed that at room temperature, the small melt volume caused a gap to form between the substrate and material that hindered heat transfer to the substrate. This caused a reduced cooling rate and subsequent crystallization. The strong bond between the metallic glass and the aluminum substrate at 250°C enhanced heat transfer through the build substrate, and allowed for full vitrification of the Al-based metallic glass. Work by Li et al. demonstrates the critical role build substrate temperature plays in the final microstructure of LPBF processed metallic glass (X. P. Li et al., 2015).

Optimizing process parameters to achieve full density and amorphicity was the focus of LPBF research. Due to the complex thermal history during LPBF and the metastable nature of metallic glass, devitrification of material during LPBF was commonly reported, even when sufficient cooling rates were predicted. In addition, stress induced cracking was a common struggle during parameter development, especially in brittle Fe-based metallic glass (Hofmann et al., 2018; Mahbooba et al., 2018; Nong et al., 2019; Żrodowski et al., 2019). Despite these challenges, researchers utilized LPBF to attain BMG dimensions significantly larger than the critical casting thickness (Lin et al., 2019; Mahbooba et al., 2018), and to fabricate complex geometries such as scaffolds (Pauly et al., 2017, 2013; Yang et al., 2018), gears (Li et al., 2016; Nong et al., 2019), and an acetabular cup (Zhang et al., 2019), that are not achievable using traditional manufacturing.

Electron Beam Melting

Electron beam melting is commonly associated with the production of electrically conductive materials and high processing temperatures, both unattractive for metallic glass production. Regardless, EBM is a feasible processing technique for metallic glass. Electron beam melting offers a considerably higher level of control over processing parameters than any other AM technique; this includes a complex thermal model that adjusts heat input over time. The high level of control is facilitated through a large number of variable parameters, many of which are not independent. Subsequently, material development is significantly more laborious for EBM than for a laser-based system. For this reason, researchers have mostly shied away from using EBM to process metallic glasses, and only two articles were published on the topic. In addition to the complex processing parameters, production in a stock EBM machine requires more than 10 liters of powder, even for the fabrication of small

components. This is a result of the powder feeder design in commercially available EBM equipment. Due to the high cost of EBM quality powder, producing large powder batches for new alloy development is impractical. To circumvent this challenge, Koptuyug et al. used specially designed small powder containers and a smaller build tank that required much less powder in order to process a metallic glass using EBM (Koptuyug et al., 2013).

During electron beam/powder bed interaction, powder particles become electrostatically charged and repel one another if the charge is not dissipated quickly. If the repulsive forces overcome the force of gravity then the powder particles electrostatically repel and form a cloud of metal powder, a process known as “smoking”. Smoking typically results in a build failure. Poor electrical conductivity and non-ideal powder size, morphology, and chemistry are chief contributors to smoking. Electron beam melting of low conductivity materials, like metallic glass, is achieved by preheating the powder bed with the electron beam before melting each layer. This preheating step anchors the powder particles together; its main purpose is to provide better thermal and electrical conductivity during melting. Retaining the spherical powder morphology after preheat sintering is imperative since the successful recovery of non-melted powder makes the EBM process cost-effective (Drescher and Seitz, 2015; Koptuyug et al., 2013). In 2015, Drescher and Seitz optimized the EBM preheat parameters for a glass-forming alloy with nominal composition $Zr_{70}Cu_{24}Al_4Nb_2$ (at. %) (Drescher and Seitz, 2015). During preheat parameter development, focus offset and layer thickness were held constant at 80 mA and 125 μm , while beam scanning speed and current were varied. A parameter set using a beam speed of 8 m/s and a beam current of 22 mA did not densify the powder bed at all. In opposition, beam parameters of 12 m/s and 32 mA over-sintered the powder particles, and eliminated the original particle morphology.

After further parameter development, a 5 mm tall sintered cake was produced that contained sufficient density for EBM processing. Drescher and Seitz, and Koptuyug et al. report that minute changes from the ideal processing parameters resulted in over or under-sintered powder (Drescher and Seitz, 2015; Koptuyug et al., 2013). Koptuyug et al. developed a preheat processing space for an Fe-based glass-forming alloy on a stainless-steel build substrate through systematic variation of beam current, beam speed and focus offset (Koptuyug et al., 2013). During preheating, trapped gas (Drescher and Seitz, 2015; Koptuyug et al., 2013) and water vapor (Koptuyug et al., 2013) were released from the powder particles. In the work by Koptuyug et al., powder near the working area was stained brown suggesting that hydroxides were present on the powder surface (Koptuyug et al., 2013). Similarly, Drescher and Seitz noted that the EBM process became more volatile (likely to smoke) with increased powder reuse, even when using identical processing parameters (Drescher and Seitz, 2015). This is possibly a result of powder oxidation, but oxygen analysis was not reported.

Electron beam melting is a heated process, so during the processing of conventional metals the build substrate is preheated $\gg 100^\circ\text{C}$. Drescher and Seitz did not use a heated build substrate during preheat parameter development of $\text{Zr}_{70}\text{Cu}_{24}\text{Al}_4\text{Nb}_2$ (Drescher and Seitz, 2015). Build plate heating facilitates in-situ stress relief, and its absence during the melting stage will likely result in stress induced delamination or distortion. Build plate temperature was not mentioned by Koptuyug et al..

In addition to the preheat parameters, Koptuyug et al. also developed melting parameters for their Fe-based glass-forming alloy. During melting, the build temperature was kept within the narrow window between the “firework” zone (ejected white-hot powder resulting from a low preheat temperature) and the T_g , “firework” zone ($350\text{-}400^\circ\text{C}$) $<$ build

temperature (420-470°C) < T_g (500-600°C). Since the build temperature stabilizes near the preheat sinter temperature during EBM, metallic glass compositions with a low T_g , and a smaller temperature gap between T_g and T_l would be problematic, or impossible, to process using EBM due to the requirement to sinter and melt material while maintaining a build temperature < T_g . Optimized melt parameters were used to produce 50 mm x 50 mm x 5 mm samples. Analyses indicate that the EBM-fabricated material is partially amorphous, and has promising mechanical and chemical properties (Koptug et al., 2013).

Parameter development in EBM is demanding for any material. Parameter development is particularly challenging for metallic glass alloys because they are less electrically and thermally conductive than crystalline metals, so dissipation of charge and heat is poor. Metallic glass also requires high cooling rates and low processing temperatures (< T_g) to attain and maintain an amorphous microstructure. Finding and maintaining a build temperature between the firework zone and the T_g is the predominate challenge during EBM processing of metallic glass. Depending on the physical properties, some metallic glass compositions are presumably not suitable for processing using EBM. Although EBM processing has not yet yielded significant results, its utility as a metallic glass processing technique is still viable. The elevated build temperature has the potential to reduce or erase thermal stress cracking, which is a primary challenge during LPBF of metallic glass. In addition, reactive metals, like Ti- or Zr-based metallic glasses, are less likely to oxidize during EBM since processing is completed under vacuum (10^{-5} mbar); this is particularly useful since GFA degrades with minute levels of oxygen contamination.

Directed Energy Deposition

Several researchers investigated the use of DED as a means to fabricate metallic glass components. When used to fabricate metallic glass out of pre-alloyed powder, the processing challenges associated with DED are applicable to any laser-based AM system. For example, Zheng et al. observed an increase in the size and fraction of a crystalline phase with increasing build thickness during laser engineered net shaping (LENS) of a Fe-based metallic glass (Zheng et al., 2009a). Numerical simulations confirmed that the accumulation of thermal energy and decrease in solidification rate with deposit thickness promoted devitrification during layerwise deposition of metallic glass (Zheng et al., 2008, 2009a). Ye and Shin produced a crack-free FeCrMoWMnCSiB deposit using LENS (Ye and Shin, 2014). They achieved a crack-free structure, despite the material's crack tendency, by pre-heating the build substrate to 422°C to reduce the thermal gradient between the current and previously deposited layers during processing. Despite the small thickness of the deposit (6 layers), crystals were observed in the HAZ of each layer. Devitrification in the HAZ was a commonly reported challenge during LENS of metallic glass (Lu et al., 2018; Sun and Flores, 2008, 2010, 2013; Xu et al., 2019; Ye and Shin, 2014; Zheng et al., 2009a). Sun and Flores observed equiaxed, spherical crystals often surrounded by amorphous material in the HAZ of their LENS-fabricated Zr- and Cu-based metallic glass (Sun and Flores, 2013, 2010, 2008). The discontinuity, size and composition of the spherulites indicate that the crystals formed from the solid state during reheating, and that the rapid heating suppressed phase separation (Sun and Flores, 2013). Despite its prominence in DED and LPBF-fabricated metallic glass, crystallization in the HAZ is not inevitable. The thickness of the HAZ increases with increasing heat input, therefore crystallization in the HAZ is preventable if the

heat input is below some threshold value (Sun and Flores, 2008; Zheng et al., 2009a). In one example, Sun and Flores almost eliminated crystallization in the HAZ of LENS-fabricated $Zr_{58.5}Cu_{15.6}Ni_{12.8}Al_{10.3}Nb_{2.8}$ (at. %) simply by increasing the laser scanning speed from 14.8 mm/s to 21.2 mm/s (Sun and Flores, 2010). They observed microhardness and T_g values that were slightly different from the as-cast material, possibly an indication of a higher free volume in the LENS components due to the higher solidification rates.

Unlike LPBF and EBM, DED is not limited to powder as the feedstock material. Kim et al. used a glass-forming $Cu_{66.5}Zr_{33.5}$ (at. %) wire with a diameter of 155 μm as feedstock for DED (Kim et al., 2017). Wire feedstock offers several advantages over powder for AM. Most notably, wire has a lower material cost and reactivity over AM powder. Also, wire does not contain the micro-porosity often found in GA powder. Single tracks of the CuZr wire were deposited onto a stainless steel build substrate and showed an amorphous structure and no observable HAZ when deposited with the appropriate deposition and laser parameters.

In addition to offering flexibility in terms of feedstock type, DED allows for the production of functionally graded materials. This is achievable by varying the delivery rate of elemental powders to the melt pool. As a result, the use of DED to rapidly screen potential alloy systems holds immense value for the development of new metallic glass alloys (Welk et al., 2014). Tsai and Flores developed a high-throughput strategy for discovering and characterizing new metallic glass compositions (Tsai and Flores, 2016, 2015, 2014). They produced compositionally graded Cu_xZr_{100-x} specimens (x ranging 61-76 at. %) using DED. During manufacturing, the Cu delivery rate was increased while the Zr delivery rate was decreased across the X- and Y-axes. Glass-forming regions were rapidly identified

by observing the topographical features of the fabricated layer and confirmed using electron microscopy. Featureless, amorphous surface regions were observed over the range $x = 62-67$ at. % Cu. Nine lines were re-melted into the initial deposit using 200 W at 12.7 mm/s and then with 100-180 W at 16.9 mm/s scanning speed. The re-melting step facilitated adequate melting and mixing of the deposited powder in the localized lines. Using this rapid screening methodology, it was determined that the most stable composition within the explored range was $\text{Cu}_{64.7}\text{Zr}_{35.3}$ (at. %). This is in agreement with a previously reported optimal CuZr composition of $\text{Cu}_{64.5}\text{Zr}_{35.5}$ (at. %) that was identified by trial-and-error testing (Tsai and Flores, 2014).

Tsai and Flores extended their methodology to a CuZrTi ternary system (Tsai and Flores, 2016). Differently from their CuZr study, each elemental powder was deposited as its own layer using a constant laser power and powder delivery rate. The travel speed of the build substrate relative to the laser and powder source was continuously varied to produce a compositional gradient. The Zr powder was deposited first. The Cu powder was deposited second, and after its deposition a series of lines was re-melted to facilitate complete mixing of the Cu and Zr layers. The Ti was deposited in the third layer, and the series of lines was re-melted again to incorporate Ti. The series of lines was placed such that the CuZr molar ratio remained fixed within a single re-melted line while the Ti content increased along the length of the line, producing a collection of tie lines in the ternary composition map. The remelting was completed at three different laser powers, 200, 240 and 280 W to produce three different compositional libraries that can show the effect of process conditions on glass formation. Using DED, each library of composition/laser power took less than 20 min to complete. This continuous deposition scheme resulted in a ternary map that highlights the

best CuZrTi glass-forming compositions within those tested. The glass-forming compositional range diminished as laser power (i.e. heat input) increased; this was attributed to the reduction in cooling rate with increasing laser power. Tsai and Flores used a pyrometer to measure the surface temperature profiles during melting and measured a decrease in the cooling rate by almost 30% with an increase in laser power from 200 W to 280 W. As the cooling rates decreased less compositions could vitrify resulting in a gradual convergence of the amorphous compositional space towards the one with the highest GFA. Based on these observations, $\text{Cu}_{51.7}\text{Zr}_{36.7}\text{Ti}_{11.6}$ (at. %) was predicted to be the optimal glass former within the compositional space (Tsai and Flores, 2016). The t_c of $\text{Cu}_{51.7}\text{Zr}_{36.7}\text{Ti}_{11.6}$ (at. %) was compared to that of $\text{Cu}_{60}\text{Zr}_{30}\text{Ti}_{10}$ (at. %) (Inoue et al., 2001) and $(\text{Cu}_{0.64}\text{Zr}_{0.36})_{90}\text{Ti}_{10}$ (at. %) (Q. Wang et al., 2007), both recognized as notable and the best glass formers in the CuZrTi system. Suction cast wedge samples were used to determine t_c values of 1.50, 1.35, and 1.20 mm (± 0.05 mm), respectively for $\text{Cu}_{51.7}\text{Zr}_{36.7}\text{Ti}_{11.6}$, $(\text{Cu}_{0.64}\text{Zr}_{0.36})_{90}\text{Ti}_{10}$, and $\text{Cu}_{60}\text{Zr}_{30}\text{Ti}_{10}$. These differences in t_c are consistent with the expected placement of the alloy compositions on the DED ternary library chart. Due to the inefficiency of the currently used trial-and-error metallic glass alloy development methods, DED holds extreme value for the development of new glass-forming compositions. Tsai and Flores demonstrated a straightforward and efficient methodology for rapidly screening a wide compositional space for alloys with high GFA. Similar challenges with optimizing density and microstructure were noted during DED of metallic glass. Researchers prominently report issues with devitrification in the HAZ; this will be discussed in greater detail in the *Devitrification in the Heat Affected Zone* section.

Sheet Lamination

Chen et al. developed a laser foil printer (LFP) utilizing sheet lamination technology (Chen et al., 2017) that has been used to fabricate bulk-scale $Zr_{52.5}Ti_5Al_{10}Ni_{14.6}Cu_{17.9}$ (at. %) (hereafter referred to as LM105) (Bordeenithikasem et al., 2018a; Y. Li et al., 2018b, 2018a; Shen et al., 2017a). During LFP, a foil is loaded on top of a substrate or the previous layer. The foil is line or spot welded to the material beneath it using argon as a shielding gas, and the excess material is removed using a UV laser cutting. To facilitate rapid solidification, active cooling of the build substrate is accomplished through the use of a heat exchanger plate and liquid nitrogen or argon flow (Shen et al., 2017a).

Similarly to LPBF and DED, the laser parameters in LFP dictate the final microstructure and the bonding strength of the substrate-layer and layer-layer joints, and non-optimized laser parameters can result in devitrification, poor density, layer delamination, geometric distortion and other defects. Shen et al. analyzed the effect of LFP laser parameters on the weld quality between an amorphous LM105 foil and an amorphous LM105 substrate. Three parameter sets were used, A (400 W, 100 mm/s), B (200 W, 150 mm/s) and C (200 W, 4 ms) (Shen et al., 2017a). Parameter set A produced a strong weld between the metallic glass foil and substrate. In addition, a fully-amorphous microstructure was maintained at the joint. In parameter set B, the laser scanning speed was reduced from 150 mm/s to 100 mm/s; this caused crystallization in the HAZ. Devitrification was seemingly a result of the increase in energy input from 1.33 J/mm in parameter set A, to 4 J/mm in parameter set B. Excessive energy deposition can cause crystallization and can also distort the foil and cause material evaporation and ejection. In parameter sets A and B, the laser was operated in continuous wave mode and a line welding strategy was used. In

parameter set C the laser was operated in pulsed mode, and the foil was spot welded to the build substrate. A 10 mm³ cube was fabricated using the spot weld strategy and parameter set C. The LFP cube is XRD amorphous and has an Archimedes' density comparable to that of the original foil. Results from differential scanning calorimetry show a slight variation in curve shape compared to the metallic glass foil, which was attributed to a variation in free volume, composition (by element evaporation) or the formation of nano-sized crystals during processing. More complex geometries including fusilli pasta and slipped cylinder shaped parts were fabricated using parameter set C.

To complement experimental work, Shen et al. presented a thermal model that predicted the heating and cooling rates of LM105 using parameter sets A-C. Due to the rapid solidification rates in laser melting conduction mode welding was assumed, so fluid flow and its effect on heat transfer were not taken into account. The model indicates that the heating and cooling rates using all three parameter sets were sufficient to avoid crystallization in LM105. However, during LFP crystallization occurred in the weld prepared using parameter set B (Shen et al., 2017a). Similar cases of devitrification during laser welding despite sufficiently high heating and cooling rates were reported in other referenced articles (Kim et al., 2007; Li et al., 2006; Wang et al., 2010). The GFA of metallic glass is highly sensitive to compositional changes. Evaporation of elements with lower vaporization temperatures during laser welding could alter the GFA and cause crystallization (Shen et al., 2017a). In addition, the time-temperature-transformation (TTT) curves can deform or shift at different temperature gradients, so microstructural evolution during laser welding is less predictable (Sun, 2010).

Shen et al. demonstrated the feasibility of LFP LM105 onto amorphous LM105 substrates. It is both challenging and costly to produce thick amorphous plates to be used as build substrates for AM. For this reason, Li et al. examined the weldability of LM105 foil to Ti6Al4V, Zr702 (Yingqi Li et al., 2017b) and 304 stainless steel (Y. Li et al., 2018a) substrates. A high-quality weld between the first deposited layer and the build substrate is critical for successful AM because this joint anchors the part to the plate providing a path for heat flux and prevents stress related delamination (Yingqi Li et al., 2017b). Ten layers of foil were deposited on to a Ti6Al4V substrate (Yingqi Li et al., 2017b). Elemental analysis of the weld indicated that mixing of the Ti6Al4V build substrate and metallic glass foil was substantial. After the 10 layers of deposition, the foil delaminated from the build substrate due to the formation of several hard, brittle intermetallic phases at the joint. The high Ti content at the glass-Ti6Al4V interface (~50 at. %) decreased the GFA and promoted the formation of these intermetallic phases (Yingqi Li et al., 2017b). A variation in the coefficient of thermal expansion (CTE) between dissimilar metals can also cause cracking at a weld joint. However, the CTE of LM105 is closer to Ti6Al4V than Zr702, and after 10 layers of deposition no cracking or delamination occurred at the glass-Zr702 weld. Cracking was suppressed at the glass-Zr702 joint due to the formation of a higher volume percent of ductile α -Zr. The sample was fully amorphous from the second layer up. Bordeenithikasem et al. also fabricated amorphous LM105 onto crystalline Zr substrates. The LFP-fabricated parts exhibited high strength and plastic strain in bending, exceeding that of cast LM105 beams. In addition, the 4 mm thick LFP exhibited XRD amorphicity while cast samples were only amorphous up to 2.5 mm (Bordeenithikasem et al., 2018a). Regardless of the build substrate material, dilution of the substrate with the foil occurred. The compositional

shift caused crystallization at both the glass-Ti6Al4V and glass-Zr702 joint, but differences in the phase properties dictated crack susceptibility of the joint and overall success of LFP (Yingqi Li et al., 2017a).

Li et al. demonstrated the feasibility of depositing LM105 onto Zr702, but they had challenges welding LM105 to Ti6Al4V (Yingqi Li et al., 2017a). Ti6Al4V is lower cost and easier to obtain than Zr702, so it is advantageous to improve the quality of the glass-Ti bond to allow for low cost LFP. To improve the glass-Ti bond strength Li et al. used intermediate layers of Zr702 foil to prevent interaction between LM105 and the Ti6Al4V substrate. Tensile samples were LFP to examine the bonding strength of glass-Ti joints with one and two intermediate layers of Zr702. A control sample with no intermediate layer fractured at the Ti-glass joint after ten layers of deposition. The tensile bar fabricated with one intermediate layer did not fail during LFP due to a decrease in Ti and increase in Zr content at the interface. Instead, the sample fractured during electric discharge machining (EDM) at the glass-Zr joint. The formation of Ti intermetallics, and the accumulation of stress between Zr and the metallic glass reduced the bond strength. The tensile bar fabricated using two intermediate Zr702 layers did not fracture during LFP or EDM. The formation of α -Zr at the glass-Zr interface and the decrease in Ti resulted in an improved bonding strength between the layers. The sample failed at the Ti-Zr interface during tensile loading with an average bonding strength of 758 MPa (Yingqi Li et al., 2017b), outperforming samples built onto a 304 stainless steel substrate with V, Ti and Zr intermediate layers (477 MPa) (Y. Li et al., 2018a). Similar to the parts fabricated onto amorphous substrates, the LFP tensile bars printed with two intermediate layers contained no pores, cracks or crystals (Yingqi Li et al., 2017b). In a separate work, the properties of the bulk LM105 material, built on a Ti6Al4V

substrate with two intermediate Zr702 layers, were analyzed. The LFP components exhibited physical (T_g , T_x and T_i) and mechanical (micro-hardness, tensile strength and flexural strength) properties comparable to that of LM105 fabricated via injection molding (Y. Li et al., 2018b).

Thus far, only one alloy has been processed using LFP, $Zr_{52.5}Ti_5Al_{10}Ni_{14.6}Cu_{17.9}$ (at. %). Laser foil printed LM105 parts exhibit high density and XRD amorphicity when produced into large-scale, complex geometries. A strong lamination between the first deposited layer and the build substrate is imperative for successful AM processing. Accordingly, it has been a focus of research regarding metallic glass production using LFP (Yingqi Li et al., 2017a, 2017b). Research by Shen et al. emphasizes the effect of thermal history, not just heating and cooling rates, on crystal evolution in laser processed metallic glass (Shen et al., 2017a, 2017b). A primary challenge of LFP is maintaining an energy input low enough to eliminate HAZ crystallization and keyhole porosity, but high enough to produce a strong bonding between layers. Few publications have been published on the topic of sheet lamination of metallic glass; however, the technology shows the potential to produce dense, crack-free bulk metallic glasses with complex geometries.

Material Jetting

The material jetting process is typically associated with the production of thermoset photopolymers. However, the basic principles of the material jetting technology can be used to produce many other materials and has inspired the design of two homemade material jetting, AM machines that can fabricate metallic glass (Wu et al., 2018; C. Zhang et al., 2018). Wu et al. employed a pneumatic injection AM process to deposit metallic glass at room temperature to avoid crystallization during processing (Wu et al., 2018). Pneumatic-

injection printing of a powder slurry was first developed by Cesarano et al. (Cesarano et al., 1998). In this method, a powder slurry is deposited according to a CAD model. This technology has been used to print powders that are challenging to melt using conventional AM equipment such as a piezoelectric, ceramic material (Y. Li et al., 2015). The study by Wu et al. focused on selecting particle size and dispersant type to prepare a FeMoCr metallic glass slurry suitable for pneumatic-injection (Wu et al., 2018). The slurry comprised of XRD-amorphous FeMoCr powder mixed with a solvent, a dispersant, a binder and a defoamer. The wettability of different particle size distributions (5-75 μm , 20-100 μm , and 45-200 μm) and morphologies (spherical and irregular) were analyzed in eight different dispersants. The most stable suspension (5-75 μm , spherical, ammonium polyacrylate) was used to produce a slurry for inkjet deposition with 50% solid content. During pneumatic injection, the line width ranged from 1000-2200 μm and was influenced by nozzle speed, injection pressure, and layer thickness. A single layer of the FeMoCr slurry was deposited using pneumatic injection. The physical properties of the deposited material were not reported but was stated as the focus for future experimentation.

Zhang et al. developed a novel thermal spray method to produce large-scale metallic glass geometries (C. Zhang et al., 2018). They took a traditional coating method, thermal spraying, and applied it iteratively to create a bulk three-dimensional part. Cooling rates on the order of 10^6 K/s were achieved during the high velocity (600–1000 m s^{-1}) deposition of 40 μm layers of semi-molten, amorphous $\text{Fe}_{48}\text{C}_{15}\text{B}_6\text{Mo}_{14}\text{Cr}_{15}\text{Y}_2$ (at %) powder. A crack-free, 20 mm x 20 mm x 20 mm specimen was fabricated using the thermal spray technique. These dimensions are larger than the critical casting thickness of the alloy, and the thermal spray metallic glass was 95% amorphous (C. Zhang et al., 2018). Mechanical properties of

the thermal spray-fabricated metallic glass were compared to as-cast rods of the same alloy composition. The thermal spray metallic glass exhibited a fracture strength of 2.06 GPa (C. Zhang et al., 2018). Although this is lower than that of the cast sample (3.25GPa), it is higher than most high-strength steels (Jiao et al., 2016). Similarly, the Young's modulus of the thermal spray metallic glass (123 GPa) was lower than the as-cast metallic glass (235 GPa) (C. Zhang et al., 2018). The reduction in mechanical properties resulted from the imperfect bonding between the thermal sprayed layers, and the porosity (0.35%). The as-cast metallic glass showed no indication of crack deflection. During fracture toughness measurement the sample failed in a brittle, catastrophic manner. In contrast, during fracture toughness measurement of the thermal sprayed metallic glass, the fracture site showed substantial crack deflection during crack propagation. Although the thermal spray metallic glass still exhibited brittle characteristics, it did not fail catastrophically like the as-cast metallic glass. The improved fracture toughness and crack deflection was attributed to the heterogeneous, layered structure created during the layer-by-layer fabrication. Although the bulk material is brittle, the interfacial regions between the layers act similarly to a secondary phase, and have a different mechanical response during crack tip interaction.

Few articles regarding material jetting of metallic glass have been identified; however, the novel processing methods proposed by Wu et al. and Zhang et al. demonstrate its feasibility as a metallic glass production technique. The thermal spraying technique offers a significant advantage over laser melting AM through the reduction of thermal stress during fabrication. Thermal stress is reduced since only the surface of the powder is melted, and the melt/solidification area is reduced. The thermal sprayed Fe-based metallic glass was free of cracking. This is a great advantage since cracking is reported as a major challenge during

laser processing of metallic glass, especially for Fe-based alloys. The pneumatic-injection technique also demonstrates a major advantage over other AM techniques. Since the process is not heated, the possibility of devitrification during fabrication is eliminated.

Material Extrusion

Conventional metals cannot be maintained at viscosities on practical time scales and are therefore, ill-suited for material extrusion processing. Dissimilarly, metallic glass contains a supercooled liquid region between the T_g and T_x , allowing them to be thermoplastically formed using processing methods commonly associated with thermoplastic polymers, like material extrusion. Gibson et al. take advantage of the thermoplastic formability of metallic glass by utilizing a material extrusion process, called fused filament fabrication (FFF), to fabricate fully-amorphous, $Zr_{44}Ti_{11}Cu_{10}Ni_{10}Be_{25}$ components (Gibson et al., 2018). One millimeter thick $Zr_{44}Ti_{11}Cu_{10}Ni_{10}Be_{25}$ rods were fed into an extrusion head at $460^\circ C$ ($T_g < 460^\circ C < T_x$), at which the time to crystallization is ~ 100 s. Extrusion was performed in air, so metallurgical bonding between the layers was achieved only by introducing a strain at the interface between the current and previous layer (Chen et al., 2014). The role of the interfacial strain is to break the native oxide film to allow for metallurgical bonding. An interfacial strain was established by controlling the bead aspect ratio such that the extrudate must deform laterally, in the XY-plane, during deposition. The interfacial strain and subsequent bonding is achieved only if both layers deform together. For this reason, the temperature of the current and previous layer must be similar; this was achieved via local heating of the previous layer ahead of the extrusion nozzle.

Despite being fabricated in air, the as-fabricated material was XRD amorphous. This is notable considering the high reactivity of several constituents in $Zr_{44}Ti_{11}Cu_{10}Ni_{10}Be_{25}$ with

oxygen. The authors suggest that printing the material in its amorphous phase, along with the low processing temperature, allowed for improved oxidation resistance and successful fabrication in air. In addition to full amorphicity, the FFF material exhibited a fracture strength of 1220 MPa when loaded parallel to the deposited layers. This is near the fracture strength of the feedstock material (~1900 MPa) and is higher than any other AM BMG, according to Gibson et al..

Like the pneumatic injection method, material extrusion does not require melting of the feedstock material; therefore, devitrification due to thermal annealing or oxygen contamination is unlikely, assuming adequate control over time-at-temperature. In addition, because no steep thermal gradients exist, the complex thermomechanical stresses, commonly found in as-built AM parts, are likely not present in FFF metallic glass. These features of FFF are particularly advantageous since devitrification and stress-induced cracking are frequently reported during metallic glass fabrication using other AM techniques.

Challenges during Additive Manufacturing of Metallic Glass

Optimization of Powder Size and Morphology

Powder bed fusion and DED are typically completed using GA powder, and therefore the feedstock contains atomization defects such as trapped gas porosity and powder satellites. These defects can influence solid density and mechanical properties; however, in small concentrations they have minimal impact. In addition, particle morphology and size distribution are influential during AM-fabrication. The morphology of the glass-forming powders used for PBF ranged from highly spherical (Fischer et al., 2005; Jung et al., 2015; Koptuyug et al., 2013; Li et al., 2016, 2014a, 2014b; Pauly et al., 2013; Yang et al., 2018) to elongated, ‘pollywog’ shaped particles (Drescher and Seitz, 2015; Fischer et al., 2005; Jung

et al., 2015; X. P. Li et al., 2015; Zito, 2017). The prominence of elongated particles in metallic glass powder is due in part to alloy design. Metallic glass alloys are designed with a negative heat of mixing between the main constituent elements to impede atomic rearrangement and improve GFA; subsequently, their melt viscosity is three orders of a magnitude larger than that of binary alloys (Telford, 2004). The elongation of metallic glass particles during GA is therefore viscosity dominated (Yaginuma et al., 2015). In one example, Zito reported the occurrence of elongated glass-forming $\text{Au}_{76.26}\text{Ag}_{4.69}\text{Pd}_{1.93}\text{Cu}_{13.5}\text{Si}_{3.62}$ particles due to an imperfect ratio between the atomization temperature and the high melt viscosity of the alloy (Zito, 2017). Non-spherical powder morphology affects powder bed density and as-fabricated part density. In EBM, non-spherical powder morphology can cause excessive powder charging and smoking.

The particle size distribution dictates layer thickness and also affects powder flowability, spreadability, reactivity, and laser absorptivity during AM. The laser/powder interaction time is extremely short during LPBF processing (X. P. Li et al., 2015), so only the particle skins are rapidly heated. The core of a particle is heated and melted through thermal diffusion (Simchi, 2006). As particle size increases, the reduction in surface area leads to a lower laser absorptivity and core temperature of the particle may be less than the melting temperature (Yadroitsev et al., 2010). For example, Guo et al. tested the feasibility of developing laser melting parameters for 45-75 μm and 75-180 μm sized $\text{Nb}_{52}\text{Si}_{20}\text{Ti}_{24}\text{Cr}_2\text{Al}_2$ (at. %) powder with layer thicknesses of 80 and 200 μm , respectively (Guo et al., 2017). A reduced melt volume resulting from inadequate thermal transfer in large size $\text{Nb}_{52}\text{Si}_{20}\text{Ti}_{24}\text{Cr}_2\text{Al}_2$ (at. %) particles caused discontinuities in laser melt tracks in the 200 μm layers (Guo et al., 2017). Thermal conductivity of an AM powder bed also changes with

particle size. A powder bed with larger sized particles has a higher thermal conductivity, assuming equal bed porosity as a bed with smaller sized particles. The microstructure of metallic glass is highly sensitive to its thermal history; therefore, metallic glass alloys are affected by changes in laser absorptivity and thermal conductivity caused by the differences in powder size. For example, Zhang et al. laser melted layers of $Zr_{55}Cu_{30}Al_{10}Ni_5$ (at. %) using three different powder size distributions, 53-75 μm , 75-106 μm and 106-150 μm (Y. Zhang et al., 2015). The laser processing parameters were identical, however, the amorphous content of laser-fabricated solid was 90.8%, 78.7% and 75.1% for the 53-75 μm , 75-106 μm and 106-150 μm powder distributions, respectively. Zhang et al. suggested that melt pools formed in the 53-75 μm sized powder bed reached a higher maximum temperature than the melt pools formed in the 75-106 μm or 106-150 μm sized powder beds. This increase in heating temperature and time allowed pre-existing crystals and quenched-in nuclei to dissolve from the melt, so crystallization was reduced. The 106-150 μm powder bed was not heated to the same extent due to particle size dependent differences in laser absorptivity and thermal conduction, therefore, pre-existing crystals, nuclei and atomic clusters were inherited from the powder, acted as crystal nucleation sites during AM reheating cycles and caused increased crystal content (Y. Zhang et al., 2015). The inheritance of quenched-in nuclei has been noted by other researchers as well (Balla and Bandyopadhyay, 2010; Lin et al., 2019; Zheng et al., 2009a).

Results by Zhang et al. imply that smaller particle sizes may improve metallic glass processability during LPBF. However, it is important to note the increase in powder reactivity with decreasing particle size. The GFA of certain metallic glass alloys is hypersensitive to oxygen contamination. As particle size decreases, the increase in surface

area allows for more oxygen adsorption. Zhang et al. suggest that powder size distribution has a more significant influence on thermal behavior than the oxygen content during AM.

Contamination of Feedstock and during Manufacturing

Powder purity is essential for successful AM processing of metallic glass since impurities can reduce GFA and induce crystallization. Oxides act as heterogeneous nucleation sites and can promote the formation of metastable quasicrystalline phases that have a lower activation energy than a competing primary crystalline phase (H. Li et al., 2009; H. X. Li et al., 2009). For example, Zhang et al. reported the oxygen content of small (53-75 μm), medium (75-106 μm) and large (106-150 μm) sized $\text{Zr}_{55}\text{Cu}_{30}\text{Al}_{10}\text{Ni}_5$ (at. %) powder: 1700 ppm, 1600 ppm and 1800 ppm, respectively (Y. Zhang et al., 2015). Laser melting was performed under an inert argon atmosphere with only 15-35 ppm oxygen in the chamber. Metastable NiZr_2 -type nanocrystals precipitated in the HAZ of the AM solid. Murty has shown that during devitrification of a similar alloy, $\text{Zr}_{65-x}\text{Cu}_{27.5}\text{Al}_{7.5}\text{O}_x$ (at. %), the oxygen content promoted the formation of the NiZr_2 -type crystals (Murty et al., 2000). The NiZr_2 -type phase has a low interfacial energy and can therefore nucleate with less energy compared to other phases (Gebert et al., 1998). In addition, a needle shaped $\text{Cu}_{10}\text{Zr}_7$ -type phase was identified; it was predicated to be a result of pre-existing, quenched-in nuclei (Y. Zhang et al., 2015). Zhang et al. suggest that crystallization in the HAZ can be eliminated through reduction of oxygen content in the virgin powder and through optimization of the laser parameters (Y. Zhang et al., 2015; Zhang et al., 2016). Superheating during melting can dissolve pre-existing nuclei and oxides (Kim et al., 1998; Lin et al., 1997; Liu et al., 2012; Zhang et al., 2016); however, if a melt is overheated too much, oxygen pickup and oxide induced crystallization occur due to increased chemical activity at high temperatures (Li et

al., 2016). For this reason, it is important to optimize the maximum temperature, eliminating quenched-in nuclei while not inducing oxygen adsorption (Mao et al., 2009).

The reactivity of the high surface area feedstock means that powder is subject to oxidation during handling. In addition, the non-vacuumed chamber in most AM machines can cause oxygen pickup during melting. For example, Pauly et al. characterized bulk specimens of $Zr_{52.5}Cu_{17.9}Ni_{14.6}Al_{10}Ti_5$ manufactured in a SLM50(H) Realizer. The oxygen content of the virgin powder was 520 ± 10 ppm. The AM parts contained 970 ± 20 ppm oxygen; this is an order of magnitude larger than the oxygen level in an as-cast rod of the same alloy, 77 ± 5 ppm. The high oxygen content in the AM solid likely stabilized the presence of the metastable big cube, $NiTi_2$ -type phase detected during XRD analysis (Pauly et al., 2017). Contaminates other than oxygen also deteriorated the GFA during AM of metallic glass. The existence of contaminants including $Cu = 0.035$ wt. %, $Ni = 0.23$ wt. % and $Ti = 0.46$ wt. % were detected as probable causes of crystallization in a laser-melted $Fe_{74}Mo_4P_{10}C_{7.5}B_{2.5}Si_2$ (at. %) alloy (Pauly et al., 2013).

Despite a deterioration in GFA with oxygen, the high cooling rates achieved during LPBF allowed the production of fully-amorphous $ZrCuAlNb$ components, larger than the critical casting thickness, out of a poor quality (higher oxygen content) powder (Bordeenithikasem et al., 2018b). Similarly, Deng et al. measured 930 ± 25 ppm oxygen in glass-forming $Ti_{47}Cu_{38}Zr_{7.5}Fe_{2.5}Sn_2Si_1Ag_2$ powder (Deng et al., 2018). Interestingly, sharp reflections corresponding to the Ti_2Cu , Ti_3Cu_4 and $TiCu$ phases were identified in the powder even though the cooling rate during GA should have been sufficient to avoid crystallization ($t_c = 7$ mm). After laser melting, the oxygen content increased to 1250 ± 40 ppm; however, XRD analysis showed no sharp reflection peaks. Fast cooling during laser melting likely

prevented chemical segregation and hindered the nucleation and growth of the ti-rich, Ti_2Cu phase. The T_g , T_x , and enthalpy of crystallization of the laser-melted solid was within the experimental error of a cast sample, so the oxygen did not measurably deteriorate the GFA for the Ti-based.

Chemical Segregation in the Melt Pool

The shift in local composition due to chemical segregation can cause crystallization in glass-forming alloys. During laser/melt pool interaction, two melt flow patterns can occur: damped capillary oscillation and thermocapillary flow (Ma, 2015). The liquid oscillation and thermocapillary waves can induce elemental segregation in the melt (Liu et al., 2011). Electron microprobe analysis of high energy density (53.3 J/mm^3) laser-melted $Zr_{52.5}Cu_{17.9}Ni_{14.6}Al_{10}Ti_5$ (at. %) revealed an uneven and wave-shaped distribution of Zr, Cu, Ni, Al and Ti in a melt pool. Similarly, elemental distribution maps by Guo et al. and Sun and Flores show a distinct swirl-like pattern, and a heterogeneous distribution of the main elements in the melt pools of laser melted metallic glass (Guo et al., 2017; Sun and Flores, 2008). Li et al. noticed that the elemental distribution of the melt pool became more homogenous as laser energy density decreased during $Zr_{52.5}Cu_{17.9}Ni_{14.6}Al_{10}Ti_5$ (at. %) processing (Li et al., 2016), and at an energy input of 13.3 J/mm^3 , the elements were evenly distributed within a melt pool. Likewise, an energy input of 5.35 J/mm^3 was sufficient to achieve full vitrification and avoid chemical segregation during laser melting of $Ti_{47}Cu_{38}Zr_{7.5}Fe_{2.5}Sn_2Si_1Ag_2$ (Deng et al., 2018).

Minor changes in chemistry can drastically affect the GFA of metallic glass, so chemical homogeneity is a requirement for successful processing. The chemical inhomogeneity caused by melt flow at high energy densities could induce crystallization even

when the cooling rate is greater than the critical cooling rate (Li et al., 2016, 2014b).

Alternatively, Pauly et al. suggest that the chemical heterogeneity found in the melt pool might be a consequence, not the source, of partial crystallization because precipitation of the alloy they processed, $Zr_{52.5}Cu_{17.9}Ni_{14.6}Al_{10}Ti_5$ (at. %), would require significant atomic diffusion (Pauly et al., 2017). Regardless, in work by Li et al., a scanning strategy was introduced where each layer was scanned four times to average the melt flow and compensate for the uneven distribution of force during a single melt. They found that scanning each layer multiple times created the most homogeneous and amorphous structure (Li et al., 2016).

Devitrification in the Heat Affected Zone

During LPBF, DED and sheet lamination, laser melting can provide sufficient cooling rates in the melt pool and HAZ for full amorphization (Ouyang et al., 2017, 2018b; C. Zhang et al., 2018). Despite rapid solidification, crystallization in the HAZ is commonly observed in laser-fabricated material (Guo et al., 2016; Lin et al., 2019; Lu et al., 2019, 2018, 2017; Ouyang et al., 2018a, 2018b, 2017; Shen et al., 2017a; Sun and Flores, 2013, 2010, 2008; Xu et al., 2019; Yang et al., 2012; Ye and Shin, 2014; Y. Zhang et al., 2018; Zheng et al., 2009a).

The crystals found in the HAZ are typically nano-sized, spherulitic and surrounded by an amorphous matrix. Many have suggested that the reheating of the amorphous phase during subsequent layer and track deposition results in structural relaxation in the HAZ (Lin et al., 2019; Lu et al., 2019; Xu et al., 2019). This structural relaxation may result in the formation of nuclei and/or nano-crystals. Ouyang et al. examined the diffraction rings of the amorphous phase surrounding the crystals in the HAZ and melt pool of LPBF-fabricated

Zr₅₅Cu₃₀Ni₅Al₁₀. The diffraction ring of the HAZ amorphous phase was larger than that of the melt pool amorphous phase indicating that the atomic distance was shorter and that structural relaxation did occur (Ouyang et al., 2018a). Since the HAZ is structurally relaxed and partially crystallized, any post-heat treatments, even if below the feedstock material's T_x, would likely lead to the growth of pre-existing nuclei or nano-crystals.

Sun and Flores showed that there was no compositional segregation at the spherulitic crystal growth front of laser deposited ZrCuNiAlNb metallic glass. Unlike for multiphase nanocrystallization (common during slow heating rates), long-range atomic diffusion and phase separation are not a requisite for spherulitic crystallization in the HAZ (high heating rates) (Sun and Flores, 2013). Instead, microstructural observations suggest that the rapid heating during laser melting suppresses nucleation and bypasses phase separation, resulting in a crystallization mechanism dominated by rapid spherulitic growth from quenched-in nuclei or atomic clusters. Without the requirement for phase separation and long-range atomic diffusion, the activation energy for spherulitic crystallization is half of that for required for multiphase nanocrystallization, based on calculations by Sun and Flores. Furthermore, the significant difference in the temperature at which maximum nucleation and growth occur, along with the presence of quenched-in nuclei, results in a distinct asymmetry in the critical cooling and heating rates required to prevent crystallization and devitrification of metallic glass (Schroers et al., 1999). Lu et al. calculated the TTT diagram for a Zr-based BMG; the diagram showed a pronounced asymmetry between the critical heating and cooling rates (Figure 1) (Lu et al., 2017). Combining this TTT diagram with their thermal cycle curves, they determined that crystallization in the HAZ was caused by insufficient heating rates during thermal cycling.

The size and degree of crystallization in the HAZ is affected by the processing parameters. At larger energy densities the cooling rates remain sufficient for amorphization, however the size and time-at-temperature of the HAZ increases thereby allowing for increased nucleation and growth of crystals (Lu et al., 2019; Ouyang et al., 2018b). While it has proven difficult in practice, molecular dynamics simulations advocate that full amorphization, even in the HAZ, is attainable given the appropriate processing parameters (Guo et al., 2016, p. 201; Y. Zhang et al., 2018). Crystallization in the HAZ is also highly contingent on the thermal stability of the alloy composition (Ouyang et al., 2018b); however, thus far, no researchers have targeted metallic glass chemistries with high thermal stabilities as a means to eliminate crystallization in the HAZ.

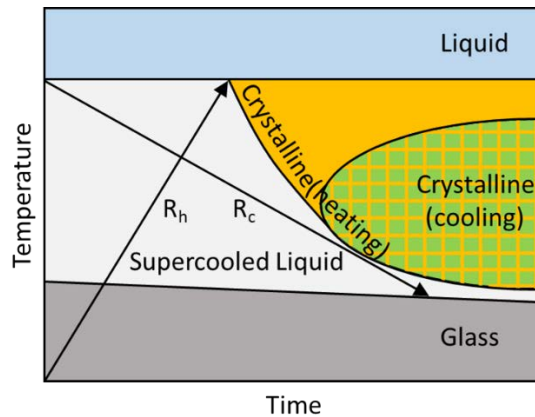


Figure 1. Time-temperature-transformation diagram of a bulk metallic glass showing a difference in critical cooling (R_c) and heating (R_h) rate. Recreated from (Lu et al., 2017).

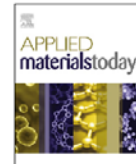
Chapter Summary

Thus far, research regarding the AM of metallic glass has fixated on process development. This research has led to the production of metallic glass components with dimensions or geometries not producible using any other manufacturing technique. Despite

these successes, researchers still struggle to prevent devitrification and cracking during AM of most metallic glass compositions. These challenges have shifted the research focus towards modeling and understanding cracking and devitrification of metallic glass in AM, and then adapting the AM equipment and processing parameters to accommodate the unique requirements for metallic glass. Although researchers identified the need to adjust AM equipment and parameters to improve the quality of AM metallic glass components, no group has targeted a glass-forming chemistry based on AM process requirements (based on the literature surveyed in this work). Instead, chemistries were chosen based on familiarity from other processing techniques, such as casting or melt spinning. Consequently, the alloy compositions used thus far exhibited poor AM processability, evident by their propensity to crack or devitrify regardless of process development efforts. These results indicate that there is a need to identify compositions with higher crack resistance and better AM processability than the ones previously selected. If a metallic glass composition is designed for AM to have a high GFA, thermal stability and crack resistance, then the AM production should be straightforward given the significant work contributed towards process development thus far.

**CHAPTER 3: ADDITIVE MANUFACTURING OF AN IRON-BASED BULK
METALLIC GLASS LARGER THAN THE CRITICAL CASTING THICKNESS**

Mahbooba, Z., Thorsson, L., Unosson, M., Skoglund, P., West, H., Horn, T., Rock, C., Vogli, E., Harrysson, O., 2018. Additive manufacturing of an iron-based bulk metallic glass larger than the critical casting thickness. *Applied Materials Today* 11, 264–269.
<https://doi.org/10.1016/j.apmt.2018.02.011>



Additive manufacturing of an iron-based bulk metallic glass larger than the critical casting thickness

Zaynab Mahbooba^{a,b}, Lena Thorsson^b, Mattias Unosson^b, Peter Skoglund^b, Harvey West^a, Timothy Horn^a, Christopher Rock^a, Evelina Vogli^c, Ola Harrysson^{a,b,*}

^a Center for Additive Manufacturing and Logistics, North Carolina State University, 126 Daniels Hall, Raleigh, NC 27607, USA

^b Sindre Metals, 8919 Scotch Castle Drive, Raleigh, NC 27612, USA

^c Liquidmetal Coatings, 26497 Rancho Parkway South, Lake Forest, CA 92630, USA

ARTICLE INFO

Article history:

Received 21 September 2017

Received in revised form 26 February 2018

Accepted 27 February 2018

Keywords:

Additive manufacturing

Amorphous metal

Bulk metallic glass

Fe

Direct metal laser sintering

ABSTRACT

Fe-based bulk metallic glasses (BMG) are of increasing research interest, driven in part by a unique combination of mechanical, magnetic and chemical properties. However, the maximum thickness and geometry of BMGs achievable in traditional manufacturing processes is limited. This work examines the capabilities of laser based powder bed additive manufacturing (AM) to produce relatively large Fe-based bulk metallic glass specimens. AM fabricated specimens exceed the critical casting thickness of the material by a factor of 15 or more in all dimensions. Resulting microstructural and mechanical properties are reported. Despite decreasing quench effect with increasing build thickness, X-ray diffraction analysis suggests that a fully amorphous structure was maintained throughout the build. However, a low concentration of sparsely distributed nano-grain clusters was discovered using a high-resolution electron backscatter diffraction scan. The results pave the way for novel applications of metallic glasses achievable through appropriate material design and optimization of existing additive manufacturing processes.

© 2018 Elsevier Ltd. All rights reserved.

1. Introduction

Metallic glasses form when molten metal is rapidly solidified to avoid crystallization. Vitrification occurs when the liquid cools below the glass transition temperature with a sufficiently high rate of solidification (typically on the order of 10^5 – 10^6 K/s) [1–3]. Unlike crystalline metals, the atoms in metallic glasses have no long-range atomic order, however short and medium-range order has been observed [3,4].

Metallic glasses containing a ferrous transition metal (Fe, Co, or Ni) as the main constituent are highly valued for their soft magnetic properties, mechanical properties, low damping coefficient and low material cost [2]. The homogeneous glassy microstructure, free of crystalline defects, removes magnetocrystalline anisotropy resulting in low hysteresis losses [2,5,6], and the absence of grain boundaries also leads to excellent corrosion and wear resistance [1–3,5]. This unique combination of magnetic properties and high strength make Fe-based metallic glasses an optimal choice for applications such as magnetic shielding or transformer core

laminations [6]. However, the requirement for rapid solidification restricts metallic glass production to relatively thin geometries using techniques such as melt spinning, vapor deposition and atomization [1,7]. These processing challenges coupled with low ductility have severely limited the potential uses of Fe-based metallic glasses as a structural material [8].

Research efforts have therefore focused on designing metallic glass alloys with greater glass forming ability (GFA). Bulk metallic glasses (BMGs) have been reported with critical cooling rates on the order of 1 – 10^3 K/s, and thicknesses greater than 1 cm [5,7,9]. For example, $Zr_{41}Ti_{14}Cu_{12.5}Ni_{10}Be_{22.5}$ has a maximum casting thickness between 5 and 10 cm [10]. Likewise, alloy $Fe_{48}Cr_{15}Mo_{14}C_{15}B_6Er_2$ has full amorphicity when cast in thicknesses of up to 12 mm [11]. Solidification rates necessary to obtain an amorphous microstructure impose a dimensional constraint on BMGs called the critical casting radius (R_c) [9,12]. BMGs cast into thicknesses up to the R_c will fully vitrify only if material contamination is minimized in the base material and during processing. Along with casting, powder metallurgy techniques such as hot pressing and spark plasma sintering are also used to produce BMGs. Certain strong glass forming BMGs can be produced into more complex shapes using thermoplastic forming. However, these often contain toxic (e.g. Be) or expensive elements (Pt, Pd, Au), limiting the viability of large-scale production [13].

* Corresponding author at: Center for Additive Manufacturing and Logistics, North Carolina State University, 126 Daniels Hall, Raleigh, NC 27607, USA.

E-mail address: harrysson@ncsu.edu (O. Harrysson).

<https://doi.org/10.1016/j.apmt.2018.02.011>

2352-9407/© 2018 Elsevier Ltd. All rights reserved.

Recently, researchers have attempted to produce BMGs using additive manufacturing (AM) [14–21]. A Swedish company, Exmet, was the first group to demonstrate the feasibility of this technique [22,23]. In powder bed AM, layers of metal powder ranging from approximately 20–100 μm in thickness are spread across a platform and selectively melted by a laser or electron beam energy source. The cooling rate per layer can reach 10^3 – 10^4 K/s, and is dependent on build parameters, layer thickness, alloy composition and part geometry. Heating and cooling rate of BMGs during AM laser processing has been modeled by [18,24–27]. The layer-by-layer melt process enables the opportunity to produce BMGs thicker than R_c , since local cooling rate is higher than the critical cooling rate. In addition, AM is able to produce near net shape components with complex and intricate geometries, unmatched by current BMG production techniques.

Jung et al. used selective laser melting (SLM) to fabricate fully amorphous FeSiBPCrMoAl samples measuring 6×20 mm ($R_c = 3$ mm) with a density of 99.7%. Despite the high density, the presence of micro-pores and fine cracking poorly affected the magnetic properties of the specimens. Cracking was attributed to thermal stresses caused by the temperature gradient between processed layer and the cold layers beneath it, and the friability of Fe-based BMGs. The authors postulated that build plate heating could potentially reduce the temperature difference between the solidified material and the melting layer to mitigate cracking [14]. Ye and Shin were able to produce crack-free FeCrMoWMMnCSiB using laser direct deposition by pre-heating the build substrate to 422 °C. However, the samples were not fully amorphous due to the precipitation of a CrFe crystalline phase [17].

Most BMGs processed using powder bed AM reported in the literature did not exhibit full vitrification. For example, Zheng et al. reported crystallization in the first layer of Fe-based BMG during directed energy deposition (laser-engineered net-shaping). The fraction of the crystalline phase increased as a function of build thickness [16]. Ye and Shin observed grain nucleation exclusively in layer overlap regions where material re-melting led to devitrification [17]. Li et al. produced a heavily crystallized AlNiYCoLa BMG alloy using SLM; they showed that devitrification had resulted from chemical inhomogeneity in the melt pool caused by laser induced liquid oscillation [21]. In addition, material contamination [20] and incomplete melting of crystalline starting powder [15] have also been reported to contribute to crystallization of metallic glasses in AM.

While significant work has been contributed to the literature, no report has been identified demonstrating a fully dense and amorphous BMG produced with AM, nor have any samples exceeded the critical casting thickness, using any manufacturing method. FeCrMoCB is a well-documented glass-forming alloy [28–30] that is optimized for thermal spray applications where excellent strength and hardness are required. FeCrMoCB has a critical casting thickness <2 mm when synthesized using copper mold casting [31]. This work reports the additive manufacturing of an amorphous alloy larger than the critical casting thickness using the direct metal laser sintering (DMLS) process (Electrical Optical Systems, Krailling, Germany).

2. Materials and methods

Gas atomized FeCrMoCB powder was produced by LiquidMetal® Coatings with a nominal particle size distribution of 20–80 μm . Powder size distribution was measured using a Microtrac S3500 laser diffraction particle size analyzer, and morphology was examined using scanning electron microscopy (JEOL 6010 LA SEM). Additionally, X-ray diffraction (XRD) (Rigaku SmartLab) was used to examine the amorphicity of the powder.

Selective laser melting was performed in an EOSINT M 280 system equipped with a 200 W Yb-fiber laser. During processing, the build chamber was flooded with argon gas to limit the oxygen content (<1000 ppm). During initial process parameter development, the sample geometry consisted of 9 mm diameter cylinders 15 mm tall. These were fabricated onto stainless steel build substrates. The build substrates consisted of $15.24 \times 1.90 \times 0.63$ cm ground 4140 steel inserts, bolted into matching pockets milled into the standard EOS build platform. This setup facilitated rapid sample removal and preparation.

The build substrate temperature and layer thickness are not adjustable parameters in the EOS M 280. Pre-set equipment parameters allowed for a build plate temperature of 80 °C and layer thickness of 20 μm . The 20 μm layer thickness is smaller than the maximum particle size of the FeCrMoCB powder (20–80 μm), this is common for DMLS processing parameters. Excessively large particles will not be spread by the recoat blade. However, particles larger than 20 μm will still be used due to solidification shrinkage of the solid and powder bed densification.

A wide range of heat inputs ($i = P/vh$, where P is laser power, v is the laser scanning speed, and h is the hatch spacing) were analyzed to determine the feasible processing window for the FeCrMoCB alloy. Heat input values that drastically over- or under-melted the material were excluded from further testing. Laser power, beam speed and hatch spacing were systematically varied from 80 to 200 W, 800 to 5000 mm/s and 0.05 to 0.15 mm, respectively, using a fractional factorial design of experiments. In addition, different scanning strategies were implemented by varying the scan vector width (stripe width), scan vector overlap (stripe overlap) and the scanning pattern (hatch style).

After AM fabrication, cylinders were inspected for dislodged particles or surface cracking. Surface roughness measurements were not collected since no effort was made to optimize the parameter set that dictates roughness, the contour parameters. Density was measured using Archimedes' method in acetone, then compared to the density of a cast and hot isostatic pressed reference sample. XRD analysis was performed on cylinder cross-sections along the build plane. Based on density and XRD analyses, laser processing parameters were altered for subsequent tests, iteratively, to produce dense samples that exhibited an amorphous structure.

Based on the results of the preliminary parameter search, two cylinders measuring 30×450 mm were produced using the optimized process settings. A low speed saw (Buehler IsoMet), was used to section one cylinder perpendicular to the build direction into three segments. These sections were examined using Archimedes density, XRD, optical and scanning electron microscopy and electron backscatter diffraction (EBSD) analyses. For SEM analysis (FEI Quanta 3D FEG), samples were ground, polished, and then etched by swabbing with aqua regia for 15 s. SEM analysis, in backscatter and secondary electron modes, was employed to visually search for a crystalline phase on the etched sample surface. Using an Oxford EBSD detector, a large surface area was manually scanned until a diffraction pattern was detected. If a grain was identified, an orientation map 1500×1500 nm was collected with a step size of 10 nm.

Vickers microhardness indentation resulted in crack initiation and growth at the indent site. Nano-indentation uses a lower load than micro-indentation, so the occurrence of cracking was reduced. Nano-indentation measurements from the polished surface of SLM-fabricated cylinders were acquired with an Anton Paar Ultra Nano-indentation Tester with a Berkovich diamond tip. The average of 21 measurements was calculated, along with elastic modulus. Coefficient of restitution (C_R) was estimated using a stainless steel ball bearing drop test on the AM bulk cylinder and compared to the same for a stainless steel surface. This approach to measuring C_R was based on previous work by Schnurmann [32].

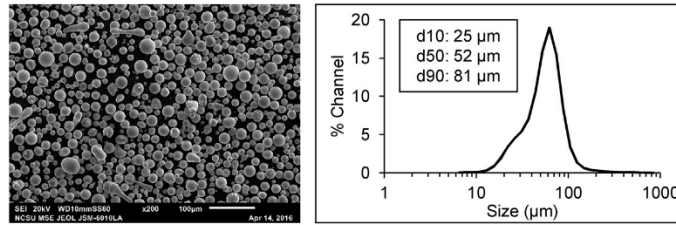


Fig. 1. Powder: Powder morphology (left) and size distribution (right) of virgin FeCrMoCB powder used for DMLS processing.

The surface of the second 45 mm diameter AM fabricated sample was polished, and an acrylic tube with an inner diameter of 45 mm and a height of 1.0 m was placed over the cylinder. A stainless steel ball bearing was dropped 0.7 m into the tube and onto the cylinder surface. The drop test was digitally recorded at 240 Hz, and frame-by-frame analysis was used to determine the drop height and bounce height. Neglecting frictional forces, C_R was calculated using, $C_R = \sqrt{h/H}$ where h is the first bounce height and H is the drop height. Lastly, combustion analysis was used to assess the oxygen composition of the as-fabricated bulk cylinder, as well as the feedstock powder.

3. Results

The powder size distribution of FeCrMoCB used in this study is shown in Fig. 1. The 10th and 90th percentiles are 25 μm and 81 μm , respectively. SEM analysis indicates that the powder morphology is mostly spherical, although particles exhibiting a high aspect ratio can also be observed.

During the initial laser parameter search, FeCrMoCB samples, shown in Fig. 2 (bottom), exhibited significant cracking and friability. Despite the minimal contact between the recoater blade and the FeCrMoCB sample, pieces of material were torn from cylinders during powder recoating (Fig. 2 top). Further development resulted in a processing space that consistently produced samples that matched intended geometry and build height.

Fig. 3 shows a 30 \times 45 ϕ mm specimen. No cracking or layer delamination was evident by visual inspection of the exterior surface, but micro-cracking was observable within the bulk material during the building process. Cracking caused by a micro-indentation test, shown in Fig. 4, indicates the brittleness of the DMLS fabricated material. The XRD spectrum of the FeCrMoCB virgin powder, shown in Fig. 5, shows a wide halo peak with a low intensity corresponding to a fully amorphous structure. XRD results reported in Fig. 5 showing the bottom, middle and top sections along the 30 \times 45 ϕ mm bulk cylinder, suggest that amorphicity was preserved during laser processing. Comparatively, a cast and hot isostatic pressed FeCrMoCB reference sample shows several sharp, high-intensity peaks corresponding to Bragg diffraction. An EBSD orientation map of a nano-grain cluster is shown in Fig. 6. Black portions represent amorphous regions of material while the colored regions are grains ($d < 300 \text{ nm}$) that were sporadically observed in low concentrations (<1% volume) throughout the cross section of the sample.

Table 1 provides the Archimedes density measurements of the bottom, middle and top sections of the bulk cylinder as compared to a hot isostatic pressed reference. Density measurements show an increase in density with build height from 96.5% to 97.7%. Average density of the 30 \times 45 ϕ mm cylinder is 97%. Nano-indentation testing yielded an average hardness of 9736 MPa (equivalent to $H_V = 902$) for the DMLS-fabricated FeCrMoCB samples. In addition, nano-indentation data was used to approximate an elastic modulus of 220 GPa (Poisson's ratio was estimated at 0.3 for this alloy



Fig. 2. Process development: Photograph of DMLS samples during the early stages of process development.

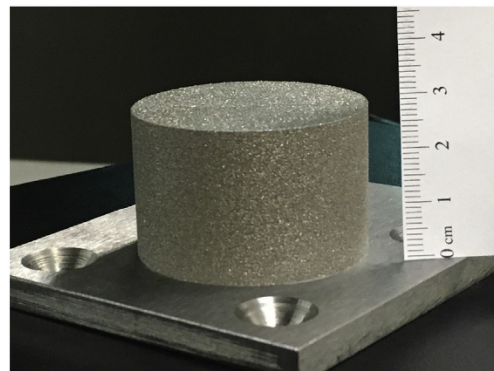


Fig. 3. DMLS-fabricated BMG; 30 \times 45 ϕ mm FeCrMoCB bulk cylinder produced using DMLS.

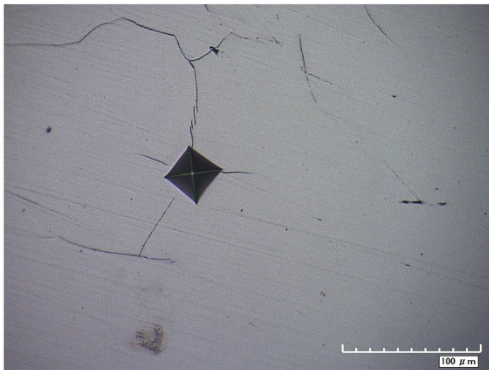


Fig. 4. Indent cracking: A micro-hardness indentation in DMLS-fabricated FeCrMoCB. Cracking caused by the indentation demonstrates the friability of FeCrMoCB.

[31]). The coefficient of restitution was estimated using a stainless steel ball bearing drop test. When dropped on the DMLS-fabricated BMG cylinder ($30 \times 45 \text{ mm}$), the ball bounced back to almost 100% of the initial drop height. Dissimilarly, the same test performed on a stainless steel surface generated a bounce only one third of the initial drop height. The coefficient of restitution for the DMLS-fabricated BMG was observed at $C_R = 0.97$, while the stainless steel test yielded $C_R = 0.60$. Furthermore, oxygen content of the virgin powder and bulk cylinder were measured at 0.087 and 0.075 at. %, respectively.

4. Discussion

Laser processing techniques, such as laser welding, laser cladding and DMLS, are associated with high residual stresses due to the large thermal gradient associated with rapid solidification. Residual stresses inherent to DMLS result in geometric distortion, layer delamination, cracking and curling. Typical post processing of DMLS-fabricated material includes a stress relieving heat treatment. It is impractical to heat treat BMGs, since heating above the crystallization temperature would induce grain nucleation and

Table 1

Archimedes density measurements of the FeCrMoCB bulk cylinder bottom, middle and top sections with standard deviation.

	Archimedes density
Top	$97.7\% \pm 0.2\%$
Middle	$97.1\% \pm 0.1\%$
Bottom	$96.5\% \pm 0.0\%$

growth. The intrinsic brittleness of metallic glass amplifies the detrimental effects of residual stress build-up. For this reason, the influence of thermal stress on DMLS-fabricated FeCrMoCB was drastic. Initial processing yielded samples that were prone to severe cracking and crumbling due to high stress during processing; samples never reached intended build height or geometry. Optimized processing parameters produced parts with no obvious surface defects upon visual inspection. Researchers investigating the AM of metallic glass alloys have also experienced difficulty overcoming stress-related cracking [14,16,21].

The alloy design of metallic glasses strongly influences the material's mechanical properties. Fe(CB)-based alloys, like the material selected for this work, exhibit the highest strength and lowest ductility of the Fe-based metallic glasses [33]. An investigation on the effect of boron content on a Fe(CB)-based BMGs revealed that boron additions $>1.5 \text{ at.}\%$ eliminate any plastic deformation prior to failure. The fracture surface of alloys with $<1.5 \text{ at.}\%$ boron exhibit a vein like pattern, indicative of plastic flow [33]. Oppositely, the Fe(CB)-based alloy containing $>1.5 \text{ at.}\%$ boron, like the alloy produced for this work, show no indication of plastic deformation before failure. Due to the compositionally induced brittleness of FeCrMoCB, the limited ductility inherent to BMGs and the high residual stresses in laser based processing, cracking was unavoidable during processing.

Laser heat treatment can reduce the thermal gradient between melting and solidified material, and can therefore facilitate in situ stress relief. Laser scanning pattern dictates the temperature distribution in the top layer of DMLS fabricated material. In this work, changes in laser scanning parameters diminished stresses to allow for the production of full-height, dimensionally accurate specimens. Reduction in residual stress via laser scanning pattern alteration was insufficient to eliminate the stress-induced

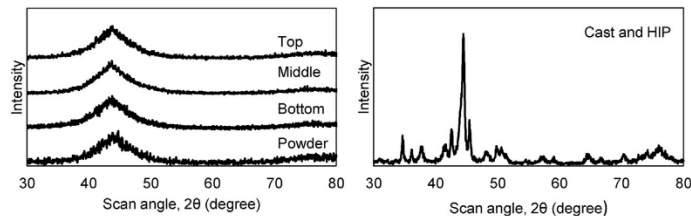


Fig. 5. X-ray diffraction: X-ray diffraction spectra of FeCrMoCB virgin powder, bulk cylinder (bottom, middle and top) and a hot isostatic pressed (HIP) reference sample.

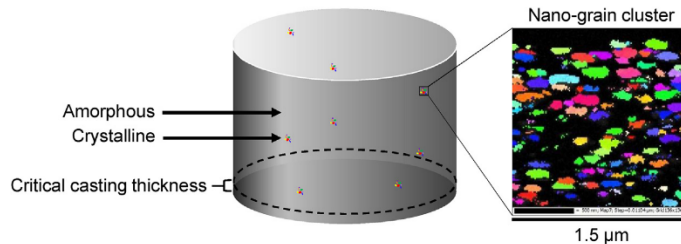


Fig. 6. Grain cluster in the bulk cylinder: EBSD micrograph collected at a nano-grain cluster in the FeCrMoCB bulk cylinder.

micro-cracking associated with rapid solidification of the low ductility FeCrMoCB alloy.

The densification of DMLS-fabricated materials is dictated by the processing parameters. Within the processing window used to produce the bulk cylinder, parameters were altered to maximize density. Increasing energy density by increasing laser power or decreasing scan speed effect the melt pool size and temperature. Too much energy input can lead to an increase in stresses or can cause beading of the molten metal as it breaks the surface tension. Too little energy input leads to incomplete melting of metal powder. Likewise, the hatch distance influences energy input into the powder bed and should be no larger than the diameter of the melt pool. The DMLS-fabricated bulk cylinder, pictured in Fig. 3, has an average density of 97%. The lack of large surface defects and high density of the cylinder suggest that the energy input was sufficient. It is likely that full density is achievable with the elimination of stress-induced micro-cracks within the bulk. Density is also influenced by the presence of spherical gas entrapment porosity, a product of gas atomization, and irregularly shaped keyhole pores. Keyhole pores are formed when the molten metal inadequately flows to fill gaps. The rapid solidification in DMLS and high viscosity of glass-forming metals do not allow adequate time for the molten material to flow into all gaps. Porosity in the DMLS cylinder was challenging to distinguish since cutting and grinding of the material induced cracking. Density measurements presented in Table 1 show an increase in density with sample height. As build height increases, poor heat transfer through the low conductivity FeCrMoCB material causes a reduction in the cooling rate. Slower cooling rates produce fewer stresses and therefore fewer density detrimental cracks are developed. In addition, the bottom layers experience prolonged thermal cycling; this could result in a lower density due to an increase in cracking as a result of structural relaxation embrittlement.

Accordingly, the 30×450 mm bulk cylinder showed full XRD amorphicity. Cooling rate per layer was sufficient to preserve amorphicity far above the critical casting thickness despite decreasing quench rate with build height. X-ray diffraction analysis is an accepted technique for obtaining an overview of microstructure, however, the resolution is limited. EBSD has higher resolution than XRD, and therefore can be used to detect smaller grains within the microstructure. EBSD analysis revealed the presence of a low concentration of nano-grain clusters. Temperature, contamination and mechanical stress are the predominant forces driving nucleation in metallic glasses [34]. Prolonged heat exposure and thermal cycling during AM are probable causes of nanocrystal nucleation. EBSD analysis showed that nano-grains exist only in localized clusters throughout the bulk FeCrMoCB cylinder; however, grain nucleation as a result of thermal annealing typically exhibits uniformly distributed grains [7]. Additionally, despite the directionality of heat flow in AM, nano-grains imaged are relatively equiaxial. Based on the localized and equiaxial nature of the nano-grains, it is unlikely that thermal annealing during DMLS processing provided the energy for grain nucleation. Alternatively, nucleation was possibly a result of oxygen contamination and/or mechanical stress.

Along with thermal annealing, impurities such as oxygen, can also induce crystallization in BMGs. Oxides act as heterogeneous nucleation sites and impact the glass formability. Furthermore, oxygen can promote the formation of metastable quasicrystalline phases that have a lower activation energy than a competing primary crystalline phase [35,36]. While it is well established that low concentrations of oxygen impurities have a detrimental effect on GFA in Zr-based metallic glasses [37,38], limited information is available on the role of oxygen in Fe-based BMGs. Li et al. report that oxygen additions between 0.02 and 0.15 at. % actually improved the GFA in a FeMoCSiBP BMG [36]. It was suggested

that the critical level of oxygen depressed the liquidus temperature and suppressed precipitation of a primary phase. In any case, oxygen concentrations >0.15 at.% promoted the formation of oxygen rich crystals and reduced the GFA [36]. Similar results are reported for a FeNiPC BMG, for which oxygen additions up to 0.0252 at.% improved thermal stability and did not induce crystallization [37]. A concentration of 0.075 at.% was measured in the DMLS-fabricated FeCrMoCB material. This oxygen concentration is within the range of oxygen additions that improved GFA for FeMoCSiBP. It is possible that oxygen contamination did not induce crystallization in this work; however, a comprehensive study of oxygen in FeCrMoCB would be required to assert this conclusion.

Mechanical stress is a well-known source of localized nanocrystal nucleation in and around shear bands in amorphous metals [34,39–42]. The underlying mechanism for stress-induced grain formation is not fully understood; however, it is of general consensus that the crystallization is caused by viscous flow or local heating [34,40]. Shear band formation and propagation dictates the plasticity of metallic glasses. During plastic deformation, local strain accumulates and a shear band is developed [43]. Metallic glasses can store more elastic strain energy per unit volume than crystalline metals. When the yield strength is surpassed, the stored elastic energy dissipates inside the shear bands and can cause a drastic increase in local temperature. Lewandowski and Greer reported a temperature increase >1000 K within nanoseconds inside a shear band [44]. The adiabatic heating often results in catastrophic failure and is a probable cause of local crystallization [39,43]. In contrast, others have suggested the stress-enhanced atomic diffusion at shear bands provides enough energy for nano-grain nucleation [39,41], particularly when dynamic loading or fracture do not occur [39]. Atoms that are not in the vicinity of shear bands are not supplied with enough energy to create grains. It is reasonable to assume that the stress-induced cracking that occurred during DMLS-processing provided sufficient energy for the nucleation of nano-grain clusters.

The AM bulk FeCrMoCB cylinder hardness was 902 HV. Nano-indentation data was used to approximate an elastic modulus of 220 GPa, assuming a Poisson's ratio of 0.3. This value is in close proximity to cast BMG alloys having similar composition (Young's modulus of 190–220 GPa) [31]. Coefficient of restitution represents a dynamic and more global hardness than nano-indentation. The C_R for the DMLS fabricated BMG was observed at $C_R = 0.97$, while the stainless steel test yielded $C_R = 0.60$. This drop test demonstrates the high elastic energy storage capacity and low dissipation of the BMG fabricated in this work, even with the presence of micro-cracks, compared to stainless steel.

5. Conclusion

In this work, we demonstrate the use of DMLS to produce a fully XRD-amorphous FeCrMoCB BMG whose thickness is more than 15 times the critical casting thickness in all dimensions, and larger than any traditionally produced Fe-based BMG recorded. The DMLS-fabricated BMG is 97% dense and has no major external cracks. Due to the brittleness associated with BMGs and the FeCrMoCB alloy, DMLS process parameter alteration alone was insufficient to eliminate all micro-cracking. Therefore, stress-induced micro-cracks, a product of the rapid solidification in laser processing, are still present within the bulk material. Continued work focuses on eliminating micro-cracks by targeting Fe-based BMG alloys with enhanced plasticity. Furthermore, a low concentration of nano-grains was exposed within the BMG microstructure. The localized and isotropic nature of the nano-grains suggest that nucleation was not a product of thermal annealing. Instead, mechanical stress induced crystallization

during DMIS processing. By eliminating micro-cracks through improved alloy design, stress-induced nucleation should subside. This work proves that DMIS is a suitable technique for the development of BMGs significantly larger than their critical casting thickness with mechanical properties rivaling that of their cast counterparts.

Acknowledgements

This material is based upon work supported by the National Science Foundation under Grant no. 1,549,770 awarded to Sindree Metals, Inc., a North Carolina SME. This work was performed in part at the Analytical Instrumentation Facility (AIF) at North Carolina State University, which is supported by the State of North Carolina and the National Science Foundation (award number ECCS-1542015). The AIF is a member of the North Carolina Research Triangle Nanotechnology Network (RTNN), a site in the National Nanotechnology Coordinated Infrastructure (NNCI).

References

- [1] A.L. Greer, *Metallic glasses*, *Science* 267 (1995) 1947.
- [2] M. Telford, The case for bulk metallic glass, *Mater. Today*, 7 (2004) 36–43, [http://dx.doi.org/10.1016/S1369-7021\(04\)00124-5](http://dx.doi.org/10.1016/S1369-7021(04)00124-5).
- [3] T.R. Anantharaman, *Metallic Glasses: Production, Properties and Applications*, Trans Tech Publications, Aedermannsdorf, Switzerland, 1984.
- [4] A.L. Greer, *Metallic glasses... on the threshold*, *Mater. Today*, 12 (2009) 14–22, [http://dx.doi.org/10.1016/S1369-7021\(09\)70037-9](http://dx.doi.org/10.1016/S1369-7021(09)70037-9).
- [5] M.F. Ashby, A.L. Greer, *Metallic glasses as structural materials*, *Scr. Mater.* 54 (2006) 321–326, <http://dx.doi.org/10.1016/j.scriptamat.2005.09.051>.
- [6] H.H. Liebermann, *I. Netlibrary, Rapidly Solidified Alloys: Processes, Structures, Properties, applications*, M. Dekker, New York, 1993.
- [7] A. Inoue, Stabilization of metallic supercooled liquid and bulk amorphous alloys, *Acta Mater.* 48 (2000) 279–306, [http://dx.doi.org/10.1016/S1359-6454\(99\)00300-6](http://dx.doi.org/10.1016/S1359-6454(99)00300-6).
- [8] V. Ponnambalam, S.J. Poon, G.J. Shiflet, Fe-based bulk metallic glasses with diameter thickness larger than one centimeter, *J. Mater. Res.* 19 (2004) 1320–1323, <http://dx.doi.org/10.1557/JMR.2004.0176>.
- [9] W.H. Wang, C. Dong, C.H. Shek, Bulk metallic glasses, *Mater. Sci. Eng. R Rep.* 44 (2004) 45–89, <http://dx.doi.org/10.1016/j.mser.2004.03.001>.
- [10] A. Peker, W.L. Johnson, A highly processable metallic glass: Zr₄₁Ti₁₃Cr₈Cu₁₂Sn₁₀Be₂₂S, *Appl. Phys. Lett.* 63 (1993) 2342–2344, <http://dx.doi.org/10.1063/1.110520>.
- [11] X.J. Gu, S.J. Poon, G.J. Shiflet, Mechanical properties of iron-based bulk metallic glasses, *J. Mater. Res.* 22 (2007) 344–351, <http://dx.doi.org/10.1557/jmr.2007.0036>.
- [12] W.L. Johnson, Bulk amorphous metal – an emerging engineering material, *JOM* 54 (2002) 40–43, <http://dx.doi.org/10.1007/BF02822619>.
- [13] A. Inoue, A. Takeuchi, Recent development and application products of bulk glassy alloys, *Acta Mater.* 59 (2011) 2243–2267, <http://dx.doi.org/10.1016/j.actamat.2010.11.027>.
- [14] H.Y. Jung, S.J. Choi, K.G. Prashanth, M. Stoica, S. Scudino, S. Yi, U. Kühn, D.H. Kim, K.B. Kim, J. Eckert, Fabrication of Fe-based bulk metallic glass by selective laser melting: a parameter study, *Mater. Des.* 86 (2015) 703–708, <http://dx.doi.org/10.1016/j.matdes.2015.07.145>.
- [15] V.K. Balla, A. Bandyopadhyay, Laser processing of Fe-based bulk amorphous alloy, *Surf. Coat. Technol.* 205 (2010) 2661–2667, <http://dx.doi.org/10.1016/j.surfcoat.2010.10.029>.
- [16] B. Zheng, Y. Zhou, J.E. Smugeresky, E.J. Lavermia, Processing and behavior of Fe-based metallic glass components via laser-engineered net shaping, *Metall. Mater. Trans. A*, 40 (2009) 1235–1245, <http://dx.doi.org/10.1007/s11661-009-9828-y>.
- [17] X. Ye, Y.C. Shin, Synthesis and characterization of Fe-based amorphous composite by laser direct deposition, *Surf. Coat. Technol.* 239 (2014) 34–40, <http://dx.doi.org/10.1016/j.surfcoat.2013.11.013>.
- [18] G. Yang, X. Lin, F. Liu, Q. Hu, L. Ma, J. Li, W. Huang, Laser solid forming Zr-based bulk metallic glass, *Intermetallics* 22 (2012) 110–115, <http://dx.doi.org/10.1016/j.intermet.2011.10.008>.
- [19] H. Sun, K.M. Flores, Microstructural analysis of a laser-processed Zr-based bulk metallic glass, *Metall. Mater. Trans. A* 41 (2010) 1752–1757, <http://dx.doi.org/10.1007/s11661-009-0151-4>.
- [20] S. Pauly, L. Löber, R. Petters, M. Stoica, S. Scudino, U. Kühn, J. Eckert, Processing metallic glasses by selective laser melting, *Mater. Today*, 16 (2013) 37–41, <http://dx.doi.org/10.1016/j.mattod.2013.01.018>.
- [21] X.P. Li, C.W. Kang, H. Huang, L.C. Zhang, T.B. Sercombe, Selective laser melting of an Al86Ni6Y4.5Co2La1.5 metallic glass: processing, microstructure evolution and mechanical properties, *Mater. Sci. Eng. A* 606 (2014) 370–379, <http://dx.doi.org/10.1016/j.msea.2014.03.097>.
- [22] A. Langlet, Method of producing products of amorphous metal, US8052923 B2, 2011, <http://www.google.com/patents/US8052923> (accessed 25.01.18).
- [23] P. Skoglund, A. Langlet, Method of producing objects containing nano metal or composite metal, US8333922 B2, 2012, <http://www.google.com/patents/US8333922>.
- [24] Y. Zhang, X. Lin, L. Wang, L. Wei, F. Liu, W. Huang, Microstructural analysis of Zr55Cu30Al10Ni5 bulk metallic glasses by laser surface remelting and laser solid forming, *Intermetallics* 66 (2015) 22–30, <http://dx.doi.org/10.1016/j.intermet.2015.06.007>.
- [25] S. Guo, M. Wang, Z. Zhao, Y.Y. Zhang, X. Lin, W.D. Huang, Molecular dynamics simulation on the micro-structural evolution in heat-affected zone during the preparation of bulk metallic glasses with selective laser melting, *J. Alloys Compd.* (2016), <http://dx.doi.org/10.1016/j.jallcom.2016.11.393>.
- [26] Y. Lu, H. Zhang, H. Li, H. Xu, G. Huang, Z. Qin, X. Lu, Crystallization prediction on laser three-dimensional printing of Zr-based bulk metallic glass, *J. Non-Cryst. Solids*, 461 (2017) 12–17, <http://dx.doi.org/10.1016/j.jnoncrysol.2017.01.038>.
- [27] Y. Shen, Y. Li, H.-L. Tsai, Evolution of crystalline phase during laser processing of Zr-based metallic glass, *J. Non-Cryst. Solids*, (2017), <http://dx.doi.org/10.1016/j.jnoncrysol.2017.11.001>.
- [28] S.J. Pang, T. Zhang, K. Asami, A. Inoue, Bulk glassy Fe–Cr–Mo–C–B alloys with high corrosion resistance, *Corros. Sci.* 44 (2002) 1847–1856, [http://dx.doi.org/10.1016/S0010-938X\(02\)00002-1](http://dx.doi.org/10.1016/S0010-938X(02)00002-1).
- [29] Z. Zhou, L. Wang, D.Y. He, F.C. Wang, Y.B. Liu, Microstructure and wear resistance of Fe-based amorphous metallic coatings prepared by HVOF thermal spraying, *J. Therm. Spray Technol.* 19 (2010) 1287–1293, <http://dx.doi.org/10.1007/s11666-010-9556-2>.
- [30] G.A. Croopnick, Iron-chromium-molybdenum-based thermal spray powder and method of making of the same, US20130052361 A1, 2013, <http://www.google.com/patents/US20130052361> (accessed 25.01.18).
- [31] C. Suryanarayana, A. Inoue, Iron-based bulk metallic glasses, *Int. Mater. Rev.* 58 (2013) 131–166, <http://dx.doi.org/10.1179/1743280412Y.0000000007>.
- [32] R. Schnurmann, Rate of energy loss from rebounding steel balls, *Proc. Phys. Soc.* 53 (1941) 662, <http://dx.doi.org/10.1088/0959-5309/53/6/305>.
- [33] C. Su, Y. Chen, P. Yu, M. Song, W. Chen, S.F. Guo, Linking the thermal characteristics and mechanical properties of Fe-based bulk metallic glasses, *J. Alloys Compd.* 663 (2016) 867–871, <http://dx.doi.org/10.1016/j.jallcom.2015.12.196>.
- [34] J.-C. Lee, Y.-C. Kim, J.-P. Ahn, H.-S. Kim, S.-H. Lee, B.-J. Lee, Deformation-induced nanocrystallization and its influence on work hardening in a bulk amorphous matrix composite, *Acta Mater.* 52 (2004) 1525–1533, <http://dx.doi.org/10.1016/j.actamat.2003.11.034>.
- [35] H. Li, Z. Lu, S. Yi, Estimation of the glass forming ability of the Fe-based bulk metallic glass Fe₆₈Cr₇Si₃B₅OP₉Cr₂Mo₂Al₂O that contains non-metallic inclusions, *Metals Mater. Int.* 15 (2009) 7, <http://dx.doi.org/10.1007/s12540-009-0007-x>.
- [36] H.X. Li, J.E. Gao, Z.B. Jiao, Y. Wu, Z.P. Lu, Glass-forming ability enhanced by proper additions of oxygen in a Fe-based bulk metallic glass, *Appl. Phys. Lett.* 95 (2009) 161905, <http://dx.doi.org/10.1063/1.3248186>.
- [37] H.X. Li, C.Q. Li, D. Cao, W.M. Yang, Q. Li, Z.P. Lu, Influences of oxygen on plastic deformation of a Fe-based bulk metallic glass, *Scr. Mater.* 135 (2017) 24–28, <http://dx.doi.org/10.1016/j.scriptamat.2017.03.018>.
- [38] C.T. Liu, M.F. Chisholm, M.K. Miller, Oxygen impurity and microalloying effect in a Zr-based bulk metallic glass alloy, *Intermetallics* 10 (2002) 1105–1112, [http://dx.doi.org/10.1016/S0966-9795\(02\)00131-0](http://dx.doi.org/10.1016/S0966-9795(02)00131-0).
- [39] J.-J. Kim, Y. Choi, S. Suresh, A.S. Argon, Nanocrystallization during nanoindentation of a bulk amorphous metal alloy at room temperature, *Science* 295 (2002) 654–657, <http://dx.doi.org/10.1126/science.1067453>.
- [40] Z. Yan, K. Song, Y. Hu, F. Dai, Z. Chu, J. Eckert, Localized crystallization in shear bands of a metallic glass, *Sci. Rep.* 6 (2016) 19358, <http://dx.doi.org/10.1038/srep19358>.
- [41] W.H. Jiang, M. Atzmon, Mechanical strength of nanocrystalline/amorphous Al90Fe5Gd5 composites produced by rolling, *Appl. Phys. Lett.* 86 (2005) 151916, <http://dx.doi.org/10.1063/1.1897434>.
- [42] H. Chen, Y. He, G.J. Shiflet, S.J. Poon, Deformation-induced nanocrystallization in shear bands of amorphous alloys, *Nature* 367 (1994) 541–543, <http://dx.doi.org/10.1038/367541a0>.
- [43] E.S. Park, Understanding of the shear bands in amorphous metals, *Appl. Microsc.* 45 (2015) 63–73, <http://dx.doi.org/10.9729/AM.2015.45.2.63>.
- [44] J.J. Lewandowski, A.L. Greer, Temperature rise at shear bands in metallic glasses, *Nat. Mater.* 5 (2006) 15–18, <http://dx.doi.org/10.1038/nmat1536>.

CHAPTER 4: EXPLORING THE USE OF CHEMISTRY MODIFICATIONS AND ELECTRON BEAM MELTING TO REDUCE MICRO-CRACKING DURING ADDITIVE MANUFACTURING OF METALLIC GLASS

Introduction

The glass-forming chemistry processed in chapter 3, FeCrMoCB, was selected due to its commercial availability in the form of AM-quality powder. After process development, it was determined that the alloy was not well suited for AM processing due to its tendency to crack regardless of process development. Micro-cracking was unavoidable during LPBF of FeCrMoCB due to the brittleness of the composition and the large thermal stresses in LPBF. This chapter explores the use of chemistry modifications and EBM to improve alloy plasticity and reduce thermal stress, respectively.

Glass-forming alloys with a higher plasticity than FeCrMoCB may exhibit a higher AM processability and develop less micro-cracks during AM. Two new glass-forming chemistries were processed in this work, both are predicted to have a higher plasticity and crack resistance than FeCrMoCB. The first glass-forming chemistry is a modification of the FeCrMoCB alloy without chromium, $\text{Fe}_{68.20}\text{Mo}_{25.62}\text{C}_{3.37}\text{B}_{1.75}$ at. %. Decreasing the chromium content in the FeCrMoCB family of alloys was documented to improve plasticity (Gu et al., 2008) and GFA (Pang et al., 2002). Therefore, the elimination of chromium from FeCrMoCB is expected to improve the alloy's suitability for LPBF without the requirement to re-start parameter development. The second glass-forming chemistry is $\text{Zr}_{\text{balance}}\text{Cu}_{23-25}\text{Al}_{3-5}\text{Nb}_{1-3}$ wt. % (hereafter referred to as AMZ4), an alloy patented by Heraeus (Hanau, Germany) having a T_m , T_g , and T_x of 915°C, 400°C, and 470°C, respectively. AMZ4 is advertised as a metal powder for AM, however there is no evidence that the chemistry was specifically designed for AM. Instead, the powder size, morphology and purity of the

powder are of AM quality. Zirconium-based metallic glass alloys are well-known to have higher plasticity than Fe-based metallic glass alloys, so the drastic change in alloy chemistry is expected to allow for crack-free fabrication of metallic glass. Unfortunately, AMZ4 will require a significant amount of parameter development since the alloy has not previously been additively manufactured. It is hypothesized that FeMoCB and AMZ4 will have higher plasticity and crack resistance than FeCrMoCB, and therefore exhibit a higher processability during LPBF.

In addition to LPBF processing, FeMoCB and FeCrMoCB will be processed using EBM. During EBM, the build platform is heated to temperatures $>100^{\circ}\text{C}$ during the processing of conventional metals. The high temperature of the build platform reduces the thermal gradient between the melt and the previously melted layers, so the thermal stress is reduced. The reduction in stress may allow for the fabrication of crack-free FeCrMoCB, which was unattainable under the high thermal stress conditions of LPBF. In addition, the predicted improvement in plasticity and the reduced thermal stress in EBM may allow for crack-free fabrication of FeMoCB. Finally, since EBM is performed under vacuum, the glass-forming alloys are less likely to oxidize during processing. This is useful for attaining an amorphous microstructure since the GFA of metallic glass is sensitive to changes in chemical composition.

Materials and Methods

Powder characterization

All powder batches were produced via gas atomization. The AMZ4 powder was gas provided by Heraeus and was used as-received. The FeCrMoCB EBM powder was sieved to $+200/-120$ ($+74\ \mu\text{m} / -125\ \mu\text{m}$) before use. The FeMoCB powder batches were produced at

Swerea KIMAB (Kista, Sweden) with particle size distributions for LPBF and EBM. The FeMoCB LPBF powder was air classified and the EBM powder was sieved to +325/-140 (+44 μm / -106 μm) before AM. Particle size distributions of the four powder batches (FeCrMoCB for EBM, FeMoCB for EBM, FeMoCB for LPBF, and AMZ4 for LPBF) were measured using a Microtrac S3500 laser diffraction particle size analyzer, and particle morphologies were examined using a JEOL 6010 LA SEM.

Laser Powder Bed Fusion

The FeMoCB and AMZ4 glass-forming alloys were processed in an EOS M280 system equipped with a 200 W Yb-fiber laser. During processing, the build chamber was flooded with argon gas to limit the oxygen content in the chamber (< 1000 ppm). The build substrates consisted of ground inserts (15.24 cm x 1.90 cm x 0.63 cm) bolted into matching pockets milled into a standard EOS steel build platform. This setup facilitated rapid sample removal and reduced build set-up time. Processing parameters were developed for FeMoCB and AMZ4 in an attempt to produce crack-free (fully-dense), amorphous components. Another goal of parameter development was to observe the influence of the new alloy chemistries on crack resistance during LPBF.

Since a processing space was optimized for FeCrMoCB in chapter 3, this was used as a starting point for development of FeMoCB. Cylindrical samples 1 cm in diameter and of varying height were produced onto 4140 steel inserts during parameter development. Laser parameters including laser power, laser scanning speed and hatch spacing were systematically varied as described in the *Materials and methods* section of chapter 3. Processing parameters for AMZ4 were similarly varied. The AMZ4 alloy was built onto

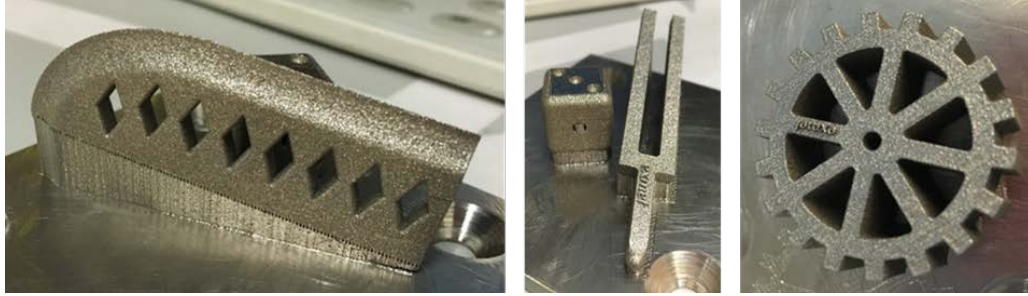


Figure 2. Photos depicting LPBF-fabricated AMZ4.

stainless-steel build substrates. The optimized parameter set for AMZ4 was used to produce a 30 mm x 45 Ø mm cylinder and several components with unique geometries depicted in Figure 2. The density of the FeMoCB and AMZ4 components was analyzed using the Archimedes' method. In addition, the components were sectioned along the z-plane and analyzed using a Rigaku SmartLab x-ray diffractometer and a Hirox KH-7700 digital light microscope.

Electron Beam Melting

The FeCrMoCB and FeMoCB glass-forming alloys were processed in an Arcam A2 EBM system and an Arcam S12 EBM system, respectively. From a process development standpoint the main difference between LPBF and EBM is the number of parameters that can be altered and eventually optimized. In this work, the number of parameters was reduced for the initial development work to find an appropriate processing window, and the EBM machine was run in manual mode. Due to the complexity of the EBM system, using constant processing parameters (i.e. manual mode) can only be used for very simple geometries, like the small-scale cylinders produced during parameter development. For more complex geometries the processing parameters, like energy input, are calculated for each layer using the machine's internal algorithms.

Production in a stock EBM machine requires more than 10 liters of powder even for the fabrication of small components. This is a result of the powder feeder design in commercially available EBM equipment. Due to the high cost of EBM quality powder, producing large powder batches for new alloy development is impractical. A newly designed and constructed build tank, pictured in Figure 3, was produced at NCSU to process new materials. The small build tank requires less than 1 liter of powder for operation and enhances the vacuum capability of the EBM by an order of magnitude. During EBM development, the FeCrMoCB and FeMoCB alloys were processed in Arcam EBM systems equipped with a custom small build tank.

Twenty EBM builds were ran during FeCrMoCB parameter development. Three different build geometries were fabricated onto 50.8 mm x 76.2 Ø mm stainless steel build platforms: 1. 10 Ø mm 2. 15 Ø mm 3. 20 mm x 20 mm. The build height was dictated by the amount of powder and success of the build parameters. The build height reached 2 mm during some EBM trials. Initially cylindrical geometries were used because the sharp corners of a rectangular prism can initiate cracking. After several EBM trials, it was determined that



Figure 3. Photo depicting the redesigned EBM build tank for processing small powder batches.

the small diameter cylinders (10 Ø mm) did not allow adequate time for the development of a stable melt pool, so the diameter was increased to 15 Ø mm. After further development, the part geometry was changed to a rectangular prism shape (20 mm x 20 mm) with the intent of having an equal melt pool length during each line of melting. Due to the complexity of EBM processing, the use of different parameters and process development strategies is less intuitive than for LPBF. The key parameters focused on during process development in this work are preheat temperature, current, voltage, beam speed and focus offset. A variety of melt strategies, some less common than others, were employed in an attempt to produce metallic glass components:

1. Plate preheat: the build plate was preheated up to 450°C. Plate preheat reduces thermal stress since the thermal gradient between the melt and previously melted layers is reduced.
2. No build plate preheat: the build plate was not heated in an attempt to eliminate overheating.
3. Powder preheat: the powder was preheated to sinter the powder together before melting. This reduces powder smoking and the thermal gradient.
4. No powder preheat: the powder was not preheated since the build stabilizes at the preheat temperature which is $> T_g$.
5. Constant energy per layer: energy input per layer was held constant, but processing parameters were altered.
6. Constant melt pool size: melt pool size was held constant while processing parameters were altered. Melt pool size was calculated using Equation 2.

Equation 2. The EBM melt pool size where P is power (W), θ_m is the temperature rise to T_m ($^{\circ}\text{C}$), k is the thermal conductivity ($\text{W}/\text{mm}^{\circ}\text{C}$), d is the beam diameter (mm), v is velocity (mm/s), ρ is the density of the powder (g/mm^3) and c is specific heat ($\text{J}/\text{g}^{\circ}\text{C}$).

$$z = 0.1 \frac{P}{\theta_m \sqrt{Kdv\rho c}}$$

7. Layer remelt: each layer was melted with low current and high focus offset to reduce powder smoking, and was remelted 2-10 times to ensure full melting.
8. Flash melt: high scanning speed was used in an attempt to melt powder before smoking could occur.

Selected samples were analyzed using XRD.

The EBM parameter development of FeMoCB was significantly different from EBM parameter development of FeCrMoCB. The same 50.8 mm x 76.2 \varnothing mm stainless steel build platforms were used; however, process development mainly consisted of a smoke test melt strategy. During the smoke test, energy input was slowly increased from 0 J using a variety of different processing parameters in an attempt to find a parameter space that did not cause smoking.

Results

Powder Characterization

The particle size distribution for each of the four powder batches is reported in Table 2 and Figure 4 - Figure 7. The 10th and 90th percentiles of the FeMoCB LPBF powder after air classification are 19 and 50 μm by volume, and 8 and 32 μm by number. Since the FeMoCB LPBF powder was air classified, a distinct cut off in the powder size by number is visible around 9 μm in Figure 6. The particle morphologies were mostly spherical with a low

concentration of elongated particles. This powder spread well during LPBF and has acceptable morphology for LPBF.

The 10th and 90th percentiles of the as-received AMZ4 powder are 10 and 34 μm by volume, and 2 and 16 μm by number. The particle size distribution curve in Figure 4 reveals that a large number of fine-sized ($< 10 \mu\text{m}$) particles exist in the powder batch. These fine particles are lost in the powder size distribution curve by volume which exhibits a Gaussian distribution. The large number of fine particles in the AMZ4 powder batch could not be removed via sieving and resulted in poor spreadability onto the build platform during LPBF. In addition to fine-sized particles, the AMZ4 powder batch contained some non-spherical particles, elongated and donut shaped particles; some of these particle geometries are depicted in Figure 9.

The 10th and 90th percentiles of the FeCrMoCB EBM powder after sieving are 59 and 120 μm by volume, and 17 and 88 μm by number. A micrograph of the powder batch in Figure 9 indicates that the FeCrMoCB particles are mostly spherical. Although there are some fine particles, the FeCrMoCB powder batch has an acceptable size and morphology for EBM processing.

Table 2. Particle size distribution and morphology of four powder batches processed using LPBF and EBM.

Alloy	AM Machine	Particle Size Volume	Particle Size Number	Particle Morphology
FeMoCB	LPBF	19 - 50 μm	8 – 32 μm	Non-spherical
AMZ4	LPBF	10 - 34 μm	2 - 16 μm	Mostly spherical
FeCrMoCB	EBM	59 - 120 μm	17 - 88 μm	Spherical
FeMoCB	EBM	60 - 175 μm	16 - 96 μm	Non-spherical

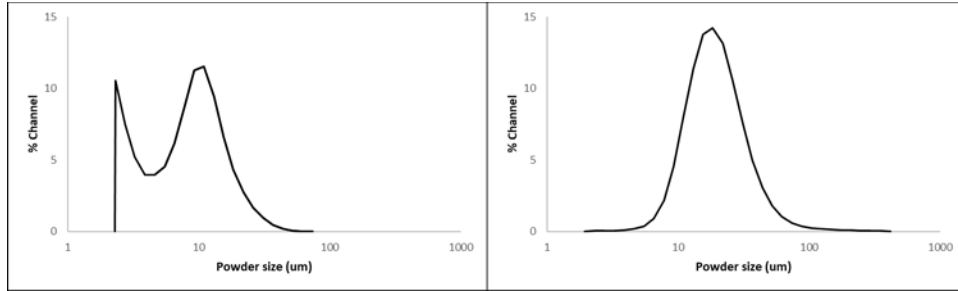


Figure 4. Particle size distribution by number (left) and volume (right) of AMZ4 LPBF powder.

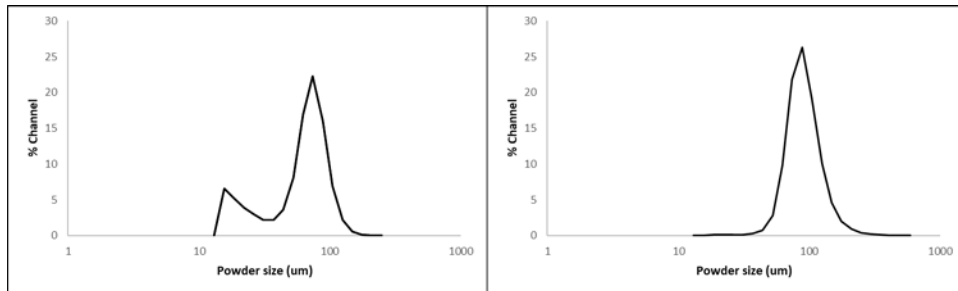


Figure 5. Particle size distribution by number (left) and volume (right) of FeCrMoCB EBM powder.

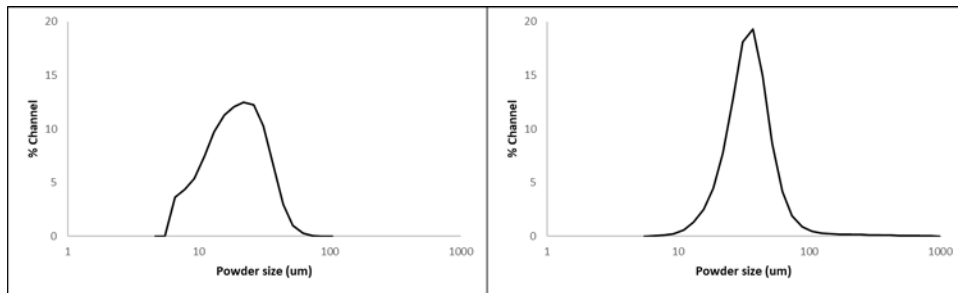


Figure 6. Particle size distribution by number (left) and volume (right) of FeMoCB LPBF powder.

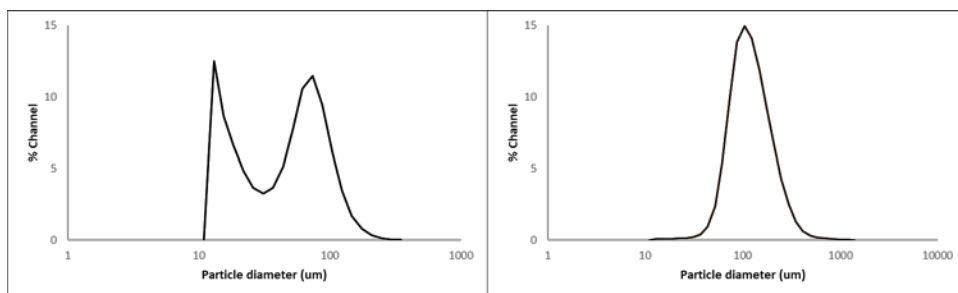


Figure 7. Particle size distribution by number (left) and volume (right) of FeMoCB EBM powder.

The 10th and 90th percentiles of the FeMoCB EBM powder after sieving are 60 and 175 μm by volume, and 16 and 96 μm by number. The particle size distribution by number is bimodal with 25% of the particles having a diameter less than 30 μm . Similarly to the AMZ4 powder, these fine particles are lost in the powder size distribution curve by volume which exhibits a Gaussian distribution. Scanning electron microscopy in Figure 8 reveals that a large concentration of elongated and plate-like powder particles remained in the powder batch after sieving EBM FeCrMoCB. The large number of smaller-sized particles and the non-spherical morphologies are not ideal for EBM. The small particles increase the chances of smoking while the non-spherical morphologies cause inefficient powder bed packing that can cause smoking or limit the maximum achievable density.

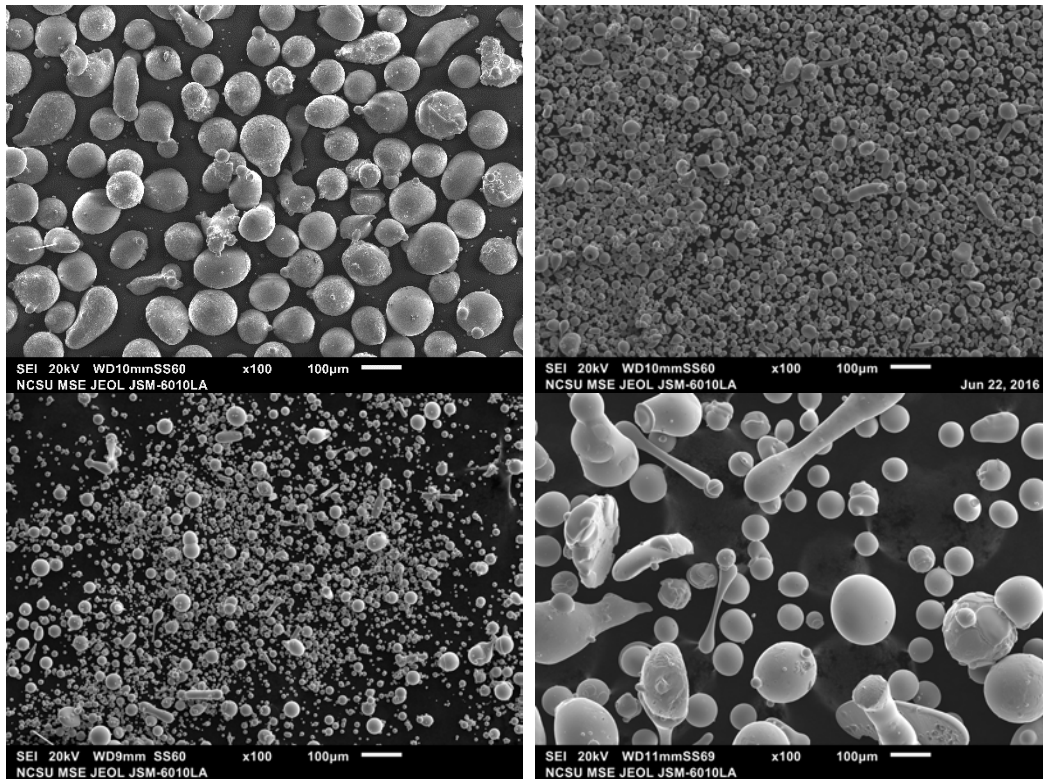


Figure 8. SEM micrographs of the EBM FeCrMoCB (top-left), LPBF AMZ4 (top-right), LPBF FeMoCB (bottom-left) and EBM FeMoCB (bottom-right) gas atomized powders.

Laser Powder Bed Fusion

The FeMoCB components fabricated using LPBF have a much denser cross-section compared to the the FeCrMoCB components shown in chapter 3 (Figure 9). Like the chapter 3 FeCrMoCB components, the FeMoCB components were XRD amorphous along the build direction. The microhardness of the FeMoCB samples averaged at 993 HV and were higher than those measured for the chapter 3 FeCrMoCB components, 902 HV.

The AMZ4 components fabricated using LPBF contained spherical porosities roughly 10-30 μm in diameter (Figure 10). The average Archimedes' density (in acetone) of the solid samples was 98.6% as compared to a cast reference sample. The high density of the samples suggests that full melting occurred during LPBF. The remaining porosity is likely a result of gas atomization porosity, the powder donut feature, or poor powder bed density.

Due to the poor weldability between zirconium and steel, there was only a superficial connection between the AMZ4 component and the steel build insert. AMZ4 parts would routinely delaminate from the build substrate and curl up at the edges due to the thermal stress accumulation during LPBF processing. Samples were often knocked off the build platform by the recoater blade and could easily be removed from the plate by hand. To improve the weld quality between AMZ4 and the build substrate, two new build plate materials were tested: brass and titanium. Zirconium has the best weldability to titanium; therefore, the build plate material was changed and laser parameters were further developed. Sample connectivity greatly improved but curling around the edges of larger parts still occurred. The high plasticity of AMZ4 as compared to Fe-based alloys allowed for the production of crack-free components. However, when larger-scale samples were produced, large cracks initiated at the edges or base of the AMZ4 component (Figure 11). These cracks

were distinctly different from the network of micro-cracks observed in the FeCrMoCB and FeMoCB alloys. The shape of the cracks in AMZ4 imply that they were caused by thermal stress. X-ray diffraction analysis along the build plane of AMZ4 samples is reported in Figure 12 and shows a broad amorphous halo peak superimposed over some sharp reflections.

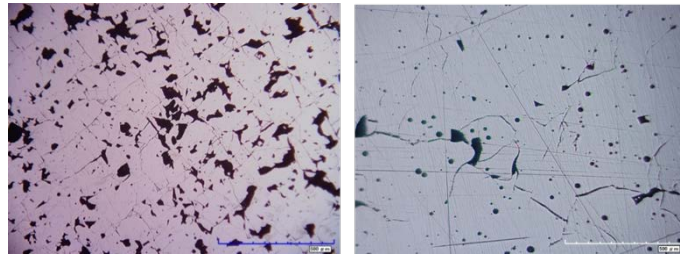


Figure 9. LPBF-fabricated FeCrMoCB (left) and FeMoCB (right) cross-sections along the build axis.

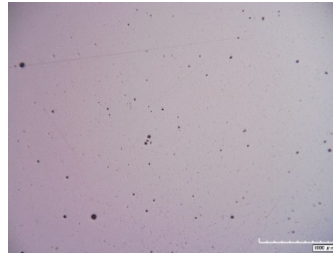


Figure 10. Cross section along the build plane of LPBF-fabricated AMZ4 revealing spherical porosity between 10 and 30 μm in diameter.

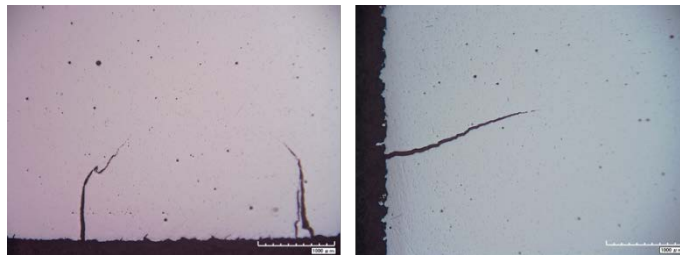


Figure 11. Micrographs of LPBF-fabricated AMZ4 along the build axis depicting stress-induced cracks.

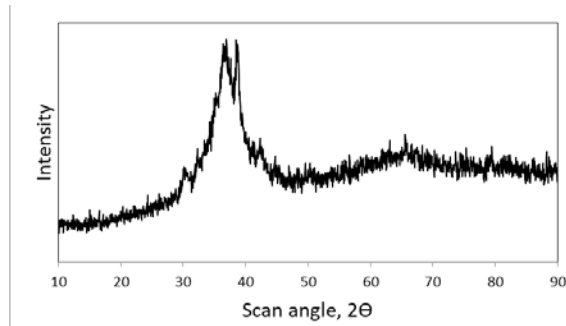


Figure 12. X-ray diffraction spectrum of LPBF-fabricated AMZ4.

Electron Beam Melting

Selected FeCrMoCB EBM builds are pictured in Figure 13. Samples produced during parameter development show evidence of cracking, poor density and overheating. During EBM fabrication, the build plate temperature often increased to above the T_g and T_x after a few layers were deposited. After visual inspection during and after EBM fabrication, these samples were deemed unworthy of further characterization. A “best case scenario” sample in terms of microstructure was built onto a 4 inch thick build plate. The larger build plate was used to act as a heat sink to keep the component temperature below the T_g of FeCrMoCB. The first 10 layers were doubled melted to ensure good connectivity to the build platform. The sample reached 2.45 mm tall and the final build plate temperature was 57°C, far below the T_g . The XRD spectrum, shown in Figure 14, indicates that the sample was fully crystalline. The build plate thermocouple, located on the underside of the build plate, is the only temperature reading offered by the EBM equipment. Although build plate temperature was maintained below T_g , there is no information on the surface temperature of the build plate or FeCrMoCB sample during EBM fabrication; this is a major flaw of the stock EBM and “small build tank” design.

During EBM processing, FeMoCB was prone to severe smoking even with low beam voltage and current values, and a highly defocused beam. A series of low voltage, low speed and large focus offset parameters were used to test the smoking threshold of the powder. In almost all parameter combinations, the powder smoke threshold was non-existent. In several instances the powder spread onto the plate would smoke before the electron beam interacted with the powder. The small amount of leakage current was enough to cause smoking of the powder bed. Unlike FeCrMoCB, the FeMoCB powder batch was not processable using EBM and no components were produced.

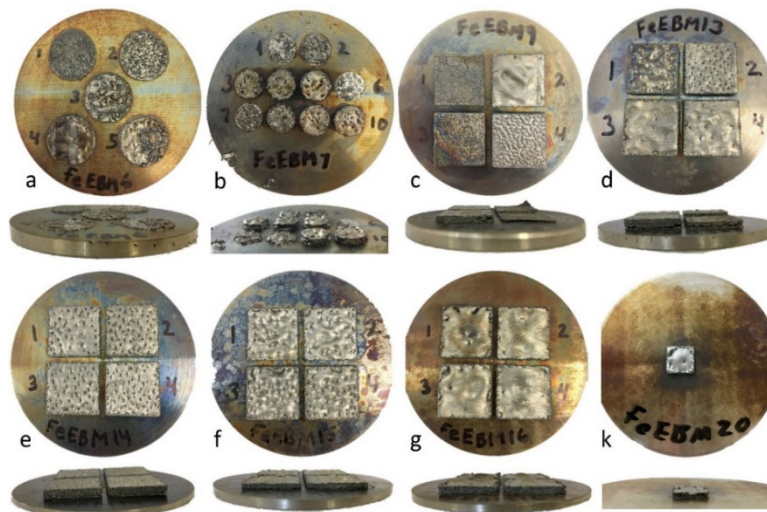


Figure 13. Selected EBM builds of FeCrMoCB.

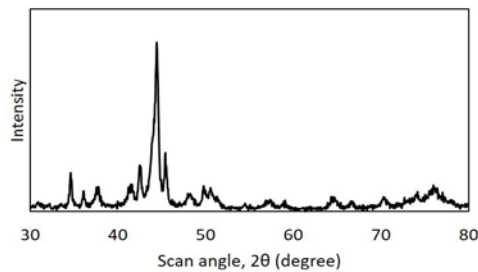


Figure 14. X-ray diffraction spectrum of the “best case scenario” EBM-fabricated FeCrMoCB sample.

Discussion

Powder

Most of the powder batches contained elongated powder particles. Non-spherical powder morphologies negatively influence the powder bed density and subsequently impact the maximum achievable solid density. The occurrence of elongated particles is a result of the high liquid viscosity of glass-forming alloys and the lack of fully-optimized gas atomization parameters. Gas atomization parameter optimization for a custom alloy, especially one with a high viscosity, can be costly and time consuming.

The AMZ4 powder batch contained a large number of fine-sized particles. As powder size decreases, the surface area to volume ratio increases and the powder agglomerates and picks up water. The AMZ4 powder was challenging to spread during LPBF, so the first layers were manually spread until the powder bed stabilized. Similarly, the EBM powder batches both contained a large number of smaller sized particles. During EBM, these small particles negatively affect processability in terms of powder smoking; this is discussed further in the *Electron Beam Melting* section below.

Laser Powder Bed Fusion

The absence of chromium in FeMoCB was intended to increase the plasticity of the alloy to reduce micro-cracking during LPBF. The effect of increased plasticity was significant enough to noticeably reduce cracking during LPBF and during post-processing; however, some microcracks were still present in the cut and polished material. Poor connectivity between the cylinders and the build plate was a key challenge during AMZ4 processing. In AM processing of Zr-based BMGs several researchers used build substrates with an identical chemistry as the BMG or used pure Zr substrates. The cost of attaining

metallic glass or pure Zr substrates was outside of the budget of the AMZ4 development project. The thermal stress caused by rapid heating and solidification caused delamination from the build platform, geometric distortion and cracking in LPBF-fabricated AMZ4. Additionally, cracking and delamination from the build plate likely reduced heat transfer during melting; this is a possible cause of the partial crystallization. Further parameter development, likely focused on scanning pattern optimization, is required to help reduce stress accumulation. Lastly, Zr-based BMGs are highly reactive with oxygen. With the small powder size distribution it is possible that the virgin powder contained > 2500 ppm (wt. %) of oxygen as specified in the material datasheet. Low oxygen content is well known to cause crystallization in Zr-based BMGs using any processing techniques (Liu et al., 2002; Pauly et al., 2017; Y. Zhang et al., 2015). It is challenging to eliminate oxidation during LPBF processing. The build chamber in the EOS M280 is flooded with argon during processing, but residual oxygen is still present during operation. Highly reactive metals, like Zr, pick up this oxygen during melting. Although no oxygen analysis was completed on the AMZ4 powder or solid, it is a probable catalyst of grain nucleation.

Electron Beam Melting

Three major challenges were encountered during EBM parameter development: powder smoking, overheating and cracking; they are each discussed in detail in this section. During electron beam interaction, powder particles become electrostatically charged and repel one another if the charge is not dissipated quickly. If the repulsive forces overcome the force of gravity then the powder particles electrostatically repel and form a smoke cloud of metal powder. Instances of powder smoking were frequently observed throughout EBM process development of FeCrMoCB and FeMoCB. Non-ideal powder size, morphology and

chemistry are chief contributors to smoking. Electron beam parameters with low scanning speed, low current and large focus offset significantly reduced the occurrence of smoking during EBM.

The low electrical conductivity of Fe-based BMGs was an additional cause of smoking. Electron beam melting of low electrical conductivity materials is achieved by preheating the powder bed with the electron beam before melting each layer. This preheating step sinters the powder, and the binding forces between the sintered particles reduce the probability of smoking. Preheating parameters were applied to FeCrMoCB during EBM processing, however atomic diffusion never took place and the powder did not sinter. The EBM build temperature typically stabilizes at the sintering temperature ($> 0.5T_m$). Although powder bed preheating reduces smoking during the production of low conductivity crystalline metals, it is not feasible to preheat the metallic glass powder since the sintering temperature is greater than the T_g . If the build temperature is held at $T > T_g$ then the material would crystallize without adequate control over time-at-temperature.

Powder smoking negatively affected productivity during EBM parameter development. After a smoke event, all of the powder on the build plate is gone and the electron beam automatically turns off. After this, powder is manually spread onto the build platform. Depending on the height of the build at the time of smoke and how many smoke events happened during the build, a lot of powder from the feeder is wasted. Electron beam melt builds of FeCrMoCB were often run until the powder dispenser was empty. Before starting a new EBM build, the electron gun needs to be disassembled and cleaned since powder is often accelerated up into the gun during a smoke event. In addition to this explosive smoking, local smoke events also occurred during parameter development. During

local smoking the beam pushes powder away from the melt pool instead of melting it (powder only moves 1-2 mm). In this case the beam does not shut off and the operator must pause the build and make manual adjustments to the build platform height. If this build plate adjustment is not completed, the next layer will be too thick, and powder smoking will become more likely or the powder layer will not be fully melted. Overall, high counts of fine particles in the FeCrMoCB powder batches, coupled with the poor electrical conductivity of the Fe-based BMG powder caused smoking.

It was initially hypothesized that the absence of chromium in FeMoCB caused an oxide layer to form on the surface of powder particles, thereby preventing charge dissipation. Cross-sectional analysis using energy dispersive spectroscopy did not provide enough resolution to detect an oxide layer on the FeMoCB powder surface; therefore, oxygen content was measured using inert gas fusion analysis. Oxygen content was only 0.020 at. % measured in the powder EBM FeMoCB powder compared to 0.098 at. % in the EBM FeCrMoCB powder; this suggests that significant oxide formation was not the cause of excessive smoking. Alternatively, it is predicted that smoking of FeMoCB was primarily a result of powder morphology effects. Scanning electron microscopy analysis revealed that the EBM FeMoCB powder batch contained a high volume of elongated and non-spherical particles that could not be removed via sieving. The non-spherical powder morphology resulted in inefficient powder packing in the EBM machine, therefore the area of contact between particles was reduced and charge was dissipated less efficiently. Challenges associated with gas atomization of custom alloys, especially a very viscous metallic glass alloy, make optimizing powder morphology challenging. A combination of fine particles,

non-spherical powder morphology and poor electrical conductivity of the material caused severe smoking that prohibited the production of FeMoCB parts using EBM.

In addition to smoking, heat build-up was a major challenge encountered during EBM processing. Samples were produced with a variety of build plate temperatures below T_g . Higher build plate temperatures helped reduce severe cracking, but micro-cracking occurred regardless of build plate temperature due to the brittle nature of FeCrMoCB. During solidification, heat dissipates into the build plate. Once the heat capacity of the build plate is reached, the build plate temperature drastically increases as more layers are melted. In one instance, the build plate temperature increased by 600°C during EBM, exceeding the T_g and T_x , after only 2 mm of material was deposited. The build plate temperature increased drastically because the build plate is surrounded by powder. The low thermal conductivity metallic glass powder effectively isolates the build plate from the build tank and resulted in quick heat buildup during melting. To improve the heat capacity of the build plate and reduce overheating, a larger build plate, 101.6 mm x 76.2 \AA mm, was used; this minimally improved overheating. Overheating of the build plate and FeCrMoCB parts resulted in part curling, swelling, beading and crystallization.

By eliminating the build plate preheat and melting only a small cross sectional area, a 3 mm tall sample was produced while maintaining build plate temperature $< 0.5T_g$.

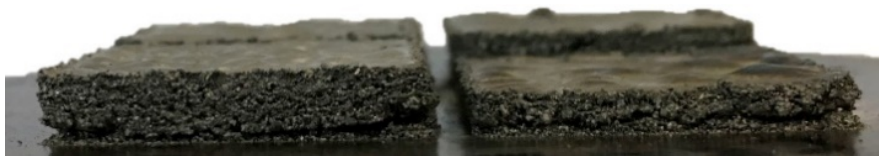


Figure 15. FeCrMoCB EBM samples depicting delamination from the build plate and cracking along the XY plane.

Regardless of build plate temperature, XRD results of the EBM sample indicated that the material was fully crystallized. Since EBM is performed under vacuum, it is critical that heat transfers through the deposited material and into the build plate to allow for rapid solidification. Crystallization occurred, even when the build plate temperature remained low, due to severe cracking along the XY plane. Cracking reduced contact to the build plate and then heat built up occurred in the part rather than the build plate.

Catastrophic cracks were often generated along the XY plane during EBM processing (Figure 15). Cracking is likely a cause of the brittle nature of the FeCrMoCB alloy and thermal stresses generated during processing. Thermal stresses arise due to the temperature difference between melted and unmelted layers of material. Elevated build plate temperatures and powder preheat help relieve stress and reduce cracking in EBM. In this work, samples were produced with a variety of build plate temperatures below T_g . Higher build plate temperatures helped reduce severe cracking; however, plate temperature quickly increased to temperatures above T_g and T_x and crystallization took place. In addition, powder preheat was used in some instances; however, it was eliminated for most EBM runs to try to avoid overheating. Cracking caused heat to accumulate into the FeCrMoCB part rather than be transferred into the build plate. Elevated build temperatures reduced catastrophic cracking, but micro-cracking occurred regardless of build plate temperature due to the brittle nature of FeCrMoCB.

Chapter Summary

The objective of chapter 4 research was to explore the use of alloy chemistry modifications and EBM to reduce micro-cracking during AM of metallic glass alloys. The FeMoCB alloy, which was a variation of the alloy processed in chapter 3, exhibited a

noticeable improvement in LPBF processability. However, the alloy still contained micro-cracks after cutting and polishing. Dissimilarly, the AMZ4 alloy demonstrated a much higher resistance to cracking during LPBF. The improved processability, a result of the increased plasticity, allowed for the production of mostly amorphous components with complex geometries.

An amorphous metallic glass was not manufactured using EBM, however its utility to produce metallic glass is still feasible. Devitrification of FeCrMoCB during EBM was caused by insufficient heat dissipation into the build plate, a result of cracking and overheating of the build plate. It is well understood that an elevated build plate temperature relieves thermal stresses in AM. An active thermal management system would provide the capability to use elevated build plate temperatures, relieving stress and eliminating cracking, while maintaining the build temperature below T_g . Furthermore, the inability to fabricate any components using the FeMoCB alloy highlighted the impact of powder morphology on the processability of alloys in EBM. In the future, new alloy chemistries may require multiple iterations of gas atomization before a batch with powder size and morphology that is acceptable for EBM is produced.

This work highlighted the importance of the alloy chemistry and manufacturing method during AM of metallic glass. The use of "educated-guess" alloy chemistry selection was employed in an attempt to find one suitable for bulk glass formation using AM. Instead, a more scientific alloy chemistry selection methodology should be applied.

CHAPTER 5: IDENTIFICATION AND APPLICATION OF COMPUTATIONAL TOOLS TO PROPOSE A NOVEL IRON-BASED METALLIC GLASS CHEMISTRY WITH ACCEPTABLE ADDITIVE MANUFACTURING PROCESSABILITY

Introduction

Thus far, research regarding AM of Fe-based metallic glass has fixated on process development. While the technology has progressed, researchers continue to report challenges overcoming devitrification and cracking during processing; both are detrimental to the mechanical and magnetic performance of the material. Based on the literature surveyed in chapter 2, no group has targeted a glass-forming chemistry based on AM process requirements. Instead, chemistries were chosen based on familiarity from other processing techniques such as casting or melt spinning. Consequently, the alloy compositions used thus far exhibited poor AM processability, evident by their propensity to crack regardless of process development efforts. These results indicate that there is a need to identify the causes of crack formation during AM of glass-forming alloys and ultimately find compositions with higher crack resistance and better AM processability than the ones previously selected.

The work completed in chapter 4 revealed that AM can be used to produce crack-free metallic glass using a less brittle, Zr-based alloy. In addition, the chapter 4 work showed that altering the composition of FeMoCrCB did influence the AM processability of the alloy. The selection of new compositions in chapter 4 resembled a trial-and-error and guesswork approach to metallic glass alloy design. Alternatively, the objective of this chapter is to apply a quantitative, scientific approach towards alloy design to propose a unique Fe-based composition with high AM processability. Fe-based metallic glass alloys are of particular interest due to their soft magnetic properties, high strength and low cost compared to Zr-based metallic glass (Telford, 2004). To attain a high AM processability, the unique Fe-

based composition must have suitable properties for additive processing including the ability to be atomized into high-quality powder with the intended chemical, morphological and flow properties. In addition, it is imperative that the composition possess a high crack resistance and sufficient GFA and thermal stability to avoid devitrification and cracking during laser melting. The methodologies and results presented in this chapter are based on work performed during an internship at QuesTek Innovations LLC, located in Evanston, IL. In addition, some technical work was supported by engineers at QuesTek Europe AB, located in Stockholm, Sweden.

Understanding the causes of cracks in AM is an essential step towards improving the crack resistance of an AM material. Cracks present in AM metals are primarily a result of lack of fusion, delamination, solidification cracking, strain age cracking, liquation cracking or ductility dip cracking. With the exception of lack of fusion and delamination, these crack types are all distinct to crystalline materials, and therefore are not implicitly relatable to cracks found in amorphous metallic glass. However, knowledge of the origin or remedy to the different AM cracks gives insight into designing a metallic glass to have acceptable crack resistance during AM. The lack of fusion and delamination cracks result from imperfect processing conditions, and therefore can typically be eliminated through process parameter alteration. Strain age cracking in conventional metals is relatable to the relaxation induced brittleness, and the subsequent cracking that can occur during reheating of metallic glass above the glass transition temperature. Again, this can be managed via process parameter alteration. Solidification cracking occurs in AM while the material is in between the solid and liquid phases. This means that the size of the supercooled liquid region, $\Delta T = T_l - T_g$, in a

glass-forming alloy impacts the likelihood of a solidification style crack to occur during AM, and that this region should be minimized to improve an alloy's solidification crack resistance.

Cracks characterized as liquation or ductility dip cracks form exclusively under an applied or residual stress. The residual stress inherent to AM that causes these cracks to form can be managed through processing parameter and scanning pattern alteration, however, it cannot be eliminated completely. The stress generated during AM is a result of the steep temperature gradient around the molten pools and the subsequent expansion and contraction of the material (Li et al., 2014a). Only when this thermal stress exceeds the fracture strength of a material will a crack occur (Xing et al., 2018). According to FEM simulations by Xing et al., even the maximum thermal stress generated during rapid heating/solidification does not exceed the typical fracture strength of Fe-based metallic glass. For this reason, Xing et al. assert that AM thermal stress cannot cause micro-cracks unless there are stress concentrating defects in the AM material (i.e. porosity). Pores are an intrinsic defect in AM components even with optimized processing parameters. It seems appropriate to assume that a material with a lower coefficient of thermal expansion will generate less stress during AM, and that a material with a higher fracture strength will have a higher AM crack resistance. For this reason, it is useful to predict and optimize the thermal expansion coefficient and fracture strength of a new AM material to improve liquation and ductility dip crack resistance.

Standard rules used to guide the selection of glass-forming compositions, originally published by renowned metallic glass researchers (Cahn and Greer, 1996; Inoue, 2000; Turnbull, 1969), were described in the *Glass-forming Compositions* section. While the glass-formation rules offered by Cahn, Greer, Turnbull, and Inoue have successfully guided the

development of new glass-forming compositions, they in no way capture the true complexity of glass formation. Li et al. applied the glass-formation rules conceived by Cahn, Greer, Turnbull, and Inoue, to approximate the number of potential glass-forming alloy systems (binary, ternary, quaternary and quinary) (Yanglin Li et al., 2017). Approximately 10^6 compositions satisfied the basic glass-formation rules. Of these 10^6 potential BMGs Li et al. calculated that only a small fraction, $\sim 0.1\%$, have actually been discovered. This low fraction originates from the lack of predictable theories to identify glass-forming compositions and the inefficiency of the currently used trial-and-error alloy development methods.

Several glass-formation design theories have been proposed following the first rules offered by Cahn, Greer, Turnbull, and Inoue (Laws et al., 2015; Perim et al., 2016; Vincent et al., 2011; Yang and Zhang, 2012; K. Zhang et al., 2015). Li et al. divided all glass-formation design theories into two groups (Yanglin Li et al., 2017). The first group is comprised of theories that are based on properties that are determined by the physical properties of the alloy such as viscosity, fragility, density, T_l , T_g , T_x , and the structure and density of states of competing crystalline phases. These physical properties can be combined to create parameters that correlate with glass formation; some are listed in Table 3. The challenge with using theories in this group is that many of the physical properties needed to determine

Table 3. Parameters that correlate with GFA (Yanglin Li et al., 2017).

Parameter	Equation
Reduced glass transition, T_{rg}	T_g/T_l
Supercooled liquid region ΔT	$T_x - T_g$
Parameter S	$(T_x - T_g)/(T_l - T_g)$
Parameter γ	$T_x/(T_l + T_g)$

GFA, like T_i , T_x , and T_g , are only available after successful production of the metallic glass (Brennhaugen et al., 2017; Yanglin Li et al., 2017). Therefore, they do not aid in the discovery of new metallic glass alloys without time and resource-consuming trial-and-error testing. However, knowledge of the competing crystalline phases does provide useful input for alloy design. For example, topologically close packed (TCP) phases have non-directional bonding and a high coordination number close to that of the clusters found in the supercooled liquid, so they nucleate easily from the supercooled melt and hinder glass formation (Belyakova and Slovokhotov, 2003; Schmid, 1988; Wang et al., 2009). Additions of C or B suppress the formation of TCP phases in Fe (Han et al., 2017) and are therefore found in most high glass-forming Fe-based compositions (Guo et al., 2014).

The second group includes theories that rely on the interdependence of quantities including the atomic size of the constituent elements, heat of mixing, and electronegativity (Inoue, 2000; K. Zhang et al., 2015). Both groups of theories present simple, one-dimensional approaches towards glass-formation that still do not capture the complexity of metallic glass formation. Despite their limited use to actually predict glass formation, these two groups of theories provide the framework for current metallic glass alloy development (Perim et al., 2016).

Utilizing many glass-formation theories and reported observations of melt spun metallic glass, Ren et al. developed a machine learning (ML) model that predicts the GFA of any binary or ternary system within its 52 element library (Ren et al., 2018). The ML model outputs the GFA of a given composition on a scale from 0 to 1 where a composition with a GFA near 1 has the best chance of vitrification if rapidly solidified via melt spinning. Ren et al. validated their ML model using high-throughput sputtering and XRD testing to prove that

compositions whose GFA was between 0.9-1.0 were in fact glass forming even in ternary systems with, until now, vast unexplored regions. Their model screened 2.38 million ternary compositions and predicted that only ~0.8% of these compositions are glass forming suggesting that without proper guidance only a small fraction of metallic glass design experiments would lead to the desired outcome.

Analysis of Alloy Design Modeling Tools

In this section the utility and accuracy of the available tools and models for predicting GFA and crack resistance are analyzed. Methods to predict GFA include a new T_i and T_g model created by QuesTek Innovations LLC, the ML model created by Ren et al. (Ren et al., 2018) and phase diagrams generated using Thermo-Calc Software. Mechanical property models to determine the shear modulus (G), hardness (H), bulk modulus (B), and Poisson's ratio (ν) of potential glass-forming alloy chemistries were created by QuesTek Europe AB.

Liquidus Temperature

The Thermo-Calc Software and databases TCFE9 and TCHEA3 are useful for predicting properties, including T_i , of crystalline Fe-based alloys and high-entropy alloys, respectively. As stated earlier, the T_i of a metallic glass is typically only available after successful fabrication. However, QuesTek Innovations LLC developed a metallic glass database, QT-BMG, to predict the T_i of Fe-based metallic glass. During cooling, crystallization becomes thermodynamically possible only when the temperature falls below the T_i , and vitrification becomes kinetically possible once the temperature of the uncrystallized melt drops below T_g . Naturally, glass formation is favored if the temperature difference between T_i and T_g is minimized. Since T_g is not strongly compositional dependent, alloy compositions that favor glass formation are due, among other effects, to a

depression in T_1 (typically deep eutectic compositions) (Greer, 1995). For this reason, accurately predicting the T_1 of potential glass-forming compositions is a useful indicator of GFA. In addition, T_1 can be combined with T_g values to calculate the temperature range for which solidification cracking can occur, ΔT . To determine the accuracy of the Thermo-Calc Software T_1 prediction, the experimental T_1 of 14 Fe-based BMGs found in literature were compared to those predicted by the TCFE9, TCHEA3 and QT-BMG databases. Fourteen BMGs were chosen for this comparison because each of the three databases contain selected elements, and it was challenging to find existing BMG chemistries whose constituents were found in all three databases. Figure 16 compares the experimental T_1 values determined via differential scanning calorimetry, and T_1 values calculated using all three databases. The TCHEA3, TCFE9 and QT-BMG databases on average over-predict the T_1 of the BMGs by

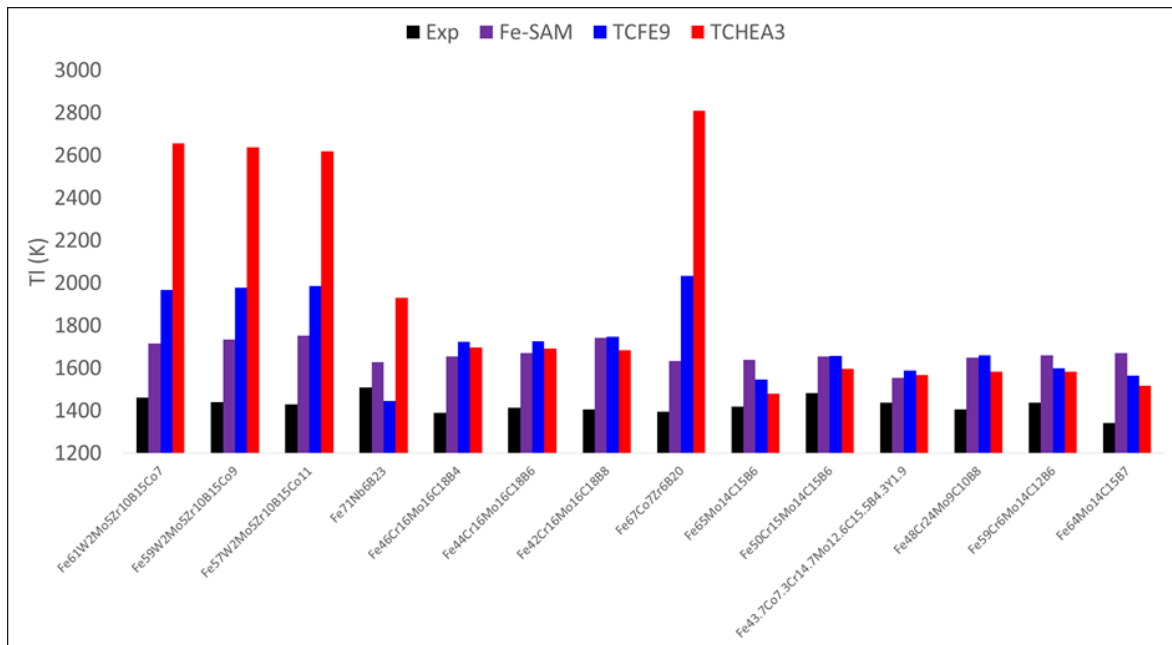


Figure 16. Experimental and calculated liquidus temperature (T_1). The liquidus temperature was calculated using Thermo-Calc databases TCFE9 and TCHEA3, and QuesTek's metallic glass database, QT-BMG.

507°C, 313°C and 242°C, respectively. None of the databases precisely predicts T_1 in a manner that would allow a fit parameter to improve the accuracy of the predicted T_1 . While the QuesTek database predicts the T_1 with greater accuracy than other databases, the predicted T_1 values still vary greatly from the experimental values and may not be useful during alloy design.

Glass Transition Temperature

In addition to the QT-BMG database for predicting the T_1 , QuesTek Innovations LLC produced a model to calculate the T_g of Fe-based metallic glass. The T_g model first predicts the shear modulus of prospective glass-forming chemistries for alloys in the Fe-M-B system (M is any combination of Ta, W, Mo, Hf, Zr, Nb, V, Cr, Mn, Ni and Co). To calculate shear modulus, the atomic fraction of molecular associates in the melt is calculated by considering the order of stability of each associate, then assuming complete saturation of that associate until one of the elemental constituents is fully consumed. The ‘next most stable’ associate then consumes the remaining elements. The order of stability of the associates is arbitrarily assumed, guided by the absolute melting temperature of the corresponding compound per atom. Then the shear modulus is calculated based on the weighted fraction of a fit value for each individual molecular associate (Equation 3). It is well documented that the mechanical properties of metallic glass are linked to the physical properties, such as the T_g (Chen et al., 1975; Yavari et al., 2007). Work from Bill Johnson demonstrated that a parabolic correlation exists between the shear modulus and T_g (Johnson and Samwer, 2005) (Equation 4). The calculated shear modulus was converted into T_g using Equation 4. The experimental T_g values from 89 different glass-forming alloys (all Fe-M-B) from the literature are compared to the calculated T_g in Figure 17. The points plotted in grey are from the FeB and FeNiB

families. These binary and ternary alloys are not bulk metallic glasses because they do not have an exceptionally high GFA. Since a majority of the data points are from high glass-forming alloys it is understandable why the model did not represent these alloys well. In addition, T_g is dependent on solidification rate, so it is reasonable to assume that a different T_g model is required for manufacturing processes with different cooling rates. Assuming that the presented model only predicts T_g for high glass-forming alloys, the binary and ternary alloys can be removed from Figure 17 (left). After this, the predicted T_g fits well with the measured T_g values (Figure 17 right) with $R^2 = 0.82$. The average difference between the experimental and measured T_g is only 11.9°C. This is exceptional, considering that T_g can vary by this amount simply by changing the solidification rate for a single composition (Equation 5). However, it is not surprising that the calculated values match the experimental values since the calculated values were fit to the experimental data. This means that the model might not predict T_g as well for new compositions that the model was not fit to. In addition, while there is a strong correlation between the shear modulus and experimental T_g of already manufactured BMGs, the same correlation will not hold in reverse i.e. the shear

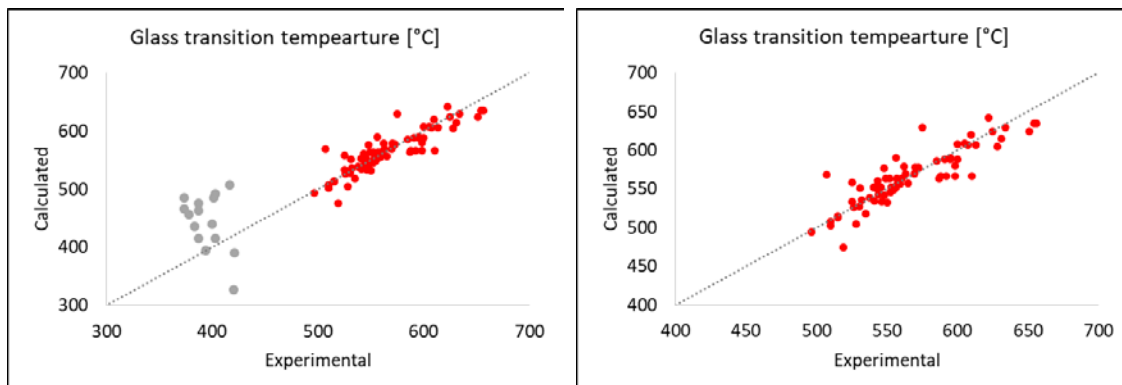


Figure 17. Experimental versus calculated glass transition temperature with (left) and without (right) low-glass-forming compositions.

modulus cannot predict the T_g . Predicting a T_g implies that an alloy is glass forming, however the model only uses the shear modulus, a mechanical property, to predict T_g and neglects all other known glass-forming effects. Even if this oversight is ignored, for this model to be useful the other glass formers for Fe-based BMGs, C and P, need to be added. This means that the number of molecular associates will at least triple. The ordering of the molecular associates is a determining factor in the predicted shear modulus and then T_g value, however, in the current model their order was arbitrarily assumed. If the number of molecular associates is tripled, the order will not be as trivial. A significant amount of work would be required to expand the T_g model to incorporate C and P, so it will not be used to guide BMG alloy design for this project.

Equation 3. Calculated shear modulus (G) where x_i and F_i are the atomic fraction and fit parameter of molecular associate i , respectively.

$$G = \sum (F_i \cdot x_i)$$

Equation 4. Calculated glass transition temperature (T_g) using the calculated shear modulus (G) (Johnson and Samwer, 2005).

$$T_g = (14098 \cdot G)^{0.49128} - 273$$

Equation 5. The width of the glass transition range for a typical glass former (Schmelzer and Tropin, 2013).

$$(T_g^+ - T_g^-) \cong \left(\frac{1}{10} - \frac{1}{20} \right) T_g$$

Machine Learning Model

Several theories have been proposed to describe the GFA of metallic alloys (Cahn and Greer, 1996; Inoue, 2000; Laws et al., 2015; Perim et al., 2016; Turnbull, 1969; Vincent et al., 2011; Yang and Zhang, 2012; K. Zhang et al., 2015), and while these theories may represent GFA well for certain alloy systems, there is no single model that can universally predict GFA. The ML model by Ren et al., which is open source, allows the inclusion of all GFA theories (Ren et al., 2018). In addition, the ML model was trained based on data collected from 6780 melt-spinning experiments at 5313 unique binary and ternary compositions found in the Landolt-Börnstein handbook (Kawazoe et al., 1997). The features in the ML model with the highest feature importance scores are the variance in covalent radii, the variance in electronegativity, the likelihood of glass formation from melt spinning data, and the mean number of unfilled valence orbitals (Ren et al., 2018). Even with the addition of several GFA theories, the experimental observations of metallic glass are still a top feature in the ML model. This suggests that, even as a whole, current GFA physiochemical theories are unable to truly capture the intricate chemistry behind metallic glass formation. Ren et al. identified a previously unobserved glass-forming region in the Co-V-Zr system using their ML model, and then validated these results using high-throughput sample production and evaluation; they found “remarkable agreements between ML prediction and experiments (Ren et al., 2018).” Due to the complexity of glass formation and the inability of current theories to universally predict GFA, the use of the open-source ML model by Ren et al. will be a useful tool during alloy design.

Phase Prediction

Brennhaugen et al. used the Thermo-Calc software to aid in the selection of glass-forming compositions in the Fe-Nb-B system (Brennhaugen et al., 2017). They calculated phase stabilities and the T_1 of potential alloy compositions in Thermo-Calc, and then combined these values with atomic size mismatch data to identify compositional spaces with potentially high GFA. Compositions in the identified regions were produced and glass-formation was confirmed by XRD analysis. Han et al. also used Thermo-Calc to aid in GFA prediction (Han et al., 2017). They present a design protocol to select the best glass-forming compositions that emphasizes nucleation in terms of compositional and structural fluctuations, predicting the difficulty of crystallization through consideration of the type and competition of potential phases. Work by Han et al. and Brennhaugen et al. demonstrate the utility of the Thermo-Calc TCFE crystalline metals databases to effectively map glass-forming compositional spaces by taking into account the driving force of potential crystalline phases.

Shear Modulus

QuesTek Europe AB produced a model containing all elements to predict the shear modulus of any prospective glass-forming chemistry using the weighted shear modulus of the elemental constituents with fit parameters (Equation 6). The experimental shear modulus values from 139 different glass-forming alloys (Fe-, Zr-, Ni-, Cu-, Pd-based, etc.) from the literature were compared to the shear modulus calculated using Equation 6 (Figure 18). There are two outliers in the plotted points, they are from $\text{Fe}_{80}\text{P}_{13}\text{C}_7$ and $\text{Nd}_{60}\text{Al}_{10}\text{Fe}_{20}\text{Co}_{10}$. Aside from those points, the calculated shear modulus values show excellent agreement with the experimental values. The ability to accurately predict the shear modulus of prospective

Equation 6. Calculated shear modulus (G) where x_i and G_i are the atomic fraction and shear modulus (scaled depending on crystalline structure) of element i , respectively.

$$G = \sum (G_i \cdot x_i)$$

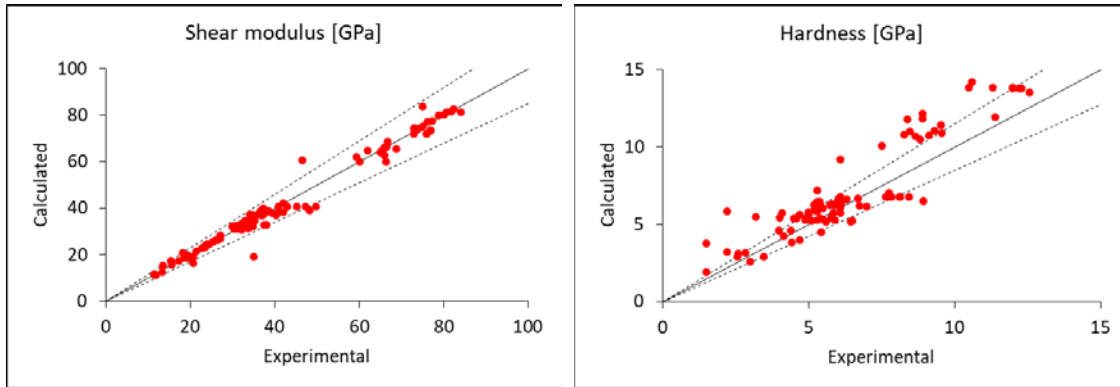


Figure 18. Experimental versus calculated shear modulus (left) and hardness (right) plotted with the + and – error lines.

alloy compositions is particularly valuable because it is a direct indication of the brittle/tough nature of the composition. Demetriou and Johnson state that tough Fe-based BMGs should have $G < 60$ GPa (Demetriou and Johnson, 2016), so the shear modulus model is a valuable tool to reject or accept potential chemistries based on desired toughness and crack resistance. The calculated shear modulus is also useful because it can be used to estimate the hardness and can be combined with the bulk modulus to predict the Poisson’s ratio.

Hardness

Chen et al. state that the hardness of BMGs is based on the same intrinsic characteristics as crystalline metals; therefore, the shear modulus of metallic glass should correlate with hardness as it does in crystalline metals (Chen et al., 2011). Their results suggest that if a material is intrinsically brittle (like a BMG that fails in the elastic regime),

its hardness linearly correlates with the shear modulus through Equation 7. Experimental versus calculated hardness values are reported in Figure 18. The calculated hardness values fit reasonably well with experimental values, but seem to trend towards over-predicting the hardness. Predicting hardness of potential BMG compositions is useful when designing alloys for high strength applications.

Equation 7. Vickers hardness of BMGs is estimated using the calculated shear modulus (Chen et al., 2011).

$$H_v = 0.151 \cdot G$$

Bulk Modulus

Similar to the shear modulus, the bulk modulus of prospective glass-forming chemistries are calculated using the weighted bulk modulus of the elemental constituents (a QuesTek Europe AB model) (Equation 8). Experimental bulk modulus values from 95 different glass-forming alloys (Fe-, Zr-, Ni-, Cu-, Pd-based, etc.) from the literature are compared to the calculated bulk modulus using Equation 8 (Figure 19). There are two outliers in the plotted points, they are from Fe₈₀P₁₃C₇ and Ni₆₀Nb₃₅Sn₅. Besides those, the calculated bulk modulus values show good agreement with the experimental values. Calculating the bulk modulus of glass-forming alloys is useful because it can be combined with the calculated shear modulus to predict the Poisson's ratio, as per Equation 9.

Equation 8. Calculated bulk modulus (B) where x_i and B_i are the atomic fraction and bulk modulus (scaled depending on crystalline structure) of element i , respectively.

$$B = \sum_i (B_i \cdot x_i)$$

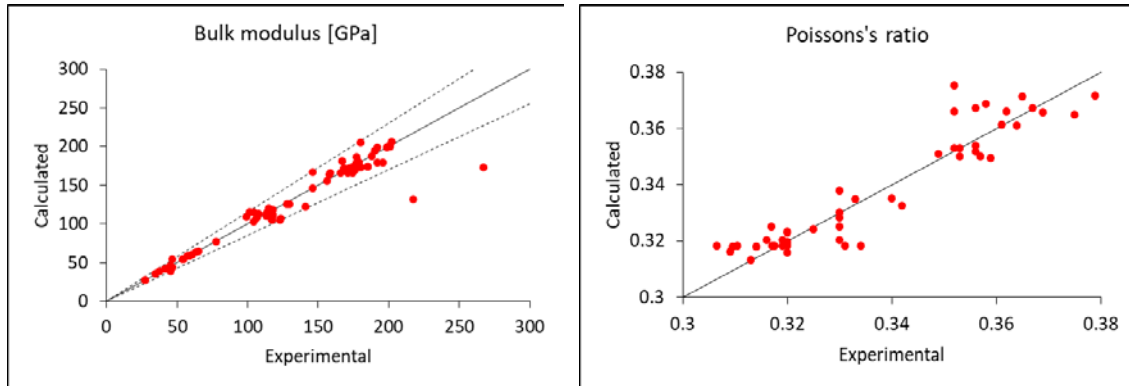


Figure 19. Experimental versus calculated bulk modulus plotted with the + and – error lines (left) and Poisson’s ratio (right).

Poisson’s Ratio

The Poisson’s ratio is a useful indicator of brittleness of metallic glass since it correlates with fracture energy. Typically, brittle metallic glass alloys exhibit $\nu < 0.31-0.32$ (Lewandowski et al., 2005). The experimental Poisson’s ratio values from 66 different glass-forming alloys from literature are compared to the calculated Poisson’s ratio in Figure 19 (calculated results from QuesTek Europe AB shear and bulk modulus models). The experimental and calculated values do not agree as strongly as the experimental and calculated bulk and shear modulus values; however, the Poisson’s ratio model is still useful since its primary use is to identify if a prospective alloy is tough, $\nu > 0.31-0.32$, and not to capture an exact Poisson’s ratio value.

Equation 9. Calculated Poisson’s ratio (ν) using calculated shear (G) and bulk (B) moduli.

$$\nu = \frac{3 - 2(G/B)}{6 + 2(G/B)}$$

Determining Mechanical Requirements

After analyzing the available models, it was important to quantify a mechanical property requirement for Fe-based metallic glass for AM. To start this process, all Fe-based glass-forming alloys that have been processed using an additive technique were listed (Table 4). Along with the chemistry, the experimental T_g and T_l , a qualitative description of the AM microstructure (cracking and amorphicity) and the calculated shear modulus are listed. Most of the literature reports or shows cracking in the AM material regardless of whether the material was amorphous or crystalline. Demetrieu and Johnson suggest that Fe-based BMGs with $G < 60$ GPa and $T_g < 440$ °C are tough (Demetriou and Johnson, 2016). Using this as a guideline, it can be asserted that no Fe-based BMGs in Table 4 are tough, and therefore all of the alloys cracked during additive processing. The two alloys highlighted in green in Table 4 do have shear moduli that satisfy $G < 60$ GPa, however they do not satisfy the T_g requirement. It was determined in the previous section that predicting T_g for potential glass-forming alloys is not practical; therefore, it can be approximated that a new glass-forming alloy for AM should have $G < 59$ GPa, since alloys with $G = 59$ GPa still cracked during AM.

Next, a list of Fe-based BMGs described as “tough” in the literature was compiled (Table 5). Unlike the alloys from Table 4, several alloys listed in Table 5 have $G < 60$ GPa and $T_g < 440$ °C, and are therefore considered tough by Demetrieu and Johnson’s criteria. These tough Fe-based BMGs typically contain more P than C or B, while alloys that were

AM typically contain C and B as the main glass-formers. Alloying elements C, B and P are glass-formers in Fe due to their small atomic radius, ability to depress the melting temperature and ability to hinder the formation of undesirable TCP phases. Electronic structure calculations by Gu et al. show that the electronic density of states in Fe₃M (M=C, B, P) binary alloys has an increasing metallicity from C through B to P (Gu et al., 2008). The increase in metallicity from C and B to P weakens the metal-metalloid bond, thereby lowering the shear modulus and elevating the Poisson's ratio of Fe-based compositions alloyed with P. Since the metallicity of the Fe-glass former bond is a main parameter in

Table 4. Fe-based glass-forming compositions that were processed using AM and their respective T_g, T_i, cracking and structure (Am=amorphous, Cr=crystalline, Am/Cr=amorphous matrix with grains). Some T_g and T_i values were collected from other references utilizing the same composition. Calculated shear modulus from the QuesTek Europe AB model are reported.

Composition (at. %)	T _g (°C)	T _i (°C)	Crack	Structure	G _{calc} (GPa)	Reference
FeCrMoWMnCSiB	-	-	-	Am/Cr	-	(Ye and Shin, 2014)
Fe ₇₁ Si ₁₀ B ₁₁ C ₆ Cr ₂	-	1250	-	Am/Cr	79.59	(Żrodowski et al., 2016)
Fe _{43.7} Co _{7.3} Cr _{14.7} Mo _{12.6} C _{15.5} B _{4.3} Y _{1.9}	838	1436	-	Am/Cr	79.53	(N. Li et al., 2018)
Fe ₅₈ Cr ₁₅ Mn ₂ B ₁ C ₄ Mo ₂ Si ₁ W ₁ Zr ₁	722	-	Yes	Am/Cr	59.16	(Zheng et al., 2009b)
Fe ₃₅ Cr ₂₅ Mo ₁₅ W ₁₀ C ₃ Mn ₅ Si ₂ B ₅	840	1463	-	Am/Cr	79.54	(Balla and Bandyopadhyay, 2010)
Fe ₇₄ Mo ₄ P ₁₀ C _{7.5} B _{2.5} Si ₂	750	-	Yes	Am/Cr	63.81	(Pauly et al., 2013)
Fe _{68.3} C _{6.9} Si _{2.5} B _{6.7} P _{8.7} Cr _{2.3} Mo _{2.5} Al _{2.1}	806	1216	Yes	Am	70.84	(Jung et al., 2015)
Fe _{43.7} Co _{7.3} Cr _{14.7} Mo _{12.6} C _{15.5} B _{4.3} Y _{1.9}	838	1436	Yes	Am	79.53	(Ouyang et al., 2018b)
Fe ₇₁ Si ₁₀ B ₁₁ C ₆ Cr ₂	-	-	Yes	Am/Cr	79.59	(Żrodowski et al., 2018)
Fe ₄₉ Cr ₁₈ B ₁₅ Mo _{7.4} Si _{2.4} C _{3.82} W _{1.6}	848	-	Yes	Am	88.06	(Nong et al., 2019)
Fe ₄₀₋₅₀ Mo ₂₄₋₃₂ Cr ₁₃₋₂₀	-	-	No	Am	-	(Wu et al., 2018)
Fe _{43.7} Co _{7.3} Cr _{14.7} Mo _{12.6} C _{15.5} B _{4.3} Y _{1.9}	-	-	Yes	Am	79.53	(Xing et al., 2018)
Fe ₄₈ Cr ₂₄ Mo ₉ C ₁₀ B ₈	887	1405	Yes	Am	85.78	Exmet AB
Fe ₅₉ Cr ₆ Mo ₁₄ C ₁₂ B ₆	806	1436	Yes	-	72.6	Exmet AB
Fe ₆₄ Mo ₁₄ C ₁₅ B ₇	793	1343	Yes	-	75.77	Exmet AB
Fe ₅₀ Ni ₃₀ P ₁₃ C ₇	-	-	Yes	Cr	59.28	Exmet AB
Fe ₇₃ Si ₁₁ B ₁₁ C ₃ Cr ₂	-	-	Yes	Am	76.56	Exmet AB

dictating mechanical properties, the addition of P will be favored over C and B during alloy design in an attempt to reduce the shear modulus and to improve crack resistance. It is important to consider that the mechanical and physical properties of metallic glass are interconnected. Typically, as the crack resistance increases, the GFA decreases, therefore, the alloy design developed in this chapter focuses on finding an appropriate balance of crack resistance and GFA for optimal AM processability.

Table 5. Fe-based glass-forming compositions that were described as “tough” and their respective T_g , T_i , plastic strain (compression), fracture strength and calculated shear modulus from the QuesTek Europe AB model.

Composition (at. %)	T_g (°C)	T_i (°C)	Pl st (%)	Fr Str (MPa)	G_{calc} (GPa)	Reference
Fe₇₅P₁₀C_{7.5}Mo₅B_{2.5}	435	985	5.5	3280	63.29	(Zhang et al., 2007)
Fe₇₂B₂₀Si₄Nb₄	556		1.9	4200	84.26	(Amiya et al., 2004)
Fe₇₆P₁₀C_{7.5}B_{2.5}Mo₂Si₂	456	991	5.7	3110	64.59	(Liu et al., 2009)
Fe₆₂Ni₁₈P₁₃C₇	-		50	-	59.78	(Guo et al., 2014)
Fe₈₀P₁₃C₇	396	998	1.1	3140	60.53	(Ma et al., 2013)
Fe₇₅P₁₃C₇Ni₅	394	990	5.2	3010	60.32	(Ma et al., 2013)
Fe₇₀P₁₃Ni₁₀C₇	388	986	6	2910	60.12	(Ma et al., 2013)
Fe₆₅Ni₁₅P₁₃C₇	384	980	9.8	2670	59.91	(Ma et al., 2013)
Fe₆₀Ni₂₀P₁₃C₇	380	974	11.2	2510	59.7	(Ma et al., 2013)
Fe₅₅Ni₂₅P₁₃C₇	376	966	7.7	2360	59.49	(Ma et al., 2013)
Fe₅₀Ni₃₀P₁₃C₇	367	955	8.2	213	59.28	(Ma et al., 2013)
Fe₇₁B₂₃Nb₆	-	-	1.6	4850	87.91	(Yao et al., 2008)
Fe₇₅P₁₀C_{8.3}Mo₅B_{1.7}	-	-	3.8	-	62.92	(Guo et al., 2010)
Fe₇₇P₉C_{7.5}Mo₅B_{1.5}	-	-	30.6	-	61.95	(Guo et al., 2010)
Fe₄₀Ni₄₀P₁₄B₆	-	-	5.21	-	60.43	(Guo et al., 2010)
Fe₇₅P₁₀C_{7.5}Mo₅B_{2.5}	-	-	5.5	-	63.29	(Guo et al., 2010)
Fe₅₀Ni₃₀P₁₃C₇	380	967	26-50+	-	59.28	(Sarac et al., 2018)
Fe₇₁P₁₂C₁₀Mo₅B₂	428	984	3.6	3150	64.81	(Gu et al., 2008)
Fe₆₉P₁₂C₁₀Mo₅B₂Cr₂	437	993	2.2	3200	65.83	(Gu et al., 2008)
Fe₆₉P₁₂C₁₀Mo₇B₂	443	990	2.8	3250	64.03	(Gu et al., 2008)
Fe₆₆P₁₂C₁₀Mo₁₀B₂	448	994	1.7	3250	62.86	(Gu et al., 2008)
Fe₆₄P₁₀C₁₀Mo₁₀B₃Cr₃	456	1015	1.2	3400	66.19	(Gu et al., 2008)
Fe₆₃P₁₂C₁₀Mo₁₀B₂Cr₃	462	1004	3.2	3400	64.39	(Gu et al., 2008)
Fe₆₃Mo₁₂P₁₀C₇B₅Cr₃	474	1026	0.9	3500	65.3	(Gu et al., 2008)
Fe₆₅P₁₀Mo₉C₈B₆Cr₂	483	1015	1	3550	68.48	(Gu et al., 2008)
Fe₇₁B₂₃Nb₆	-	-	1.6	4850	66.5	(Yao et al., 2008)

Step 2: Glass Forming Ability Plot Production

The second step was to produce GFA plots using the ML model by Ren et al. (Ren et al., 2018); the first generation of this model is available open source at <https://github.com/WardLT>. All iterations of Fe and the 37 other elements selected in step 1 were input into the ML model; this yielded 630 GFA plots with elemental composition varying from 0 - 100 at. % at a 1 at. % grid. The ML model output two plots for each ternary system. The first shows all experimental compositions within the ternary system that were input into the ML model and whether they had an amorphous, crystalline or a composite microstructure. The second shows a heat map of GFA within the ternary space on a scale from 0 to 1.0 where a composition with 1.0 has the highest chance of glass formation if produced via melt spinning. In the paper by Ren et al., the first generation ML model correctly predicted amorphicity for compositions with predicted GFA > 0.9, therefore, a color scaling was applied to the GFA heat maps such that areas with poor predicted GFA (GFA < 0.9 = shades of yellow) were easily discernable from compositional spaces with high predicted GFA (GFA > 0.9 = shades of green).

Step 3: Glass Forming Ability Plot Filtering

The third step was to separate and remove all ternary plots with poor GFA. First, the 630 diagrams were divided into two groups: *glass-forming* and *non-glass-forming*. Any ternary plots that only contained shades of yellow (GFA < 0.9) were added to the *non-glass-forming* group, and any plots containing shades of green were added to the *glass-forming* group. Of the 630 plots, 510 were separated into the *non-glass-forming* group; these were excluded from further consideration since the likelihood of glass formation is low. The 120 plots separated into the *glass-forming* group were sub-divided into three categories: *weak-*

glass-forming, *moderate-glass-forming*, and *strong-glass-forming*. Ternary GFA plots containing mostly shades of yellow with some light green regions were added to the *weak-glass-forming* group (32 plots). Diagrams containing mostly shades of light green were added to the *moderate-glass-forming* group (52 plots). The *weak* and *moderate-glass-forming* compositions were excluded from further consideration in an attempt to maximize the GFA of the ternary composition.

Thirty-six ternary compositions were separated into the *strong-glass-forming* group, they all contained a wide compositional space with $GFA = 1.0$. These areas of predicted high GFA were typically supported by experimental data points. Of the 36 *strong-glass-forming* compositions, 19 contained B as an alloying element. This is not surprising since B is a known glass-former in Fe and the FeB binary system has a wide glass-forming compositional space. Despite its positive effect on glass-formation, the addition of B is known to embrittle Fe-based metallic glass due to the strong, covalent Fe-B bond (Guo et al., 2014). For this reason, plots containing B were removed from further consideration. In fact, all plots containing a known glass-former in Fe (B, C and P) were removed since the intent of this step is to find a high glass-forming ternary system that did not yet contain a glass former. In doing this, there is an opportunity to improve the GFA of the $GFA = 1.0$ ternary compositions in future steps by adding a combination of B, C and P. This is a necessary step since the solidification rates of melt spinning are typically higher than those found in metal AM, so a material for AM requires a higher GFA than one for melt spinning.

After removing the ternary compositions containing B, C and P, 16 plots remained. Of these, 13 showed the $GFA = 1.0$ region in a compositional space containing < 50 at. % Fe. These compositions were removed since the intent of this alloy design is to create a Fe-based

alloy. After completing step 3, 3 ternary compositions remained: Fe-Ni-Ta, Fe-Zr-Co and Fe-Ni-Zr (Figure 21).

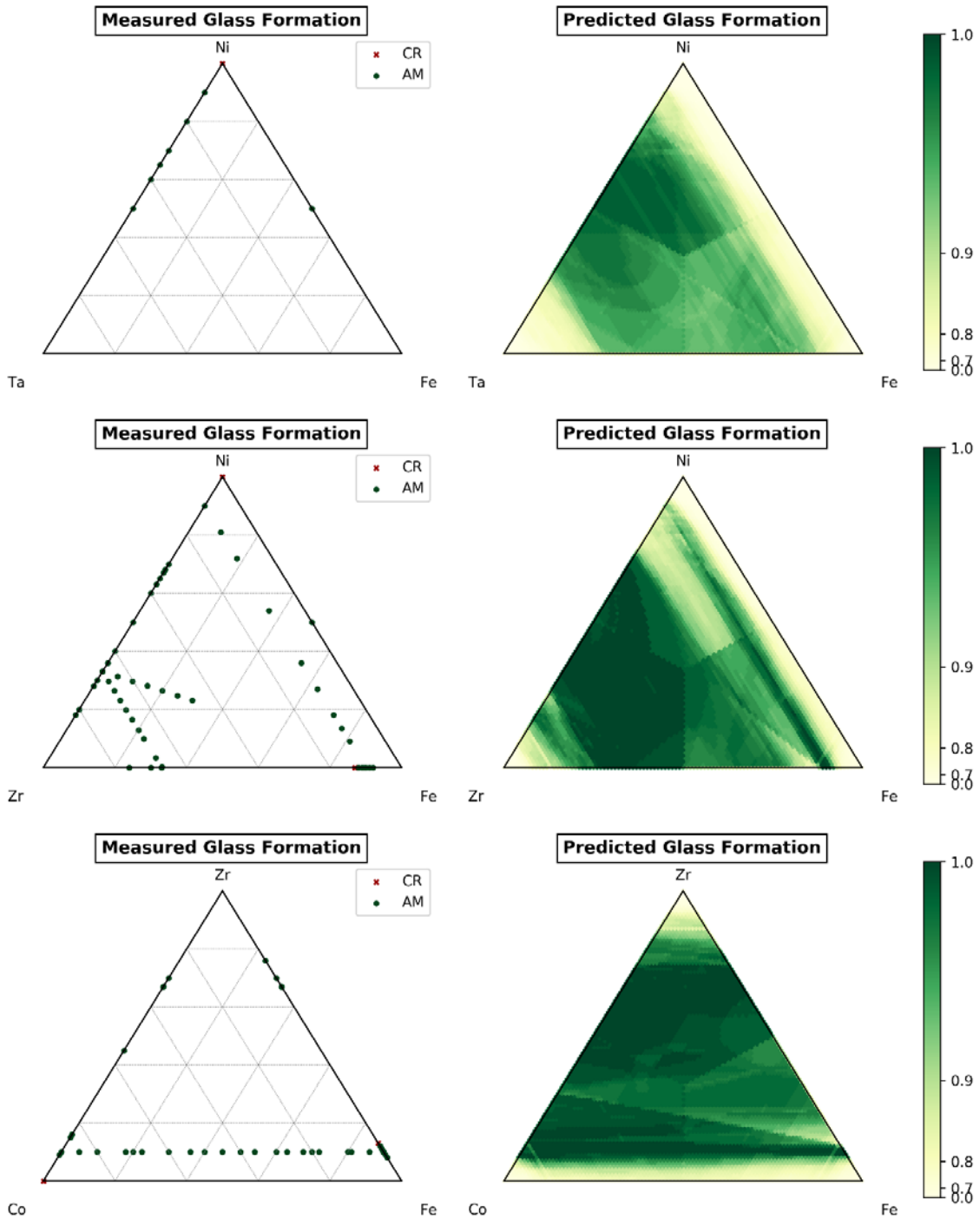


Figure 21. Selected ternary diagrams with high GFA (Ren et al., 2018).

Step 4: Shear Modulus Calculation

The fourth step in the alloy design process was to calculate the shear modulus of the high glass-forming Fe-Ni-Zr, Fe-Zr-Co and Fe-Zr-Ta ternary systems using the QuesTek Europe's shear modulus model. The current model cannot account for Ta additions, so shear modulus data from the Fe-Ni-Ta system is excluded. Ternary shear modulus diagrams of the Fe-Ni-Zr and Fe-Zr-Co systems are presented in Figure 22 with a 1 at. % grid. Both ternary compositional spaces have shear modulus values ranging from 27 GPa to 55 GPa; these represent the 100 at. % Zr and Fe corners, respectively. The effective shear moduli for selected elements are reported in Table 6. Since Ni and Co have very similar effective shear moduli, the Fe-Ni-Zr and Fe-Zr-Co ternary systems are nearly identical in terms of shear modulus. The purpose of calculating shear modulus is to ensure that a new alloy satisfies the crack resistance requirements for an AM material. According to the literature search in Table 4, Fe-based BMGs with $G \geq 59$ GPa cracked during AM. To find alloy chemistries with more crack resistance than those AM thus far, the alloy chemistry designed in this chapter must have $G < 59$ GPa. The entire compositional space of the Fe-Ni-Zr and Fe-Zr-Co systems satisfy this requirement.

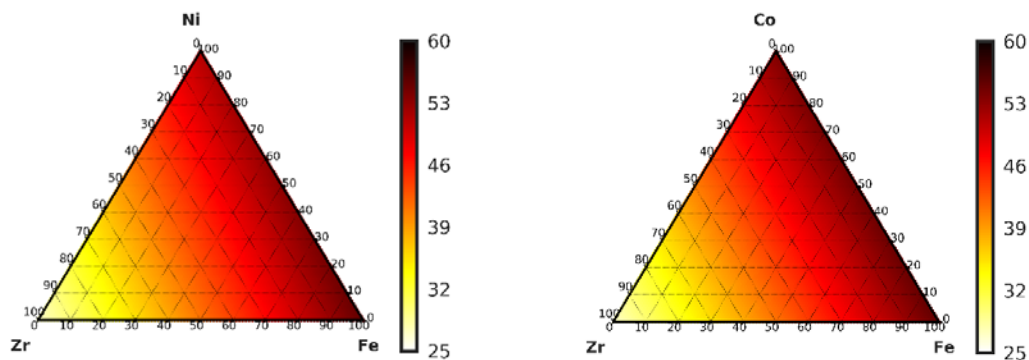


Figure 22. Shear modulus plots of the high glass-forming Fe-Ni-Zr and Fe-Co-Zr ternary systems.

Table 6. Effective shear modulus of selected elements from the QuesTek Europe AB shear modulus model.

Element	Effective Shear Modulus (GPa)
Fe	55.3
Ni	51.2
Co	53.9
Zr	27.1
P	39.8
C	78.7
B	204.4

Step 5: Phase Analysis

The fifth step was to analyze the ternary phase diagrams of Fe-Ni-Ta, Fe-Zr-Co and Fe-Ni-Zr. The purpose of phase analysis was to identify compositional spaces that contain TCP phases that easily nucleate from the supercooled melt and therefore negatively impact GFA. The phase diagrams were produced using the Thermo-Calc database TCFE9; they are shown in Figure 23. In the Fe-Ta-Zr system, the entire compositional space where Fe > 50 at. % contains the laves phase, a TCP phase. Therefore, without any addition of elements that suppress TCP phase formation (B and C) the Fe-Ta-Zr ternary compositions will not be the best starting point for alloy design. The laves phase was also found in the Fe-Ni-Zr and Fe-Co-Zr systems. Figure 24 outlines the compositional space on the Fe-Ni-Zr and Fe-Co-Zr GFA diagrams where Fe > 50 at. % and no TCP phases exist. Areas with GFA = 1 and no predicted TCP phases are an appropriate space to select a potential glass-forming composition. The Fe-Ni-Zr and Fe-Co-Zr systems differ by a single element, Ni and Co. Nickel and Co are adjacent on the periodic table and therefore have similar materials properties, evident by their nearly identical effective shear moduli. Since the Fe-Co-Zr phase

diagram contains a smaller compositional space that is free of TCP phases than the Fe-Ni-Zr phase diagram, only the Fe-Ni-Zr system will be used in the final steps of alloy development.

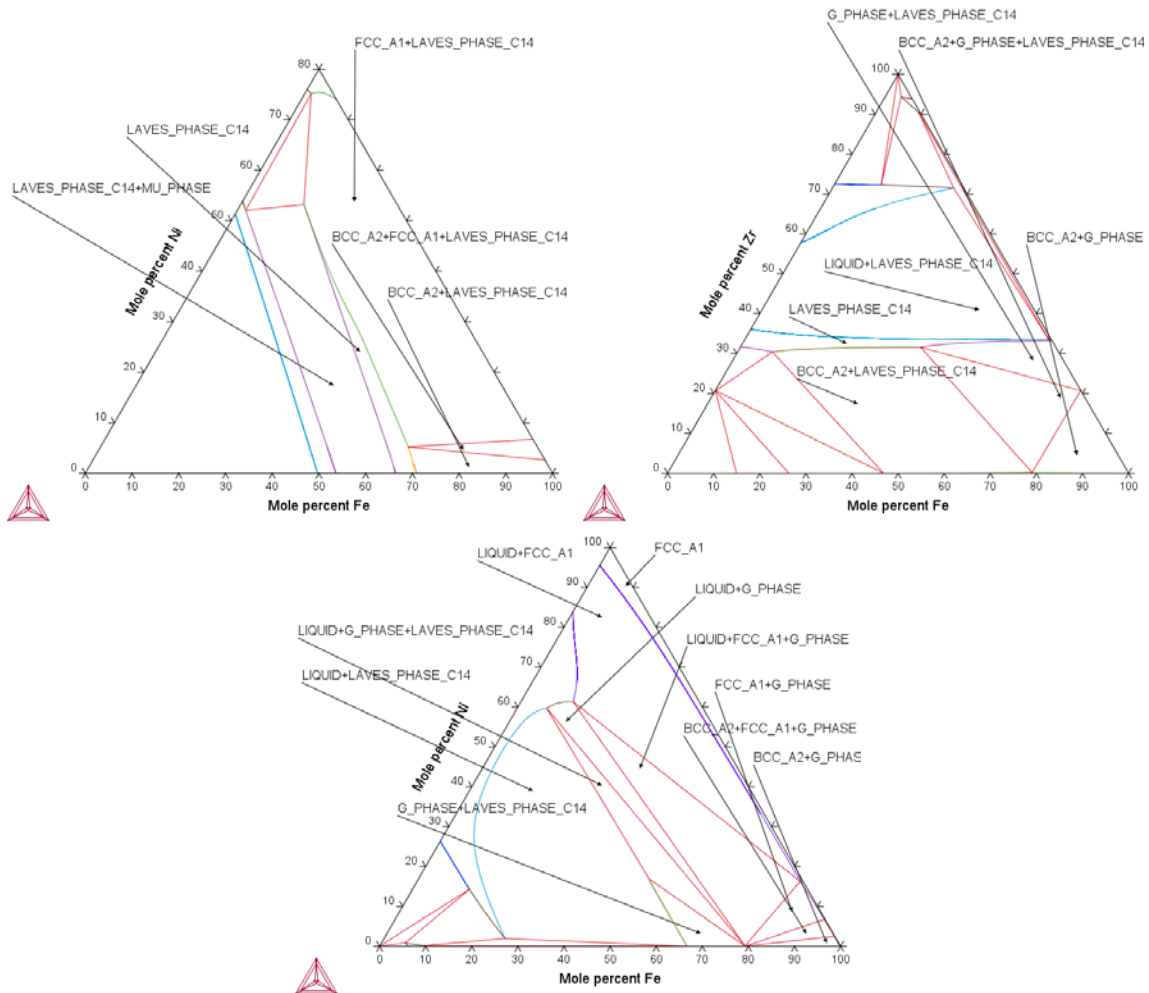


Figure 23. Ternary phase diagrams of Fe-Ni-Ta (top left), Fe-Zr-Co (top right) and Fe-Ni-Zr (bottom middle).

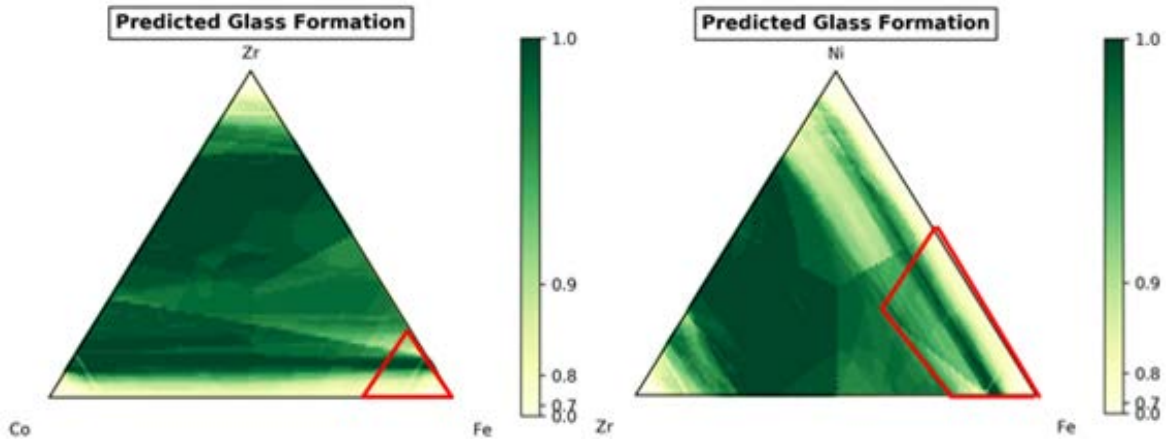


Figure 24. Ternary GFA diagrams of Fe-Zr-Co and Fe-Ni-Zr. Compositional space with Fe > 50 at. % and no TCP phases is outlined in red.

Step 6: Glass-former Addition

The sixth step was to improve the GFA of the compositional space outlined in step 5. The ML model created by Ren et al. and used in step 2 and 3 of the design process is based on data from melt spinning experiments. Therefore, the model predicts GFA for ternary compositions under the assumption that the alloy will be manufactured via melt spinning with solidification rates of 10^4 - 10^7 K/s. Different synthesis methods will noticeably alter GFA (Ren et al., 2018). Additive manufacturing has a unique thermal profile and thermal history. Since the solidification rates typical of LPBF (10^3 - 10^4 K/s) AM are lower than those typical of melt spinning, it is imperative that the GFA of the ternary composition selected from the ML model is improved. Improving the GFA increases the chances of obtaining an amorphous material after AM.

Additions of B, C or P to the high glass-forming ternary compositions facilitate GFA improvement. Of the three glass-formers, only B has enabled the production of binary metallic glass, Fe_xB_y . As a result, B is seemingly a better glass-former in Fe than C or P; this

is likely a result of the high bond strength of Fe-B compared to Fe-C and Fe-P rather than differences in atomic size or liquidus depression. Under the same assumption, C is a better glass former than P. Glass forming ability is inversely proportional to the ductility (i.e. crack resistance) of a metallic glass. This relationship is apparent when comparing the effective shear moduli of B, C and P where $B = 204.4$ GPa, $C = 78.7$ GPa and $P = 39.8$ GPa (from the QuesTek shear modulus model). Accordingly, additions of B will likely yield the greatest GFA improvement, but will lessen the shear modulus and crack resistance, and P will yield the least improvement on GFA, but will not lessen the crack resistance.

The objective of this design work is to create a Fe-based composition with high GFA and high crack resistance for AM. In chapter 3 the ability to fabricate a fully-amorphous Fe-based material via AM was demonstrated, however, micro-cracking was present in the AM material. For this reason, the primary focus of this alloy design is to achieve high crack resistance, so only additions of P are utilized to improve GFA to maintain a high crack resistance. Since the GFA is already high in the ternary system, the absence of the best glass-former, B, in the alloy should not hinder its ability to form a glass. The decision to forgo additions of B in this alloy design process resembles the compositions listed in the “tough” Fe-based metallic glass alloys in Table 5.

Determining the quantity of P to achieve the greatest GFA improvement is not clear. The compositions from Table 5 containing P and/or C averaged additions of 11.7 at. % and 8.0 at. %, respectively. The additions ranged from 9 - 14 at. % P and 7 - 10 at. % C. Using this as a starting point, the liquidus projections of Fe-Ni-Zr with addition of 5, 10 and 15 at. % P were mapped using the Thermo-Calc TCFE9 database (Figure 25) in an attempt to assess the impact of P quantity on GFA based on T_1 depression. The minimum T_1 values

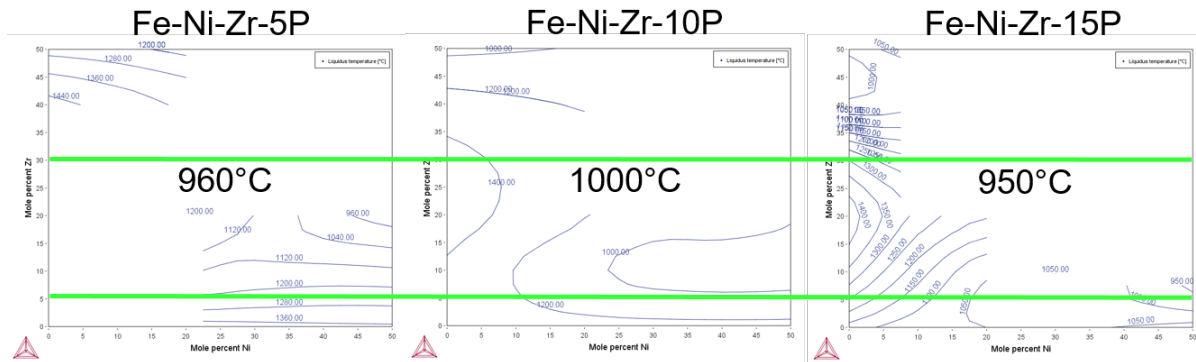


Figure 25. Liquidus projection of Fe-Ni-Zr-xP ($x = 5, 10$ and 15). The area between the green lines is the compositional space where TCP phases were not predicted on the Fe-Ni-Zr phase diagram. The temperature on each plot is the minimum liquidus within this region.

listed on each plot in Figure 25 do not show a distinct trend towards an optimal amount of P addition, and there is a $< 50^{\circ}\text{C}$ different between the T_1 predictions. The quantity of P may not heavily impact the T_1 of the ternary system. It is also plausible that the T_1 predictions from Thermo-Calc are not accurate for this alloy system. Either way, calculating the T_1 is not a useful metric to determine the ideal P addition to improve GFA in this alloy design methodology.

Instead of using T_1 as a measure of GFA, this process uses a stoichiometric balance between the metals (Fe, Ni and Zr) and the glass-former (P) in the alloy. The stoichiometric balance ensures that there is an adequate amount of glass-former to bond with the metals in the supercooled liquid region. The metal-GF (glass-former) bond is stronger than the metal-metal bond, and therefore a higher energy is required to break the metal-GF bond to allow for atomic rearrangement, a requisite for atomic diffusion and crystal growth. In addition, the stoichiometric balance helps avoid the metal-metal bond typical of phases with a very low activation energy, like laves. Two levels of stoichiometric balance were chosen: M_3GF and M_2GF ; these equate to $GF = 25$ at. % and $GF = 33$ at. % in the Fe-Ni-Zr-GF alloy.

Step 7: Composition Selection

Based on the methodology and data presented in steps 1 – 6, QuesTek Innovations LLC and QuesTek Europe AB selected the eight compositions listed in Table 7. These compositions do not have predicted TCP phases in their phase diagrams and are not too close to a TCP phase boundary or a non-glass-forming boundary, so minor compositional shifts that might occur during alloy production should not compromise the GFA of the alloy. Calculated values of the G , T_g , T_1 and v are reported in Table 7. The calculated G , T_g and v values suggest that all eight alloys are tough since $G < 60$ GPa, $T_g < 440^\circ\text{C}$ and $v > 0.32$. The T_1 values are lower than those of Fe-based alloys produced via AM (Table 4) and greater than those of the tough Fe-based alloys found in the literature (Table 5).

Table 7. Compositions selected by QuesTek Innovations LLC and QuesTek Europe AB for alloy design validation and their calculated G , T_g , T_1 and v values (2019 US Patent Application No. 62/851,261).

ID	Composition (at. %)	G (GPa)	T_g ($^\circ\text{C}$)	T_1 ($^\circ\text{C}$)	v
QTBMG11	Fe _{48.575} Ni _{8.375} Zr _{10.050} P _{33.000}	40	365	1202	0.37
QTBMG12	Fe _{58.725} Ni _{10.125} Zr _{12.150} P _{19.000}	46	406	1182	0.37
QTBMG13	Fe _{70.000} Ni _{4.000} Zr _{6.000} P _{20.000}	47	411	1148	0.38
QTBMG14	Fe _{55.125} Ni _{3.150} Zr _{4.725} P _{37.000}	40	358	1212	0.37
QTBMG15	Fe _{62.950} Ni _{19.500} Zr _{4.300} P _{13.250}	52	448	953	0.37
QTBMG16	Fe _{43.500} Ni _{13.500} Zr _{3.000} P _{40.000}	40	362	1189	0.37
QTBMG17	Fe _{49.000} Ni _{27.000} Zr _{13.000} P _{10.000}	51	444	1010	0.37
QTBMG18	Fe _{35.200} Ni _{19.200} Zr _{9.600} P _{36.000}	41	366	1191	0.37

Materials and methods for design analysis

Of compositions listed in Table 7, five were fabricated at Uppsala University in Uppsala, Sweden (QTBMG11, QTBMG12, QTBMG13, QTBMG15, and QTBMG17). Elemental material was purchased from Thermo Fisher Scientific and details of the material

purity and the product description are listed in Table 8. During sample preparation, binary master alloys of Ni-P and Fe-P were produced using induction melting since the melting and boiling point of P is significantly lower than that of Fe, Ni and Zr. These master alloy pellets were mixed such that their combined weight fraction was near the intended chemistry from the Table 7 list, and then placed into an arc furnace. The chemistry was further tuned towards the desired chemistry in the arc furnace by adding elemental Fe, Ni or Zr as needed. After compositional adjustment the melt was splat quenched with the intent of achieving solidification rates sufficient for amorphization.

The GFA of the proposed compositions was predicted using the Ren et al. ML model, which is based on data from melt spinning experiments. For this reason, the proposed compositions should ideally be produced using melt spinning since production method can significantly alter GFA. Due to challenges finding available melt spinning equipment, the alloys were instead fabricated using splat quenching, a technique similar to melt spinning. The solidification rates achievable during splat quenching, $\geq 10^4$ K/s, are similar to those achievable during melt spinning, 10^4 - 10^7 K/s. Therefore, the use of splat quenching to fabricate the proposed compositions should not significantly alter the results in terms of glass-formation or T_g .

After splat quenching, the material was analyzed at NCSU. The chemical compositions of the specimens were measured using a Niton™ XL3t GOLDD+ x-ray fluorescence spectrometer. Additionally, XRD spectra were collected using a Rigaku SmartLab x-ray diffractometer (0.05 step, 2 seconds per step). No further characterization was completed since the XRD results indicated that the splat quenched material was not amorphous.

Table 8. Product description of elemental material purchased from Thermo Fischer Scientific.

Element	Product description
Fe	Alfa Aesar™ Iron slug, 9.5mm (0.37 in.) dia. x 9.5mm (0.37 in.) length, 99.95+% (metals basis)
Ni	Alfa Aesar™ Nickel slug, 3.175mm (0.125 in.) dia. x 6.35mm (0.25 in.) length, 99.98% (metals basis)
Zr	Alfa Aesar™ Zirconium slug, 3.175mm (0.125 in.) dia. x 3.175mm (0.125 in.) length, 99.9+% (metals basis excluding Hf), Hf nominal 3%
P	Alfa Aesar 10g Phosphorus lump, red, Puratronic®, 99.999+% (metals basis)

Results

The five splat quenched specimens are depicted in Figure 26; many are in several pieces due to insufficient liquid dropped during splat quenching and the delicate nature of the thin material. Sample chemistries are reported in Table 9. The maximum difference between target and actual values of Fe, Ni, Zr and P was 6.0, 2.1, 3.6, and 5.9 wt. %, respectively. Trace amounts of Cu contamination were detectable on the QTBMG11 and QTBMG17 specimens; this contamination, seen and denoted by an arrow in Figure 27, originates from the Cu plate that the liquid material was dropped and pressed onto during splat quenching. X-ray diffraction spectra of the splat quenched samples are plotted in Figure 28. All spectra show indication of Bragg diffraction, as at least one peak is evident in each diffraction pattern. A high intensity peak near 45 degrees is apparent in four of the five specimens, and is slightly shifted along the 2θ axis. This “100% peak” and all lower intensity peaks are significantly broader than typical crystalline diffraction peaks. Lastly, the XRD patterns for QTBMG11 and QTBMG17 show a lot of background noise and had low counts in the raw data.



Figure 26. Splat quenched specimens.

Table 9. Target and actual chemistry of splat quenched specimens in weight percent.

ID		Fe	Ni	Zr	P	Cu
QTBMG12	Target	58.9	10.1	19.9	10.6	0.0
	Actual	58.7	11.0	16.3	13.3	0.0
	Diff	-0.1	0.9	-3.6	2.8	0.0
QTBMG17	Target	47.0	27.2	20.4	5.3	0.0
	Actual	45.1	25.2	17.1	10.4	1.4
	Diff	-1.9	-2.1	-3.3	5.1	1.4
QTBMG13	Target	78.6	4.4	10.3	11.7	0.0
	Actual	74.0	5.0	9.0	10.4	0.0
	Diff	-4.6	0.5	-1.3	-1.3	0.0
QTBMG15	Target	64.4	21.0	7.2	7.5	0.0
	Actual	63.4	22.2	6.2	7.8	0.0
	Diff	-0.9	1.3	-1.0	0.3	0.0
QTBMG11	Target	52.7	9.6	17.8	19.9	0.0
	Actual	58.7	9.9	16.7	13.9	0.2
	Diff	6.0	0.4	-1.1	-5.9	0.2



Figure 27. Copper contamination visible on the QTBMG17 specimen.

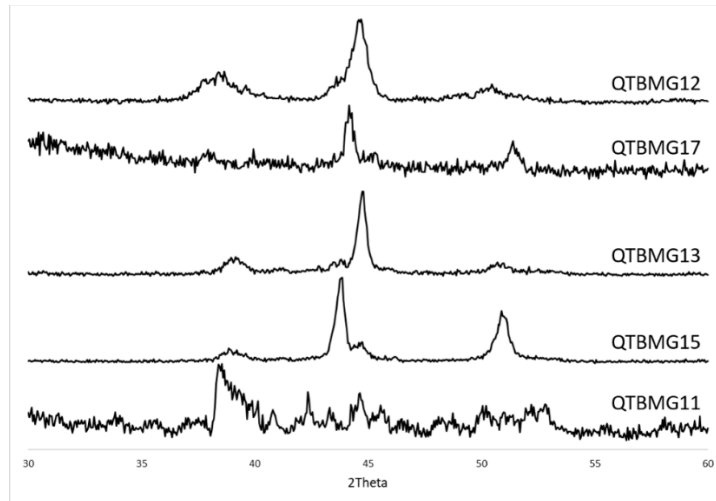


Figure 28. XRD spectra of splat quenched specimens.

Discussion

Despite the low boiling point of P, the P content fell below its target value in only two of the five splat quenched specimens, demonstrating the effectiveness of the master alloying methodology. Differences in the actual and target chemistries of all alloying elements ranged from 0.1 wt. % up to 6 wt. %. Unfortunately, this makes it challenging to validate the alloy design work within this chapter since glass-forming ability is sensitive to even a single atomic percent difference (Yanglin Li et al., 2017). Regardless, XRD analysis indicated that the compositional space of the proposed alloys was not glass-forming at the achieved solidification rates. Even the QTBMG15 specimen having ≤ 1.3 wt. % difference between the target and actual chemistry crystallized; this suggests that the GFA of the alloy or the solidification rates achieved during quenching was not as high as predicted.

In addition to crystalline peaks, the XRD spectra were characterized by peak broadening, peak shift, and background noise. Typically, peak broadening hints that a material is nano-crystalline or partially amorphous. If the specimens were partially

amorphous, complete broadening at all 2Θ values is expected along with some indication of an amorphous halo peak. Instead, the spectra in Figure 28 more resemble those of nanocrystalline materials. Furthermore, the peak shifting is likely the result of local concentration gradients or crystal lattice distortion (micro-strain). The latter is particularly probable in these experiments given the rapid, non-equilibrium solidification rates established during splat quenching. Two of the diffraction spectra, QTBMG11 and QTBMG17 also contained significant background noise and low counts collected per angle. It is likely that the x-ray beam did not have sufficient interaction with the material since the QTBMG11 sample did not contain a large amount of material, and only the edges of QTBMG17 were characterized in an attempt to avoid areas with Cu contamination. Despite the noise and low counts, both spectra contained at least one crystalline peak providing little incentive for re-collection of data.

The compositions proposed in this work were predicted to have sufficient GFA for splat quenching based off of a GFA ML model, analysis of equilibrium phases, and additions of the glass-former P. There are several probable causes of crystallization in the material. Firstly, it is possible that the absence of glass-formers B and C allowed TCP phases to nucleate easily during solidification even though the phases were not present on the equilibrium phase diagram. Although P is a known glass-former in Fe, it does not form a binary metallic glass with Fe like B and C. Additions of P actually decrease the calculated shear modulus of the FeNiZr alloy. Ignoring all other glass-formation theories, this suggests that P additions could be decreasing the GFA of FeNiZr. Furthermore, it is possible that the splat quench processing did not yield the required solidification rates and purity for glass-formation of the Fe-based alloys.

Chapter Summary

Previously manufactured Fe-based metallic glass alloys have exhibited poor AM processability evident by their propensity to crack regardless of process development efforts. Consequently, there is a need to identify the causes of crack formation during AM of metallic glass and ultimately select compositions with higher crack resistance than the ones previously selected while maintaining adequate GFA. This chapter provides a description of AM cracks and how they relate to metallic glass along with an analysis of the utility and accuracy of the available modeling tools for predicting GFA and crack resistance in potential glass-forming compositions. Tools for predicting GFA, potential phases, shear modulus, hardness, bulk modulus and Poisson's ratio demonstrated an ability to correctly predict values for existing glass-forming compositions. The GFA, potential phases and shear modulus models were applied in the novel alloy design sequence presented in this chapter. Utilizing the novel alloy design sequence, eight unique Fe-based compositions with predicted high GFA and crack resistance were identified. Five of the unique chemistries were fabricated via splat quenching. X-ray diffraction analysis showed that none of the splat quenched samples were amorphous. Possible causes of crystallization are the variation between the target and actual chemistries, lack of glass-formers B and C, or lower-than-expected solidification rates. Irrespective of the cause of crystallization, future work will target iterative design and experimental testing of novel chemistries intended to have high GFA and additive manufacturability. Collection of experimental data will expand our understanding of the design requirements for glass-formation and eventually AM, and will allow us to evolve and improve the modeling tools used in this work.

CHAPTER 6: SUMMARY

Iron-based metallic glass is an optimal material for use as magnetic shielding or transformer core materials, where their high strength and soft magnetic properties would offer a significant improvement in performance over the currently applied crystalline material. However, the requirement for rapid solidification during production limits the applicability of metallic glass since only simple, thin geometries are fabricable using the current manufacturing methods. Additive manufacturing allows for the production of near net shape components with complex and intricate geometries, unmatched by current metallic glass manufacturing techniques. In addition, additive deposition allows for the fabrication of components thicker than the critical casting thickness. Notable publications on the topic of AM of metallic glass were identified in this work, however, no report demonstrated the ability to AM a fully dense and amorphous metallic glass, nor have any samples exceeded the critical casting thickness. Chapters 3, 4 and 5 in this work provide novel research regarding the AM of metallic glass. The aim of the presented research is to allow for the fabrication of large-scale Fe-based metallic glass having a high potential for commercialization in terms of achievable dimension, geometry, materials properties, cost, and ease of fabrication.

The objective of chapter 3 was to demonstrate the ability to produce a Fe-based metallic glass component larger than its critical casting thickness. Significant process development work resulted in the fabrication of a fully amorphous FeCrMoCB component whose thickness is more than 15 times the critical casting thickness of the material, in all dimensions, and larger than any traditionally produced Fe-based BMG recorded. The AM-fabricated component contains no visible external cracks and is nearing full density. Even with a high relative density, sectioning revealed a dense distribution of microcracks within

the material likely resulting from residual stress accumulation and the inherent brittleness of the FeCrMoCB composition.

The aim of the fourth chapter was to reduce microcracking during AM of metallic glass by exploring the use of chemistry and process modifications. A variation of the FeCrMoCB alloy, FeMoCB, was elected for LPBF with the intent of improving the alloy's crack resistance without restarting LPBF process development. Modification of the alloy chemistry resulted in a visible improvement in crack resistance during LPBF, however microcracking was still significant. Dissimilarly, a higher plasticity Zr-based alloy (AMZ4) processed using the LPBF demonstrated a much higher crack resistance, and exhibited no microcracks after sectioning. An attempt to reduce microcracking during AM of the Fe-based alloys via process modification was ineffective. It was predicted that the elevated build temperature allowable during EBM would anneal the material in-situ, as it does in crystalline metals, reduce stress accumulation and reduce microcracking. Instead, the small heat capacity and isolated nature of the build plate resulted in overheating and crystallization.

The educated-guess, trial-and-error chemistry modification employed during chapter 4 did not yield a significant outcome for the Fe-based alloy, however results from AMZ4 processing give evidence that crack-free metallic glass is fabricable using LPBF if the material exhibits a high enough plasticity. For this reason, the objective of the final research chapter, chapter 5, was to design Fe-based glass-forming alloys for AM using a scientific methodology. Creating a scientific methodology to design glass-forming alloys suitable for AM required (1) understanding AM cracks and how they relate to metallic glass, (2) an analysis of the utility and accuracy of the available modeling tools for predicting GFA and crack resistance in potential glass-forming compositions, and (3) the determination of target

material properties for optimal AM processability based on alloys previously AM. Eight unique Fe-based compositions with predicted high GFA and crack resistance were named based on the alloy design methodology, and five were prototyped using splat quenching. Even though none of the splat quenched samples were amorphous, prototypes of this first iteration of alloy design provide useful insight into the requirements for designing for glass-formation. This work presents only a first step towards utilizing computational tools to design glass-forming compositions. After the modeling tools and property goals fully mature, the design approach presented in this work will accelerate the discovery of additively manufacturable metallic-glass compositions without the need for high-cost trial-and-error testing.

The motivation of this research was to allow for the fabrication of large-scale Fe-based metallic glass having a high potential for commercialization in terms of achievable dimension, geometry, materials properties, cost, and ease of fabrication. This work made notable strides towards this goal, and more scientific research is required before the ultimate insertion of these new materials. In future work, iterative design, prototyping, and characterization of novel chemistries will expand the understanding of quantifiable design requirements for glass-formation and AM, and will allow the modeling tools to evolve and improve. After a promising alloy is prototyped via splat quenching or melt spinning, the additive manufacturability and mechanical properties of the alloy will be characterized. Once AM of a Fe-based metallic glass yields fully-amorphous and crack free material, the material is ready for prototyping into functional parts intended for insertion into applications that would benefit from the unique properties of metallic glass.

REFERENCES

- Amiya, K., Urata, A., Nishiyama, N., Inoue, A., 2004. Fe-B-Si-Nb bulk metallic glasses with high strength above 4000 MPa and distinct plastic elongation. *Materials Transactions* 45, 1214–1218.
- Anantharaman, T.R., 1984. *Metallic glasses : production, properties and applications*, Materials science surveys ; no. 2. Trans Tech Publications, Aedermannsdorf, Switzerland.
- Ashby, M.F., Greer, A.L., 2006. Metallic glasses as structural materials. *Scripta Materialia*, Viewpoint set no: 37. On mechanical behavior of metallic glasses Viewpoint set no: 37. On mechanical behavior of metallic glasses 54, 321–326.
<https://doi.org/10.1016/j.scriptamat.2005.09.051>
- Balla, V.K., Bandyopadhyay, A., 2010. Laser processing of Fe-based bulk amorphous alloy. *Surface and Coatings Technology* 205, 2661–2667.
<https://doi.org/10.1016/j.surfcoat.2010.10.029>
- Belyakova, O.A., Slovokhotov, Y.L., 2003. Structures of large transition metal clusters. *Russian chemical bulletin* 52, 2299–2327.
- Bordeenithikasem, P., Shen, Y., Tsai, H.-L., Hofmann, D.C., 2018a. Enhanced mechanical properties of additively manufactured bulk metallic glasses produced through laser foil printing from continuous sheetmetal feedstock. *Additive Manufacturing* 19, 95–103. <https://doi.org/10.1016/j.addma.2017.11.010>
- Bordeenithikasem, P., Stolpe, M., Elsen, A., Hofmann, D.C., 2018b. Glass forming ability, flexural strength, and wear properties of additively manufactured Zr-based bulk

- metallic glasses produced through laser powder bed fusion. Additive Manufacturing. <https://doi.org/10.1016/j.addma.2018.03.023>
- Brennhaugen, D.D.E., Mao, H., Louzguine-Luzgin, D.V., Arnberg, L., Aune, R.E., 2017. Predictive modeling of glass forming ability in the Fe-Nb-B system using the CALPHAD approach. Journal of Alloys and Compounds, Selected papers presented at ISMANAM 2016, July 3rd-8th, Nara, Japan 707, 120–125. <https://doi.org/10.1016/j.jallcom.2016.12.049>
- Buckel, W., 1954. Elektronenbeugungs-Aufnahmen von dünnen Metallschichten bei tiefen Temperaturen. Z. Physik 138, 136–150. <https://doi.org/10.1007/BF01337905>
- Cahn, R.W., Greer, A.L., 1996. Metastable states of alloys. Physical Metallurgy (Fourth Edition) 1723–1830.
- Cesarano, J., Segalman, R., Calvert, P., 1998. Robocasting provides moldless fabrication from slurry deposition. Ceramic Industry; Troy 148, 94–102.
- Chen, C., Shen, Y., Tsai, H.-L., 2017. A Foil-Based Additive Manufacturing Technology for Metal Parts. J. Manuf. Sci. Eng 139, 024501. <https://doi.org/10.1115/1.4034139>
- Chen, H.S., 1980. Glassy metals. Rep. Prog. Phys. 43, 353. <https://doi.org/10.1088/0034-4885/43/4/001>
- Chen, H.S., 1974. Thermodynamic considerations on the formation and stability of metallic glasses. Acta Metallurgica 22, 1505–1511. [https://doi.org/10.1016/0001-6160\(74\)90112-6](https://doi.org/10.1016/0001-6160(74)90112-6)
- Chen, H.S., Krause, J.T., Coleman, E., 1975. Elastic constants, hardness and their implications to flow properties of metallic glasses. Journal of Non-Crystalline Solids 18, 157–171. [https://doi.org/10.1016/0022-3093\(75\)90018-6](https://doi.org/10.1016/0022-3093(75)90018-6)

- Chen, H.S., Turnbull, D., 1969. Formation, stability and structure of palladium-silicon based alloy glasses. *Acta Metallurgica* 17, 1021–1031. [https://doi.org/10.1016/0001-6160\(69\)90048-0](https://doi.org/10.1016/0001-6160(69)90048-0)
- Chen, H.S., Turnbull, D., 1968. Evidence of a Glass–Liquid Transition in a Gold–Germanium–Silicon Alloy. *The Journal of Chemical Physics* 48, 2560. <https://doi.org/10.1063/1.1669483>
- Chen, W., Liu, Z., Schroers, J., 2014. Joining of bulk metallic glasses in air. *Acta Materialia* 62, 49–57. <https://doi.org/10.1016/j.actamat.2013.08.053>
- Chen, X.-Q., Niu, H., Li, D., Li, Y., 2011. Modeling hardness of polycrystalline materials and bulk metallic glasses. *Intermetallics* 19, 1275–1281. <https://doi.org/10.1016/j.intermet.2011.03.026>
- Cullity, B.D. (Bernard D., Graham, C.D. (Chad D.), c2009. Introduction to magnetic materials [electronic resource]. IEEE/Wiley, Hoboken, N.J.
- DeCristofaro, N.J., Datta, A., Davis, L.A., Hasegawa, R., 1982. An iron-base metallic glass alloy with improved 60 Hz properties, in: *Proceedings of 4th International Conference on Rapidly Quenched Metals*. pp. 1031–1033.
- Demetriou, M.D., Johnson, W.L., 2016. Tough iron-based bulk metallic glass alloys. US9359664B2.
- Deng, L., Wang, S., Wang, P., Kühn, U., Pauly, S., 2018. Selective laser melting of a Ti-based bulk metallic glass. *Materials Letters* 212, 346–349. <https://doi.org/10.1016/j.matlet.2017.10.130>
- Drehman, A.J., Greer, A.L., Turnbull, D., 1998. Bulk formation of a metallic glass: Pd₄₀Ni₄₀P₂₀. *Applied Physics Letters* 41, 716. <https://doi.org/10.1063/1.93645>

- Drescher, P., Seitz, H., 2015. Processability of an amorphous metal alloy powder by electron beam melting. *RTEJournal - Fachforum für Rapid Technologie* 2015.
- Eckert, J., Das, J., Pauly, S., Duhamel, C., 2007. Mechanical properties of bulk metallic glasses and composites [WWW Document]. *Journal of Materials Research*.
<https://doi.org/10.1557/jmr.2007.0050>
- Fan, C., Inoue, A., 2000. Ductility of bulk nanocrystalline composites and metallic glasses at room temperature. *Applied Physics Letters* 77, 46–48.
- Fischer, P., Blatter, A., Romano, V., Weber, H.P., 2005. Selective laser sintering of amorphous metal powder. *Appl. Phys. A* 80, 489–492.
<https://doi.org/10.1007/s00339-004-3062-7>
- Gebert, A., Eckert, J., Schultz, L., 1998. Effect of oxygen on phase formation and thermal stability of slowly cooled Zr₆₅Al_{7.5}Cu_{17.5}Ni₁₀ metallic glass. *Acta Materialia* 46, 5475–5482. [https://doi.org/10.1016/S1359-6454\(98\)00187-6](https://doi.org/10.1016/S1359-6454(98)00187-6)
- Gibson, M.A., Mykulowycz, N.M., Shim, J., Fontana, R., Schmitt, P., Roberts, A., Ketkaew, J., Shao, L., Chen, W., Bordeenithikasem, P., Myerberg, J.S., Fulop, R., Verminski, M.D., Sachs, E.M., Chiang, Y.-M., Schuh, C.A., John Hart, A., Schroers, J., 2018. 3D printing metals like thermoplastics: Fused filament fabrication of metallic glasses. *Materials Today*. <https://doi.org/10.1016/j.mattod.2018.07.001>
- Greer, A.L., 2009. Metallic glasses...on the threshold. *Materials Today* 12, 14–22.
[https://doi.org/10.1016/S1369-7021\(09\)70037-9](https://doi.org/10.1016/S1369-7021(09)70037-9)
- Greer, A.L., 1995. Metallic glasses. *Science* 267, 1947.

- Gu, X.J., Poon, S.J., Shiflet, G.J., Widom, M., 2008. Ductility improvement of amorphous steels: Roles of shear modulus and electronic structure. *Acta Materialia* 56, 88–94.
<https://doi.org/10.1016/j.actamat.2007.09.011>
- Guo, S., Wang, M., Zhao, Z., Zhang, Y.Y., Lin, X., Huang, W.D., 2016. Molecular dynamics simulation on the micro-structural evolution in heat-affected zone during the preparation of bulk metallic glasses with selective laser melting. *Journal of Alloys and Compounds*. <https://doi.org/10.1016/j.jallcom.2016.11.393>
- Guo, S.F., Liu, L., Li, N., Li, Y., 2010. Fe-based bulk metallic glass matrix composite with large plasticity. *Scripta Materialia* 62, 329–332.
<https://doi.org/10.1016/j.scriptamat.2009.10.024>
- Guo, S.F., Qiu, J.L., Yu, P., Xie, S.H., Chen, W., 2014. Fe-based bulk metallic glasses: Brittle or ductile? *Appl. Phys. Lett.* 105, 161901. <https://doi.org/10.1063/1.4899124>
- Guo, Y.-L., Jia, L.-N., Kong, B., Huang, Y.-L., Zhang, H., 2017. Energy Density Dependence of Bonding Characteristics of Selective Laser-Melted Nb-Si-Based Alloy on Titanium Substrate. *Acta Metall. Sin.* <https://doi.org/10.1007/s40195-017-0670-8>
- Han, J.J., Wang, C.P., Wang, J., Liu, X.J., Wang, Y., Liu, Z.K., 2017. Compositional design of Fe-based multi-component bulk metallic glass based on CALPHAD method. *Materials & Design*. <https://doi.org/10.1016/j.matdes.2017.04.030>
- Hasegawa, R., 1983. *Glassy Metals: Magnetic, Chemical and Structural Properties*. CRC Press.
- Hofmann, D.C., Bordeenithikasem, P., Pate, A., Roberts, S.N., Vogli, E., 2018. Developing Processing Parameters and Characterizing Microstructure and Properties of an

- Additively Manufactured FeCrMoBC Metallic Glass Forming Alloy. *Advanced Engineering Materials* 0. <https://doi.org/10.1002/adem.201800433>
- Inoue, A., 2000. Stabilization of metallic supercooled liquid and bulk amorphous alloys. *Acta Materialia* 48, 279–306. [https://doi.org/10.1016/S1359-6454\(99\)00300-6](https://doi.org/10.1016/S1359-6454(99)00300-6)
- Inoue, A., Takeuchi, A., 2011. Recent development and application products of bulk glassy alloys. *Acta Materialia* 59, 2243–2267. <https://doi.org/10.1016/j.actamat.2010.11.027>
- Inoue, A., Zhang, T., Masumoto, T., 1989. Al–La–Ni Amorphous Alloys with a Wide Supercooled Liquid Region. *Mater. Trans., JIM* 30, 965–972. <https://doi.org/10.2320/matertrans1989.30.965>
- Inoue, A., Zhang, W., Zhang, T., Kurosaka, K., 2001. High-strength Cu-based bulk glassy alloys in Cu–Zr–Ti and Cu–Hf–Ti ternary systems. *Acta Materialia* 49, 2645–2652. [https://doi.org/10.1016/S1359-6454\(01\)00181-1](https://doi.org/10.1016/S1359-6454(01)00181-1)
- Jiao, Z.B., Luan, J.H., Guo, W., Poplawsky, J.D., Liu, C.T., 2016. Effects of welding and post-weld heat treatments on nanoscale precipitation and mechanical properties of an ultra-high strength steel hardened by NiAl and Cu nanoparticles. *Acta Materialia* 120, 216–227. <https://doi.org/10.1016/j.actamat.2016.08.066>
- Johnson, W.L., 2002. Bulk amorphous metal—An emerging engineering material. *JOM* 54, 40–43. <https://doi.org/10.1007/BF02822619>
- Johnson, W.L., Samwer, K., 2005. A Universal Criterion for Plastic Yielding of Metallic Glasses with a $(T/T_g)^{2/3}$ Temperature Dependence. *Physical Review Letters* 95, 195501. <https://doi.org/10.1103/PhysRevLett.95.195501>
- Jun, W.K., Willens, R.H., Duwez, P., 1960. Non-crystalline Structure in Solidified Gold–Silicon Alloys. *Nature* 187, 869. <https://doi.org/10.1038/187869b0>

- Jung, H.Y., Choi, S.J., Prashanth, K.G., Stoica, M., Scudino, S., Yi, S., Kühn, U., Kim, D.H., Kim, K.B., Eckert, J., 2015. Fabrication of Fe-based bulk metallic glass by selective laser melting: A parameter study. *Materials & Design* 86, 703–708.
<https://doi.org/10.1016/j.matdes.2015.07.145>
- Kawazoe, Y., Yu, J.Z., Tsai, A.P., Masumoto, T., 1997. Nonequilibrium Phase Diagrams of Ternary Amorphous Alloys, in Landolt-Bornstein, Numerical Data and Functional Relationships in Science and Technology.
- Kim, J.H., Lee, C., Lee, D.M., Sun, J.H., Shin, S.Y., Bae, J.C., 2007. Pulsed Nd:YAG laser welding of Cu₅₄Ni₆Zr₂₂Ti₁₈ bulk metallic glass. *Materials Science and Engineering: A, Proceedings of the 12th International Conference on Rapidly Quenched & Metastable Materials* 449–451, 872–875.
<https://doi.org/10.1016/j.msea.2006.02.323>
- Kim, S.-Y., Park, G.-H., Kim, H.-A., Lee, A.-Y., Oh, H.-R., Lee, C.-W., Lee, M.-H., 2017. Micro-deposition of Cu-based metallic glass wire by direct laser melting process. *Materials Letters* 202, 1–4. <https://doi.org/10.1016/j.matlet.2017.05.092>
- Kim, Y.J., Busch, R., Johnson, W.L., Rulison, A.J., Rhim, W.K., 1998. Metallic glass formation in highly undercooled Zr_{41.2}Ti_{13.8}Cu_{12.5}Ni_{10.0}Be_{22.5} during containerless electrostatic levitation processing. *Applied Physics Letters* 65, 2136.
<https://doi.org/10.1063/1.112768>
- King, W.E., Anderson, A.T., Ferencz, R.M., Hodge, N.E., Kamath, C., Khairallah, S.A., Rubenchik, A.M., 2015. Laser powder bed fusion additive manufacturing of metals; physics, computational, and materials challenges. *Applied Physics Reviews* 2, 041304. <https://doi.org/10.1063/1.4937809>

- Koptyug, A., Rännar, L.-E., Bäckström, M., Langlet, R., 2013. Bulk Metallic Glass Manufacturing Using Electron Beam Melting. Presented at the International Conference on Additive Manufacturing & 3D Printing, Nottingham, UK, July 2013.
- Kui, H.W., Greer, A.L., Turnbull, D., 1998. Formation of bulk metallic glass by fluxing. *Applied Physics Letters* 45, 615. <https://doi.org/10.1063/1.95330>
- Laws, K.J., Miracle, D.B., Ferry, M., 2015. A predictive structural model for bulk metallic glasses. *Nature Communications*; London 6, 8123. <http://dx.doi.org.prox.lib.ncsu.edu/10.1038/ncomms9123>
- Lewandowski *, J.J., Wang, W.H., Greer, A.L., 2005. Intrinsic plasticity or brittleness of metallic glasses. *Philosophical Magazine Letters* 85, 77–87. <https://doi.org/10.1080/09500830500080474>
- Li, B., Li, Z.Y., Xiong, J.G., Xing, L., Wang, D., Li, Y., 2006. Laser welding of Zr₄₅Cu₄₈Al₇ bulk glassy alloy. *Journal of Alloys and Compounds* 413, 118–121. <https://doi.org/10.1016/j.jallcom.2005.07.005>
- Li, H., Lu, Z., Yi, S., 2009. Estimation of the glass forming ability of the Fe-based bulk metallic glass Fe_{68.8}C_{7.0}Si_{3.5}B_{5.0}P_{9.6}Cr_{2.1}Mo_{2.0}Al_{2.0} that contains non-metallic inclusions. *Met. Mater. Int.* 15, 7. <https://doi.org/10.1007/s12540-009-0007-x>
- Li, H.X., Gao, J.E., Jiao, Z.B., Wu, Y., Lu, Z.P., 2009. Glass-forming ability enhanced by proper additions of oxygen in a Fe-based bulk metallic glass. *Appl. Phys. Lett.* 95, 161905. <https://doi.org/10.1063/1.3248186>
- Li, N., Zhang, J., Xing, W., Ouyang, D., Liu, L., 2018. 3D printing of Fe-based bulk metallic glass composites with combined high strength and fracture toughness. *Materials & Design* 143, 285–296. <https://doi.org/10.1016/j.matdes.2018.01.061>

- Li, X.P., Kang, C.W., Huang, H., Sercombe, T.B., 2014a. The role of a low-energy-density re-scan in fabricating crack-free Al₈₅Ni₅Y₆Co₂Fe₂ bulk metallic glass composites via selective laser melting. *Materials & Design* 63, 407–411. <https://doi.org/10.1016/j.matdes.2014.06.022>
- Li, X.P., Kang, C.W., Huang, H., Zhang, L.C., Sercombe, T.B., 2014b. Selective laser melting of an Al₈₆Ni₆Y_{4.5}Co₂La_{1.5} metallic glass: Processing, microstructure evolution and mechanical properties. *Materials Science and Engineering: A* 606, 370–379. <https://doi.org/10.1016/j.msea.2014.03.097>
- Li, X.P., Roberts, M., Liu, Y.J., Kang, C.W., Huang, H., Sercombe, T.B., 2015. Effect of substrate temperature on the interface bond between support and substrate during selective laser melting of Al–Ni–Y–Co–La metallic glass. *Materials & Design* (1980–2015) 65, 1–6. <https://doi.org/10.1016/j.matdes.2014.08.065>
- Li, X.P., Roberts, M.P., O’Keeffe, S., Sercombe, T.B., 2016. Selective laser melting of Zr-based bulk metallic glasses: Processing, microstructure and mechanical properties. *Materials & Design* 112, 217–226. <https://doi.org/10.1016/j.matdes.2016.09.071>
- Li, Y., Li, L., Li, B., 2015. Direct Ink Writing of Three-Dimensional (K, Na)NbO₃-Based Piezoelectric Ceramics. *Materials* 8, 1729–1737. <https://doi.org/10.3390/ma8041729>
- Li, Yingqi, Shen, Y., Chen, C., Leu, M.C., Tsai, H.-L., 2017a. Building metallic glass structures on crystalline metal substrates by laser-foil-printing additive manufacturing. *Journal of Materials Processing Technology* 248, 249–261. <https://doi.org/10.1016/j.jmatprotec.2017.05.032>
- Li, Y., Shen, Y., Hung, C.-H., Leu, M.C., Tsai, H.-L., 2018a. Additive Manufacturing of Zr-based Metallic Glass Structures on 304 Stainless Steel Substrates via V/Ti/Zr

- Intermediate Layers. *Materials Science and Engineering: A*.
<https://doi.org/10.1016/j.msea.2018.05.052>
- Li, Y., Shen, Y., Leu, M.C., Tsai, H.-L., 2018b. Mechanical properties of Zr-based bulk metallic glass parts fabricated by laser-foil-printing additive manufacturing. *Materials Science and Engineering: A*. <https://doi.org/10.1016/j.msea.2018.11.056>
- Li, Yingqi, Shen, Y., Leu, M.C., Tsai, H.-L., 2017b. Building Zr-based metallic glass part on Ti-6Al-4V substrate by laser-foil-printing additive manufacturing. *Acta Materialia*.
<https://doi.org/10.1016/j.actamat.2017.11.046>
- Li, Yanglin, Zhao, S., Liu, Y., Gong, P., Schroers, J., 2017. How Many Bulk Metallic Glasses Are There? *ACS Comb. Sci.* 19, 687–693.
<https://doi.org/10.1021/acscombsci.7b00048>
- Liebermann, H.H., c1993. Rapidly solidified alloys : processes, structures, properties, applications, *Materials engineering ; 3*. M. Dekker, New York.
- Lin, X., Zhang, Y., Yang, G., Gao, X., Hu, Q., Yu, J., Wei, L., Huang, W., 2019. Microstructure and compressive/tensile characteristic of large size Zr-based bulk metallic glass prepared by laser solid forming. *Journal of Materials Science & Technology, Recent Advances in Additive Manufacturing of Metals and Alloys* 35, 328–335. <https://doi.org/10.1016/j.jmst.2018.10.033>
- Lin, X.H., Johnson, W.L., Rhim, W.K., 1997. Effect of Oxygen Impurity on Crystallization of an Undercooled Bulk Glass Forming Zr–Ti–Cu–Ni–Al Alloy. *Mater. Trans., JIM* 38, 473–477. <https://doi.org/10.2320/matertrans1989.38.473>

- Liu, C.T., Chisholm, M.F., Miller, M.K., 2002. Oxygen impurity and microalloying effect in a Zr-based bulk metallic glass alloy. *Intermetallics* 10, 1105–1112.
[https://doi.org/10.1016/S0966-9795\(02\)00131-0](https://doi.org/10.1016/S0966-9795(02)00131-0)
- Liu, F., Pang, S., Li, R., Zhang, T., 2009. Ductile Fe–Mo–P–C–B–Si bulk metallic glasses with high saturation magnetization. *Journal of Alloys and Compounds* 483, 613–615.
- Liu, W.D., Ye, L.M., Liu, K.X., 2011. Micro-nano scale ripples on metallic glass induced by laser pulse. *Journal of Applied Physics* 109, 043109-043109–5.
<https://doi.org/10.1063/1.3552914>
- Liu, Z., Li, R., Liu, G., Song, K., Pauly, S., Zhang, T., Eckert, J., 2012. Pronounced ductility in CuZrAl ternary bulk metallic glass composites with optimized microstructure through melt adjustment. *AIP Advances* 2, 032176.
<https://doi.org/10.1063/1.4754853>
- Lu, X., Nursulton, M., Du, Y., Liao, W., 2019. Structural and Mechanical Characteristics of Cu₅₀Zr₄₃Al₇ Bulk Metallic Glass Fabricated by Selective Laser Melting. *Materials* 12, 775. <https://doi.org/10.3390/ma12050775>
- Lu, Y., Huang, Y., Wu, J., 2018. Laser additive manufacturing of structural-graded bulk metallic glass. *Journal of Alloys and Compounds*.
<https://doi.org/10.1016/j.jallcom.2018.06.259>
- Lu, Y., Zhang, H., Li, H., Xu, H., Huang, G., Qin, Z., Lu, X., 2017. Crystallization prediction on laser three-dimensional printing of Zr-based bulk metallic glass. *Journal of Non-Crystalline Solids* 461, 12–17. <https://doi.org/10.1016/j.jnoncrysol.2017.01.038>

- Lund, A.C., Schuh, C.A., 2004. The Mohr–Coulomb criterion from unit shear processes in metallic glass. *Intermetallics* 12, 1159–1165.
<https://doi.org/10.1016/j.intermet.2004.07.001>
- Ma, C., 2015. *Fundamental Study on Laser Interaction with Metal Matrix Nanocomposites*. UCLA.
- Ma, X., Yang, X., Li, Q., Guo, S., 2013. Quaternary magnetic FeNiPC bulk metallic glasses with large plasticity. *Journal of Alloys and Compounds* 577, 345–350.
<https://doi.org/10.1016/j.jallcom.2013.05.165>
- Mahbooba, Z., Thorsson, L., Unosson, M., Skoglund, P., West, H., Horn, T., Rock, C., Vogli, E., Harrysson, O., 2018. Additive manufacturing of an iron-based bulk metallic glass larger than the critical casting thickness. *Applied Materials Today*.
- Mao, J., Zhang, H.-F., Fu, H.-M., Wang, A.-M., Li, H., Hu, Z.-Q., 2009. The Effects of Casting Temperature on the Glass Formation of Zr-Based Metallic Glasses. *Adv. Eng. Mater.* 11, 986–991. <https://doi.org/10.1002/adem.200900174>
- Murty, B.S., Ping, D.H., Hono, K., Inoue, A., 2000. Influence of oxygen on the crystallization behavior of Zr₆₅Cu_{27.5}Al_{7.5} and Zr_{66.7}Cu_{33.3} metallic glasses. *Acta Materialia* 48, 3985–3996. [https://doi.org/10.1016/S1359-6454\(00\)00190-7](https://doi.org/10.1016/S1359-6454(00)00190-7)
- Nong, X.D., Zhou, X.L., Ren, Y.X., 2019. Fabrication and characterization of Fe-based metallic glasses by Selective Laser Melting. *Optics & Laser Technology* 109, 20–26.
<https://doi.org/10.1016/j.optlastec.2018.07.059>
- Ouyang, D., Li, N., Liu, L., 2018a. Structural heterogeneity in 3D printed Zr-based bulk metallic glass by selective laser melting. *Journal of Alloys and Compounds* 740, 603–609. <https://doi.org/10.1016/j.jallcom.2018.01.037>

- Ouyang, D., Li, N., Xing, W., Zhang, J., Liu, L., 2017. 3D printing of crack-free high strength Zr-based bulk metallic glass composite by selective laser melting. *Intermetallics* 90, 128–134. <https://doi.org/10.1016/j.intermet.2017.07.010>
- Ouyang, D., Xing, W., Li, N., Li, Y., Liu, L., 2018b. Structural evolutions in 3D-printed Fe-based metallic glass fabricated by selective laser melting. *Additive Manufacturing* 23, 246–252. <https://doi.org/10.1016/j.addma.2018.08.020>
- Pang, S., Zhang, T., Asami, K., Inoue, A., 2002. Effects of Chromium on the Glass Formation and Corrosion Behavior of Bulk Glassy Fe-Cr-Mo-C-B Alloys. *Mater. Trans.* 43, 2137–2142. <https://doi.org/10.2320/matertrans.43.2137>
- Pauly, S., Löber, L., Petters, R., Stoica, M., Scudino, S., Kühn, U., Eckert, J., 2013. Processing metallic glasses by selective laser melting. *Materials Today* 16, 37–41. <https://doi.org/10.1016/j.mattod.2013.01.018>
- Pauly, S., Schricker, C., Scudino, S., Deng, L., Kühn, U., 2017. Processing a glass-forming Zr-based alloy by selective laser melting. *Materials & Design* 135, 133–141. <https://doi.org/10.1016/j.matdes.2017.08.070>
- Perim, E., Lee, D., Liu, Y., Toher, C., Gong, P., Li, Y., Simmons, W.N., Levy, O., Vlassak, J.J., Schroers, J., Curtarolo, S., 2016. Spectral descriptors for bulk metallic glasses based on the thermodynamics of competing crystalline phases. *Nature Communications* 7, 12315. <https://doi.org/10.1038/ncomms12315>
- Prashanth, K.G., Shakur Shahabi, H., Attar, H., Srivastava, V.C., Ellendt, N., Uhlenwinkel, V., Eckert, J., Scudino, S., 2015. Production of high strength Al₈₅Nd₈Ni₅Co₂ alloy by selective laser melting. *Additive Manufacturing* 6, 1–5. <https://doi.org/10.1016/j.addma.2015.01.001>

- Ren, F., Ward, L., Williams, T., Laws, K.J., Wolverton, C., Hatrick-Simpers, J., Mehta, A., 2018. Accelerated discovery of metallic glasses through iteration of machine learning and high-throughput experiments. *Sci Adv* 4. <https://doi.org/10.1126/sciadv.aaq1566>
- Sarac, B., Ivanov, Y.P., Chuvilin, A., Schöberl, T., Stoica, M., Zhang, Z., Eckert, J., 2018. Origin of large plasticity and multiscale effects in iron-based metallic glasses. *Nature Communications* 9, 1333. <https://doi.org/10.1038/s41467-018-03744-5>
- Schmelzer, J.W.P., Tropin, T.V., 2013. Dependence of the width of the glass transition interval on cooling and heating rates. *The Journal of Chemical Physics* 138, 034507. <https://doi.org/10.1063/1.4775802>
- Schmid, G., 1988. Metal clusters and cluster metals. *Polyhedron* 7, 2321–2329.
- Schroers, J., 2010. Processing of Bulk Metallic Glass. *Adv. Mater.* 22, 1566–1597. <https://doi.org/10.1002/adma.200902776>
- Schroers, J., Masuhr, A., Johnson, W.L., Busch, R., 1999. Pronounced asymmetry in the crystallization behavior during constant heating and cooling of a bulk metallic glass-forming liquid. *Phys. Rev. B* 60, 11855–11858. <https://doi.org/10.1103/PhysRevB.60.11855>
- Schuh, C., Hufnagel, T., Ramamurty, U., 2007. Mechanical behavior of amorphous alloys. *Acta Materialia* 55, 4067–4109. <https://doi.org/10.1016/j.actamat.2007.01.052>
- Shen, Y., Li, Y., Chen, C., Tsai, H.-L., 2017a. 3D printing of large, complex metallic glass structures. *Materials & Design* 117, 213–222. <https://doi.org/10.1016/j.matdes.2016.12.087>

- Shen, Y., Li, Y., Tsai, H.-L., 2017b. Evolution of crystalline phase during laser processing of Zr-based metallic glass. *Journal of Non-Crystalline Solids*.
<https://doi.org/10.1016/j.jnoncrysol.2017.11.001>
- Simchi, A., 2006. Direct laser sintering of metal powders: Mechanism, kinetics and microstructural features. *Materials Science and Engineering: A* 428, 148–158.
<https://doi.org/10.1016/j.msea.2006.04.117>
- Sun, H., 2010. *Microstructure Evolution of Bulk Metallic Glasses via Laser Processing*. The Ohio State University.
- Sun, H., Flores, K.M., 2013. Spherulitic crystallization mechanism of a Zr-based bulk metallic glass during laser processing. *Intermetallics* 43, 53–59.
<https://doi.org/10.1016/j.intermet.2013.06.010>
- Sun, H., Flores, K.M., 2010. Microstructural Analysis of a Laser-Processed Zr-Based Bulk Metallic Glass. *Metall and Mat Trans A* 41, 1752–1757.
<https://doi.org/10.1007/s11661-009-0151-4>
- Sun, H., Flores, K.M., 2008. Laser deposition of a Cu-based metallic glass powder on a Zr-based glass substrate. *Journal of Materials Research* 23, 2692–2703.
<https://doi.org/10.1557/JMR.2008.0329>
- Telford, M., 2004. The case for bulk metallic glass. *Materials Today* 7, 36–43.
[https://doi.org/10.1016/S1369-7021\(04\)00124-5](https://doi.org/10.1016/S1369-7021(04)00124-5)
- Tregilgas, J.H., 2004. Amorphous titanium aluminide hinge. *Advanced Materials and Processes* 162, 40–41.

- Trexler, M.M., Thadhani, N.N., 2010. Mechanical properties of bulk metallic glasses. *Progress in Materials Science* 55, 759–839.
<https://doi.org/10.1016/j.pmatsci.2010.04.002>
- Tsai, P., Flores, K.M., 2016. High-throughput discovery and characterization of multicomponent bulk metallic glass alloys. *Acta Materialia* 120, 426–434.
<https://doi.org/10.1016/j.actamat.2016.08.068>
- Tsai, P., Flores, K.M., 2015. A Laser Deposition Strategy for the Efficient Identification of Glass-Forming Alloys. *Metall and Mat Trans A* 46, 3876–3882.
<https://doi.org/10.1007/s11661-015-2900-x>
- Tsai, P., Flores, K.M., 2014. A combinatorial strategy for metallic glass design via laser deposition. *Intermetallics* 55, 162–166. <https://doi.org/10.1016/j.intermet.2014.07.017>
- Turnbull, D., 1969. Under what conditions can a glass be formed? *Contemporary Physics*.
<https://doi.org/10.1080/00107516908204405>
- Vincent, S., Peshwe, D.R., Murty, B.S., Bhatt, J., 2011. Thermodynamic prediction of bulk metallic glass forming alloys in ternary Zr–Cu–X (X=Ag, Al, Ti, Ga) systems. *Journal of Non-Crystalline Solids* 357, 3495–3499.
<https://doi.org/10.1016/j.jnoncrysol.2011.06.024>
- Wang, H., Fu, H.M., Zhang, H.F., Hu, Z.Q., 2007. A Practical Thermodynamic Method to Calculate the Best Glass-forming Composition for Bulk Metallic Glasses. *International Journal of Nonlinear Sciences and Numerical Simulation* 8.
<https://doi.org/10.1515/IJNSNS.2007.8.2.171>
- Wang, H.S., Chen, H.G., Jang, J.S.C., Chiou, M.S., 2010. Combination of a Nd:YAG laser and a liquid cooling device to (Zr₅₃Cu₃₀Ni₉Al₈)Si_{0.5} bulk metallic glass welding.

- Materials Science and Engineering: A, Special Topic Section: Local and Near Surface Structure from Diffraction 528, 338–341. <https://doi.org/10.1016/j.msea.2010.09.014>
- Wang, Q., Qiang, J.B., Xia, J.H., Wu, J., Wang, Y.M., Dong, C., 2007. Cu–Zr–Al (Ti) bulk metallic glasses: Cluster selection rules and glass formation. *Intermetallics, Advanced Intermetallic Alloys and Bulk Metallic Glasses* 15, 711–715. <https://doi.org/10.1016/j.intermet.2006.10.025>
- Wang, T.L., Li, J.H., Liu, B.X., 2009. Proposed thermodynamic method to predict the glass formation of the ternary transition metal systems. *Phys. Chem. Chem. Phys.* 11, 2371–2373. <https://doi.org/10.1039/B818642A>
- Wang, W.H., Dong, C., Shek, C.H., 2004. Bulk metallic glasses. *Materials Science and Engineering: R: Reports* 44, 45–89. <https://doi.org/10.1016/j.mser.2004.03.001>
- Waniuk, T., Schroers, J., Johnson, W.L., 2003. Timescales of crystallization and viscous flow of the bulk glass-forming Zr-Ti-Ni-Cu-Be alloys. *Phys. Rev. B* 67, 184203. <https://doi.org/10.1103/PhysRevB.67.184203>
- Welk, B.A., Fraser, H.L., Dixit, V., Williams, T., Gibson, M.A., 2014. Phase Selection in a Laser Surface Melted Zr-Cu-Ni-Al-Nb Alloy. *Metall and Materi Trans B* 45, 547–554. <https://doi.org/10.1007/s11663-013-9907-8>
- Wu, W., Du, H., Sui, H., Sun, B., Wang, B., Yu, Z., Ni, H., Li, G., Zhao, J., 2018. Study of printing parameters of pneumatic-injection 3D printing of Fe-based metallic glass. *Journal of Non-Crystalline Solids* 489, 50–56. <https://doi.org/10.1016/j.jnoncrysol.2018.03.027>

- Xing, W., Ouyang, D., Li, N., Liu, L., 2018. Insight into micro-cracking in 3D-printed Fe-based BMGs by selective laser melting. *Intermetallics* 103, 101–106.
<https://doi.org/10.1016/j.intermet.2018.10.011>
- Xu, H., Lu, Y., Liu, Z., Wang, G., 2019. Laser 3D printing of Zr-based bulk metallic glass. *Journal of Manufacturing Processes* 39, 102–105.
<https://doi.org/10.1016/j.jmapro.2019.02.020>
- Yadroitsev, I., Gusarov, A., Yadroitsava, I., Smurov, I., 2010. Single track formation in selective laser melting of metal powders. *Journal of Materials Processing Technology* 210, 1624–1631. <https://doi.org/10.1016/j.jmatprotec.2010.05.010>
- Yaginuma, S., Nakajima, C., Kaneko, N., Yokoyama, Y., Nakayama, K.S., 2015. Log-normal diameter distribution of Pd-based metallic glass droplet and wire. *Scientific Reports (Nature Publisher Group); London* 5, 10711.
<http://dx.doi.org/10.1038/srep10711>
- Yang, C., Zhang, C., Xing, W., Liu, L., 2018. 3D printing of Zr-based bulk metallic glasses with complex geometries and enhanced catalytic properties. *Intermetallics* 94, 22–28.
<https://doi.org/10.1016/j.intermet.2017.12.018>
- Yang, G., Lin, X., Liu, F., Hu, Q., Ma, L., Li, J., Huang, W., 2012. Laser solid forming Zr-based bulk metallic glass. *Intermetallics* 22, 110–115.
<https://doi.org/10.1016/j.intermet.2011.10.008>
- Yang, X., Zhang, Y., 2012. Prediction of high-entropy stabilized solid-solution in multi-component alloys. *Materials Chemistry and Physics* 132, 233–238.
<https://doi.org/10.1016/j.matchemphys.2011.11.021>

- Yao, J.H., Wang, J.Q., Li, Y., 2008. Ductile Fe–Nb–B bulk metallic glass with ultrahigh strength. *Appl. Phys. Lett.* 92, 251906. <https://doi.org/10.1063/1.2949747>
- Yavari, A.R., Lewandowski, J.J., Eckert, J., 2007. Mechanical Properties of Bulk Metallic Glasses. *MRS Bulletin* 32, 635–638. <https://doi.org/10.1557/mrs2007.125>
- Ye, X., Shin, Y.C., 2014. Synthesis and characterization of Fe-based amorphous composite by laser direct deposition. *Surface and Coatings Technology* 239, 34–40. <https://doi.org/10.1016/j.surfcoat.2013.11.013>
- Zhang, C., Li, X., Liu, S.-Q., Liu, H., Yu, L.-J., Liu, L., 2019. 3D printing of Zr-based bulk metallic glasses and components for potential biomedical applications. *Journal of Alloys and Compounds* 790, 963–973. <https://doi.org/10.1016/j.jallcom.2019.03.275>
- Zhang, C., Wang, W., Li, Y.-C., Yang, Y.-G., Yue, W., Lin, L., 2018. 3D printing of Fe-based bulk metallic glasses and composites with large dimension and enhanced toughness by thermal spraying. *J. Mater. Chem. A*. <https://doi.org/10.1039/C8TA00405F>
- Zhang, K., Dice, B., Liu, Y., Schroers, J., Shattuck, M.D., O’Hern, C.S., 2015. On the origin of multi-component bulk metallic glasses: Atomic size mismatches and de-mixing. *The Journal of Chemical Physics* 143, 054501. <https://doi.org/10.1063/1.4927560>
- Zhang, T., Liu, F., Pang, S., Li, R., 2007. Ductile Fe-Based Bulk Metallic Glass with Good Soft-Magnetic Properties. *Mater. Trans.* 48, 1157–1160. <https://doi.org/10.2320/matertrans.48.1157>
- Zhang, Y., Lin, X., Wang, L., Wei, L., Liu, F., Huang, W., 2015. Microstructural analysis of Zr₅₅Cu₃₀Al₁₀Ni₅ bulk metallic glasses by laser surface remelting and laser solid forming. *Intermetallics* 66, 22–30. <https://doi.org/10.1016/j.intermet.2015.06.007>

- Zhang, Y., Lin, X., Wei, L., Liu, F., Huang, W., 2016. Influence of powder size on the crystallization behavior during laser solid forming Zr55Cu30Al10Ni5 bulk amorphous alloy. *Intermetallics* 76, 1–9.
<https://doi.org/10.1016/j.intermet.2016.06.006>
- Zhang, Y., Liu, H., Mo, J., Wang, M., Chen, Z., He, Y., Yang, W., Tang, C., 2018. Atomic-scale structural evolution in selective laser melting of Cu50Zr50 metallic glass. *Computational Materials Science* 150, 62–69.
<https://doi.org/10.1016/j.commatsci.2018.03.072>
- Zheng, B., Zhou, Y., Smugeresky, J.E., Lavernia, E.J., 2009a. Processing and Behavior of Fe-Based Metallic Glass Components via Laser-Engineered Net Shaping. *Metall and Mat Trans A* 40, 1235–1245. <https://doi.org/10.1007/s11661-009-9828-y>
- Zheng, B., Zhou, Y., Smugeresky, J.E., Lavernia, E.J., 2009b. Processing and Behavior of Fe-Based Metallic Glass Components via Laser-Engineered Net Shaping. *Metall and Mat Trans A* 40, 1235–1245. <https://doi.org/10.1007/s11661-009-9828-y>
- Zheng, B., Zhou, Y., Smugeresky, J.E., Schoenung, J.M., Lavernia, E.J., 2008. Thermal Behavior and Microstructural Evolution during Laser Deposition with Laser-Engineered Net Shaping: Part I. Numerical Calculations. *Metall and Mat Trans A* 39, 2228–2236. <https://doi.org/10.1007/s11661-008-9557-7>
- Zito, D., 2017. 3D direct metal printing: a trip through new opportunities and innovative alloys.
- Żrodowski, Ł., Wysocki, B., Wróblewski, R., Krawczyńska, A., Adamczyk-Cieślak, B., Zdunek, J., Błyskun, P., Ferenc, J., Leonowicz, M., Świąszkowski, W., 2019. New approach to amorphization of alloys with low glass forming ability via selective laser

melting. *Journal of Alloys and Compounds* 771, 769–776.

<https://doi.org/10.1016/j.jallcom.2018.08.075>

Żrodowski, Ł., Wysocki, B., Wróblewski, R., Krawczyńska, A., Adamczyk-Cieślak, B., Zdunek, J., Błyskun, P., Ferenc, J., Leonowicz, M., Świąszkowski, W., 2018. New approach to amorphization of alloys with low glass forming ability via selective laser melting. *Journal of Alloys and Compounds*.

<https://doi.org/10.1016/j.jallcom.2018.08.075>

Żrodowski, Ł., Wysocki, B., Wróblewski, R., Kurzydłowski, K.J., Świąszkowski, W., 2016.

The Novel Scanning Strategy For Fabrication Metallic Glasses By Selective Laser Melting, in: ResearchGate. Presented at the Fraunhofer Direct Digital Manufacturing Conference 2016.